UNIVERSITY OF DERBY

Numerical Study of Tractor-Trailer Gap Aerodynamics

Terrance Priestley Charles

Doctor of Philosophy   2020

Abstract

Aerodynamics have become an essential design process for ground vehicles in order to improve the fuel consumption by lowering the emissions along with increasing the range of vehicles using different source of power. A significant portion of the world CO_2 emissions is a result of ground vehicles with a more significant portion of these contributed by trucks. The boxy nature of trucks is the desired shape to carry maximum payload. However, a box shaped geometry is not aerodynamically efficient. Several manufacturers have developed aerodynamic add on devices that are optimized to the shape of the truck, in order to achieve gains in lowering emission and improving range by deeper understanding of the flow physics around the vehicle.

The thesis reports an in-depth understanding of the flow field within the gap region of a tractor trailer combination truck and how several aerodynamic add on devices reduce the overall drag of a truck. The gap region of a truck typically contributes to about 20-25% of the overall vehicle drag and hence presents an opportunity for considerable level of drag reduction.

A basic two box bluff body (2D & 3D) model was used to investigate how the flow field changes by changing the gap width between the two bluff bodies. A section of the thesis investigates the sudden increase in drag coefficient of the downstream cube around 2D tandem bluff bodies. Distinct flow patterns were observed in the gap and around the 2D tandem at different gap ratios. The sudden change in drag coefficient for the 2D downstream bluff body is well captured numerically, which is due to the wake of the upstream cube impinging onto the front face of the downstream cube. A steady increase in drag coefficient is witnessed for the 3D cubes which are consistent with previous experimental findings. The steady increase in drag coefficient is due to the vortical structures formed around the 3D cubes which are different, which consist of a smooth transition. Hence, they result in steady increase in drag coefficient.

A second study was conducted on a realistic truck like test case with the simplified truck model where the leading edges of the tractor were rounded off to manipulate the flow separation. As a result of leading edge rounding off the flow separation reduced significantly resulting in a major portion of the flow remain attached to the lateral walls of the tractor. This was seen to increase the flow entering the gap region between the tractor and trailer.

Finally, several add on devices which were subdivided based on tractor and trailer mounted devices were numerically assessed with several other devices within the gap region. Significant level of drag reduction was achieved for the entire truck with these add on devices. The highest drag reduction was achieved with the base bleeding technique.

Overall, the research has shown that it is important to control the flow condition within the gap region and maintain an even pressure on the front face of the trailer. The base bleeding method proved to be a vital technique to further reduce drag.

Acknowledgements

I owe my great thanks to my both my supervisors Prof Zhiyin Yang and Dr Yiling Lu for their support and guidance throughout the period of this study. This research and thesis would not have been completed without the encouragement and constant support from my supervisors. I also thank the University of Derby for providing all the necessary facilities in terms of computational and academic resources.

The technical staff and the support staff have been invaluable throughout my PhD journey especially the IT services who did an exceptional job in solving all my computational issues and helping me with running simulations at maximum efficiency.

Special thanks to my colleagues and fellow PhD students at MS109 Research student's office and elsewhere at the university. I extend my thanks to Adam Abikan who I worked closely with throughout the duration of our PhD. Thanks for Marzena Pawlik, Mijoh Gbededo, Solomon Mathew and Ade Muyiwa for the special friendship over the years within our office. To Scherin Pulprayil for all the laughs and memories. Don Dominic, Arun Dev and Suganjani S for being a big support when all things broke loose and helping me fix it.

Finally, my heartfelt thanks go to my parents who supported me in every possible way throughout the past 12 years of student status and providing me with the opportunity to pursue this. Without your patience, understanding, support and trust, I would not have made it this far in my life.

Table of Contents

List of Figure

List of Tables

Nomenclature

A	Area (m^2)
arg_1, arg_2	Arguments of blending functions F_1 & F_2
b	Height of trailer (m)
C_d	Drag coefficient
D	Cube length (L)
f_b	Resultant body forces such as gravity or centrifugal forces.
F_D	Drag force
F_1&F_2	Blending function for baseline $k - \omega$ and SST models.
H	Gap between cubes (m)
k	kinetic energy of turbulence ($m^2.s^{-2}$)
L	Length (m)
p_∞	Static Pressure in the freestream
P	Pressure Normal to the Surface (Pa)
S	Separation Point
T_t	Reynolds stress tensor
u	Velocity component (m/s)
μ_t	Eddy viscosity (m^2/s)
V	Vortices

Acronyms

2D	Two Dimensional
3D	Three Dimensional
CO_2	Carbon Dioxide
CVTD	Cross Vortex Trap Device
DES	Detached Eddy Simulation
EPA	European Protection Agency
GHG	Green House Gas
LES	Large Eddy Simulation
PDE	Partial Differential Equation

RANS   Reynolds Averaged Navier Stokes

SAE   Society of Automotive Engineering

URANS   Unsteady Reynold Averaged Navier Stokes

Greek variables

Δ Difference in terms

ρ Density (kg/m^2)

τ Shear Stress (Pa)

μ Dynamic Viscosity ($Pa.s$)

μ_t Eddy Viscosity

θ Angle (°)

Publication

List of authors academic publications

Terrance Charles, Yiling Lu and Zhiyin Yang. Impacts of The Gap Size Between Two Bluff bodies on The Flow Field Within the Gap. 13th International Conference on Heat Transfer, Fluid Mechanics and Thermodynamics, 2017. http://hdl.handle.net/2263/62393

Varun Raj TN, Vijaykrishna Jayaprakash and **Terrance Charles.** Experimental Investigation on the Performance and Emission Characteristics of a Direct Injection Diesel Engine Using Blends of Ethyl Ester of Jatropha Oil and Ethanol., and Terrance Charles. SAE NuGen Summit, 2019. https://doi.org/10.4271/2019-28-2378

Terrance Charles, Zhiyin Yang and Yiling Lu. Numerical Analysis of Flow in the Gap between a Simplified Tractor-Trailer Model and Cross Vortex Trap Device. International journal   of   Mechanical   and   Mechatronics   Engineering,   2019. doi.org/10.5281/zenodo.3593100

Terrance Charles, Zhiyin Yang and Yiling Lu. Assessment of Drag Reduction Devices Mounted on a Simplified Tractor-Trailer Truck Model. Journal of Applied and Computational Mechanics 2020. D.O.I: 10.22055/JACM.2020.34811.2475

Chapter 1

Introduction

1.1 Context and Motivation

In the present world, vehicle market has come under immense scrutiny to reduce the fuel consumption for conventional internal combustion engine vehicles. This has forced automobile manufacturers to shift focus on hybrid or fully electric vehicles. While these improvements are being achieved by developing the powertrain systems, they can also benefit from drag reduction of the vehicle, thereby reducing the power requirement of a vehicle to drive through the air. Aerodynamics force is the primary dominant on acting on a vehicle traveling at a speed above 60km/h (W.H.Hucho, 1997). With increasing cost of fossil fuels in the long term, stricter emission standards, vehicle designers have spent a lot of time, money and available resource in the last few decades focussing on reducing the aerodynamic drag of the vehicle.

In the late 20th century, aerodynamics was considered as a major part of ground vehicle design and development. In the 1970's the fuel crisis sped up the design and development of a more streamlined vehicle shape to be more widely accepted. Henceforth the drag coefficient progressively decreased until it became the talking point in the marketplace. Some successful examples included race cars. In the early 80's and 90's numerous researches were carried out on scaled truck models in order to develop aerodynamic upgrades which help reduce drag. However, there were several limitations for bringing them into production vehicle as they did not encompass common design parameters such as vehicle operating conditions, safety regulations and consumer perception. Some concepts, which had been trialled and tested, become more prevalent and are introduced to modern vehicle design. For example, boat tails are used on the rear end of the trailer. Depending on the manufacturer and consumer requirement, these boat tails differ in shapes and sizes to suit the payload and vehicle dimensions of the country.

Vehicle aerodynamics exhibits a complicated three-dimensional flow field which is a characteristic flow feature around bluff body. These flows contain several flow separations and are responsible for resultant pressure drag. The tractor and trailer have a gap where the air flow tends to separate and reattach. As a result, either negative or positive pressure effects on the back face of tractor and front face of trailer are reported, respectively. This complicated flow field can be influenced by several factors surrounding the vehicle. Most efforts have

focused on front/rear ends, and the under carriage of the vehicle. The pressure drag associated with the air gap region in the truck has a major contribution as high as 20% (Wood, 2006). It is very important to fully understand the flow field in the gap and reduce the resultant drag.
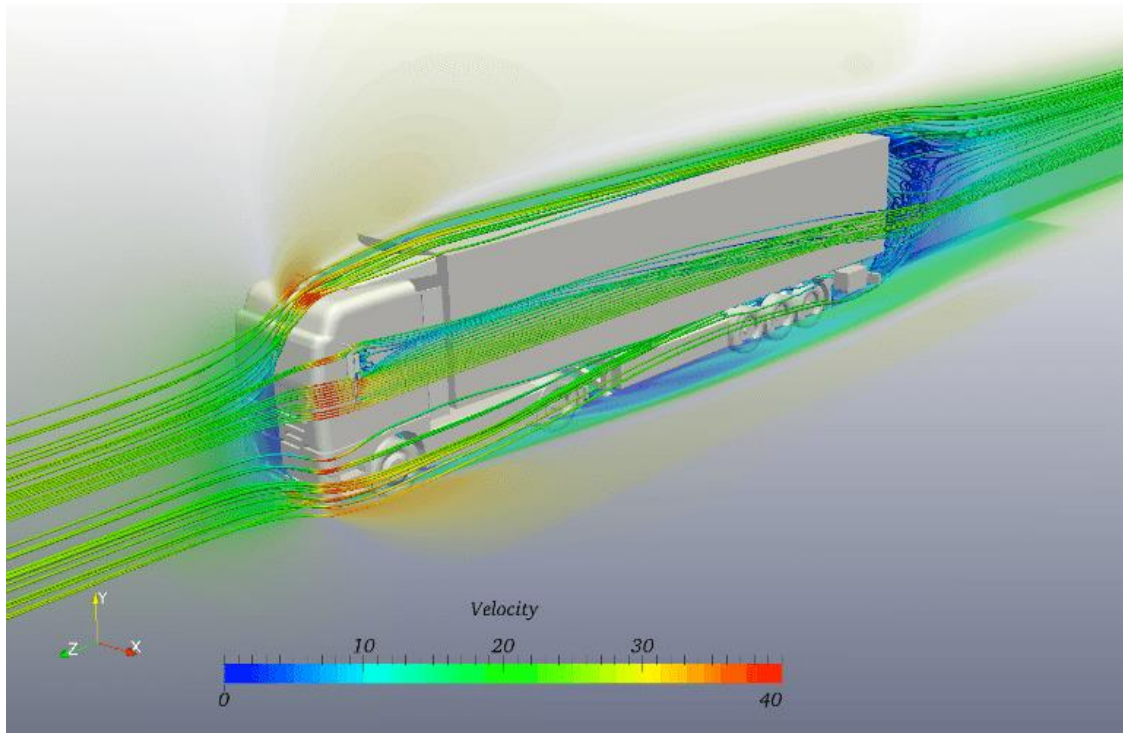
Figure 1.1: Flow field around a truck (Simscale, 2016).

1.2 Introduction

Transportability is the ability to move freely and easily. The evolution of transportability has expanded in terms of vision and culture, and satisfied every individual needs, dreams and desires. With the help of breakthrough in technology, transportation affects and improves our daily life. Motorbikes, cars, busses and trucks are directly or indirectly part of our daily routine. Hence it is important to continuously improve the standard of transportation by not settling for what is existing. A constant need to improve the technology involved in transportability is very important for a sustainable future. Several countries have taken some drastic decision and working towards a sustainable future. The goal of achieving zero emission is possible only by taking drastic action in the transport sector since transportation accounts to nearly a quarter of the total Green House Gas (GHG) production from vehicles. The 'European Strategy for Low Emission Mobility' has set clear goals to achieve - by mid-2000 the GHG emission has to be reduced by nearly 60% - and work towards zero emission path (European Strategy of Low emission, 2016). The transport industry is working towards a sustainable future to converge towards a common goal. Trucks need to improve their fuel efficiency to extend the mileage and maximise consumption efficiency. Improving the aerodynamics of heavy trucks will be a good contribution to help the transport industry achieve the target.

Flow around commercial vehicles including tractor trailers, buses and high-speed trains are inherently three-dimensional and exhibit complicated flow characteristics including turbulent boundary layer, separation and reattachment on the vehicle surface, trailing edges and large wake at the end of the vehicle. It is of considerable practical significance to understand the effects of these flow characteristics on the aerodynamic performance of the vehicle because they are closely related to affect fuel economy, Greenhouse gas emission along with driving stability etc. Several studies had been carried out in academics and industries to predict and understand flow control around heavy vehicles (Ahamed, et al., 1985) (Cooper, 2002) (Hucho, 1998) (Hucho & Sovran, 1993). Drag reduction of a vehicle has been of interests because it is directly related to the energy efficiency of a vehicle. A vehicle can achieve about 4% fuel saving if the aerodynamic drag of a truck is reduced by nearly 20% for a tractor weighing 36 tonnes and travelling at a highway speed of 105km/h (Bradley, 2000). With the increase in fossil fuel prices and the depletion of petroleum resources, this issue becomes very important to solve.

1.3 Fuel Economy

Figure 1.2 gives GHG emission by sectors. There exists an upward trend in the curve for transportation. This increase is mainly due to the consequence of increase in passenger and freight transportation demand which manifests in an increasing transport fleet and an increase in the number of kilometres travelled by these trucks (Delgado & Rodriguez, 2018).
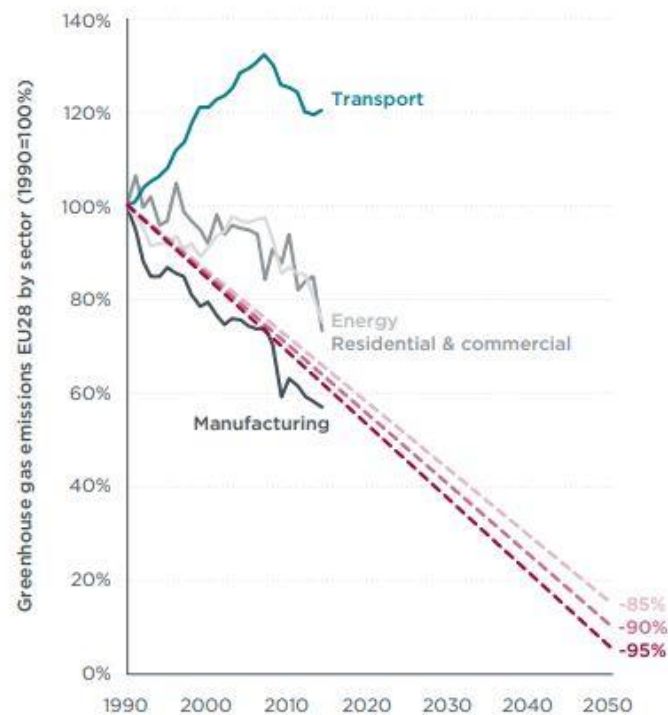
Figure 1.2: Energy Consumption by sectors (O. Delgado, 2018).

Fuel economy and increasing global warming are the key factors to have pushed automotive brands to design low drag models. Fuel consumption of a vehicle is a matter of supply and demand. Considering supply, it is the vehicle efficiency with which this energy is generated by the power train and delivered for application. On the demand side, the energy required to overcome mechanical losses of a vehicle are important. There exists an influence of aerodynamics which bridges this supply-demand relationship through drag forces of a vehicle. This drag force directly affects the propulsive part in the demand side of the vehicle (Hucho, 1998).

Trucks operate at a relatively constant highway speed. An in-depth analysis of factors affecting vehicle fuel economy can be split into two categories depending on type of roads the vehicle is being driven, Urban and Highway. These two types roads represent the two major types of driving conditions. In most countries speed variations can be found on these two types of roads. In Europe the regulations determining these speeds are based on the Euromix cycle which is a combination of the simple urban driving schedule and two constant speed cruising conditions on the highway (Hucho, 1998).

In the United States, transportation activities account to nearly 28% of the total US energy use and 33.4% of the carbon dioxide production. The transportation sector has come under intense scrutiny since it is the largest emitter of GHG emission. Investigation and technical solutions have been scarce for heavy duty diesel trucks, with their contribution towards GHG emission accounting to about 22.8% of the total CO_2 production in the transport sector (EPA, 2015). It is estimated that emission from trucks are bound to increase by almost 10% only in Europe by 2030 (Delgado & Rodriguez, 2018). The fuel efficiency of an average European tractor-trailer has remained stagnant for the past 10 years. Figure 1.3 gives an insight to data on fuel consumption for tractor trailers from the past fourteen years. The stagnation is due to strict laws enforced on these truck manufacturers which have ultimately offset any engine and vehicle efficiency improvements.
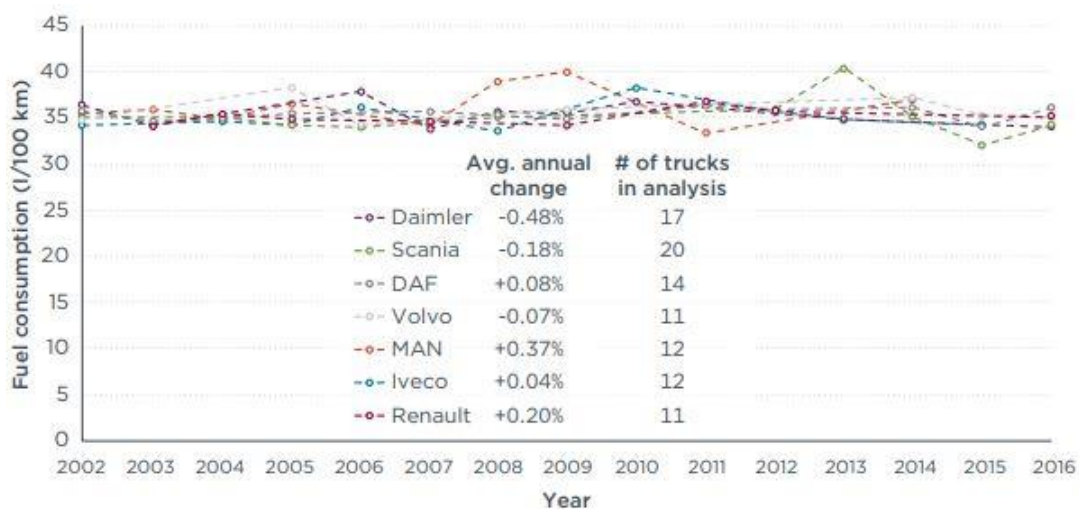
Figure 1.3: Fuel consumption of tractor-trailers with engine power between 300 to 400kw (Delgado & Rodriguez, 2018).

Being fuel consumption and emission as a major concern to truck manufacturers, a detailed insight into how emission has affected the atmosphere and what direct impact it has on Global warming is given in the next section.

1.4 Transportation and Global Warming

Automotive transportation has been going through an overhaul to battle climate change. The most evident overhaul is the shift from internal combustion engines which use fossil fuels to hybrid power technology and finally electrification of vehicles. The other significant change is the automation of vehicles along with improvement in safety, comfort and convenience. As a result of this recent revolution the future of driving around in urban and motorways will look very different from the experience we have today. Cities are very likely to be filled with zero emission vehicles which communicate among themselves in order to assist self-driven cars (Steinmetz, 2017).

In the year 2007, Germany came up with a solution to solve Global warming to reduce the greenhouse gas emissions by 40% by the year 2020. The statement was an aggressive climatic goal for scientists from some of the developed countries. However, till date Germany has managed to reduce greenhouse gasses by 27.7% which seemed like an astonishing achievement for a developed country which houses some of the major automotive brands (Atkin, 2010).

In the 21st century there exist a huge dependence of petroleum fuels in the transportation sector. In certain countries the transportation sector is responsible for one third of the countries climate change. In the United States nearly 30% of all global warming emissions are produced from trucks, ships, planes and cars, resulting in the transport industry being the highest contributor to global warming. Transport is single headedly the largest consumer of fossil fuels. In recent years there has been an immense scarcity of fossil fuels due to their ever-increasing usage. A typical heavy-duty cargo truck requires energy from the air and fuel. Burning of fossil fuels causes air pollution by producing nitrous oxides and other particulates. They are significant contributors to global warming. The transport sector including air ways, water ways and road transport is the major contributor to greenhouse gasses which becomes the primary cause of global warming.

Several countries have introduced strict emission norms which have pushed automotive manufacturers to improve their emission standards in the past few years. However, there has

been an increase in vehicle usage which ultimately overrides the reduction in greenhouses gasses which are controlled by emission regulations.

Figure 1.4 shows the distribution of greenhouse gas emission from various sectors in the US. From Figure 1.4, transportation generates the highest share of greenhouse gas emission when compared to other sectors. GHG from the transportation industry mainly comes from the burning of fossil fuels. Over 90% of the fuel used in the transportation industry comes from fossil fuels. When considering the electricity sector, the vast majority of GHG comes from burning fossil-based fuels such as coal, oil and natural gas to produce electricity. Burning coal is highly carbon intensive than burning natural gas or petroleum for producing electricity. Even though coal accounts to only about 67.9% of the total CO_2 emission from the electricity sector, it represents nearly 31.2% of the electricity generated in the United States in 2019. The industrial sector which produces GHG emissions can be categorised into direct emissions and indirect emissions. Direct emissions are the produces onsite and indirect emissions occur offsite. Direct emission occurs by burning fuel for generating power and heat onsite.
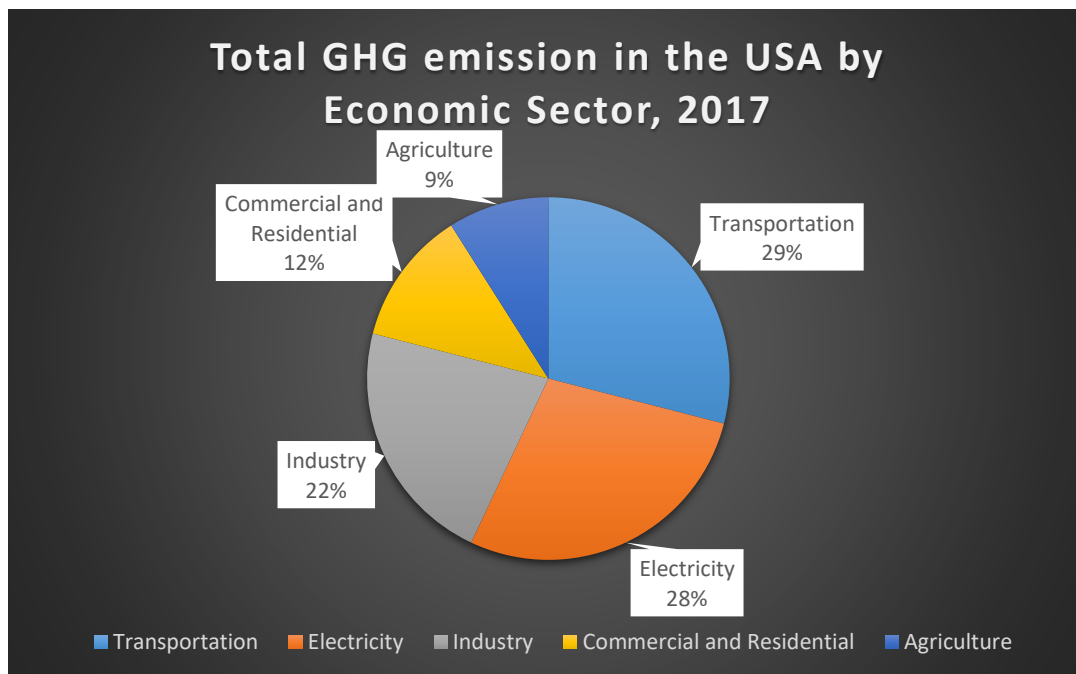
Figure 1.4: Percentage of total emissions in 2017 (EPA, 2019).

Indirect emissions for the industry come from burning fossil fuels at power plants to supply electricity to industrial facility. Like industrial sector, the commercial and residential sector contribute to GHG by direct and indirect emissions. Direct emissions come from burning of fossil fuels for cooking and heating food at home along with leakages in refrigerants from homes and commercial shops. Indirect emission is produced from power supply provided to homes and businesses. Agriculture only contributes up to a miniscule level of GHG emission. These emissions are produces mainly from the soil which emit nitrous oxide. Livestock's such as cattle produce methane. Hence agriculture is only a small source of GHG when compared to transport which is the main contributor to GHG (EPA, 2019).

Transportation support increase in mobility but on the other hand they have direct impact on the environment with increase of carbon particulates and congestion (Sharma & Kumar, 2012). With the ever-expanding transport industry there has been a direct, indirect and cumulative impact both on the environment and living mankind. For instance, some of the direct impact are noise and carbon monoxide emission. Indirect impact is caused when the particulates are emitted from exhaust of vehicles to cause cardiovascular problems. The cumulative effect of this is the impact on the environment resulting in climate change along with several natural and anthropogenic factors (Paul, 2017). Figure 1.5 shows the percentage share between different sectors of the transportation industry with road transport contributing to nearly 74% of the GHG emissions. The current study focusses on trucks which are the major source of transport for the road sector and as a result contribute the most towards GHG emissions.
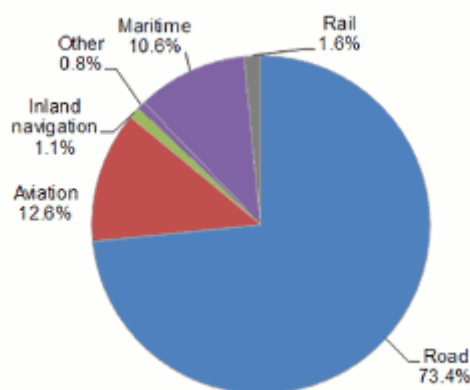
Figure 1.5: Percentage of GHG emission by transport sector (European Commision, 2017).

Chapter 2

Literature Review

2.1 Introduction about Trucks

Trucks, known as lorries, are motor vehicles with a sole purpose to carry freight and goods. Trucks carry utmost amount of goods between intercity which are aided by well-developed highways system in North America and Europe. Trucks are the preferred mode of transport for any freight it could carry since they enjoy the liberty of delivering goods directly to the recipients (Easton & Cromer, 2019). Trucks can be classified into two categories based on the construction of their carriage as either straight or articulated. A straight truck is one where all the axles of the truck are attached to one single chassis or frame. An articulated truck is one which consists of two separate chassis which are connected at the bridge (Easton & Cromer, 2019). A pictorial description of the two trucks cans be seen in the Figure 2.1 and 2.2.

An articulated truck can carry more load than a straight truck. This is simply because the chassis of an articulated truck is bigger in terms of a load capacity. So, it could carry more and heavier freight when compared to a straight truck. An articulated truck is also low on maintenance combined with more revenue and more load options. These trucks are also low on emission per unit cargo transported. They prove to be a very good cost-effective solution to reduce emission from other road freight making efficient use of the infrastructure (High Capacity Transport, 2019). These trucks also have a higher range of flexibility since the trailer units can be exchanged between trucks (Allen, 2019).

Content removed due to copyright reasons.

Figure 2.1: Example of straight truck (Wolenski, 2017).

Content removed due to copyright reasons.

Figure 2.2: Example of an articulated truck (Renault Trucks Optifuel Lab 3 aims to reduce heavy-duty diesel truck fuel consumption by 13%, 2018).

Nowadays automobile manufacturers are competing to design a powerful but also aerodynamic truck with better fuel efficiency. This market is highly regulated with strict fuel emission norms. The need for bigger size truck with higher horsepower and cargo is also a major demand from truck owners. Designing energy efficient trucks, whereby reducing the total structural mass, improving the thermal efficiency of the engine or altering the exterior body shape to reduce the aerodynamic drag, are some of the changes considered by some of the leading truck brands.

A constant need to better the fuel economy of a vehicle and its performance in the long run has been the goal of any auto maker. One way to achieve is to improve the aero performance of a vehicle, to reduce wind noise levels and to improve the grip levels and stability of a vehicle. This has laid the foundation for vehicle manufacturers to investigate the physics behind air resistance or drag of different body shapes under different operating conditions.

2.2 Types of Trucks

The dimension of these heavy-duty trucks varies depending on the region in which they operate around the world and the type of payload they carry. These dimensional regulations are usually laid out by the government. Trucks in the United States have no maximum length but, however, must adhere to minimum trucks length. The minimum allowable length of a trailer unit is 14.63 meters. This applies to the overall length of the truck, which includes the tractor and trailer units. A truck in the US can have more than one trailer unit, typically called a road train (US department of transportation, 2001). Road trains are however common in Australia. This means a typical Australian truck consisting of 22 tyres, which is much higher than their counterparts in other countries as seen in Figure 2.4. In total these road trains in Australia have up to four trailers and can be measured up to 53.5 meters in length (Wikipedia, 2019). Trucks in the Europe are restricted about a dimension and weight they can carry in order to prevent road from damaging and to ensure road safety. The maximum allowable length of a truck in Europe is 18.75 meters (measured from the front of the tractor to the rear of the trailer) as seen in Figure 2.5 (European Commission, 2016). Trucks in China have a similar regulation with their maximum truck dimension at 17.10 meters (Quang, 2019).

Content removed due to copyright reasons.

Figure 2.3: Schematic depicting some of the major part and length of a truck measured in US (US department of transportation, 2001).
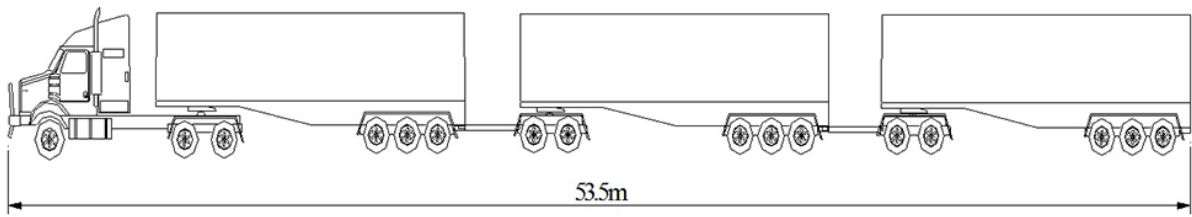
Figure 2.4: Length of a road train measured in Australia (Oversize or overmass vehicles, 2020).
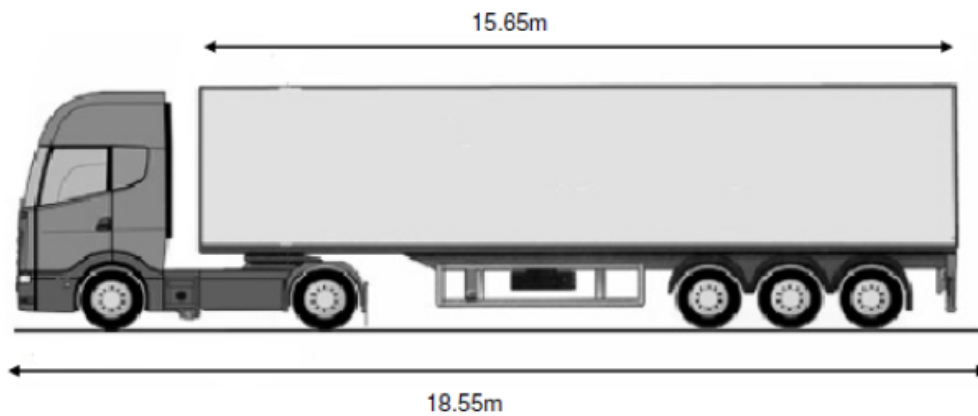
Figure 2.5: Schematic of truck length measured in Europe (Cuotto, 2016).

In order to carry maximum allowable cargo on these trucks, the load-carrying trailer is preferred to be as big as possible. Hence the tractor is made as small as possible to seek out maximum space for the trailer from the allowable total length. Tractor sizes across brands do not vary much. A typical tractor width would vary from 2.3 meters to 2.5 meters and the length can vary from 2.225 meters to 2.3. A top view of a typical tractor with dimensions is given in Figure 2.6. With these dimensions, the tractor can house two seats (driver and passenger), a bed and a dashboard with a total area of $6m^2$ (Cuotto, 2016). On an average the speed limit of trucks across Europe is 85 km/hr with some countries having speed limits as low as 60 km/hr and some countries having speed limits up to 112 km/hr (Motorway standard speed limits in Europe, 2015). This PhD project focuses on aerodynamics flow around a truck with a single trailer unit attached to the tractor.

Content removed due to copyright reasons.

Figure 2.6: Tractor dimensions (Cab specifications for Volvo FH, n.d.).

2.3 Introduction to Heavy Vehicle Aerodynamics

To better understand the importance of aerodynamics of trucks, it is important to understand the breakdown various modes of transport into air, maritime and road transport based on power consumption. Figure 2.7 below shows the importance of road transport which requires more than 70% of engine power to overcome aerodynamic drag making it the highest contributor to GHG emissions. Aerodynamic drag force acts on any incoming solid body in the direction of the fluid freestream flow (Anderson, 2005).

Content removed due to copyright reasons.

Figure 2.7: Power share across different modes of transportation to overcome aerodynamics drag (Minelli, 2017).

Reducing aerodynamic drag through careful shaping of trucks have been experimented over the years by designers using trial and error method. Proposals to streamline air flow around a vehicle was first implemented in 1914 (Saltzman & Meyer, 1999). In the 70's the world was hit with oil crisis which stimulated the development of add-on devices which could be fitted to existing trucks. This led to more research on improving the shape of vehicles for the future. Until recently, there has been limited consideration in size and shape of large trucks. The shape and size are primarily determined by the amount of payload.
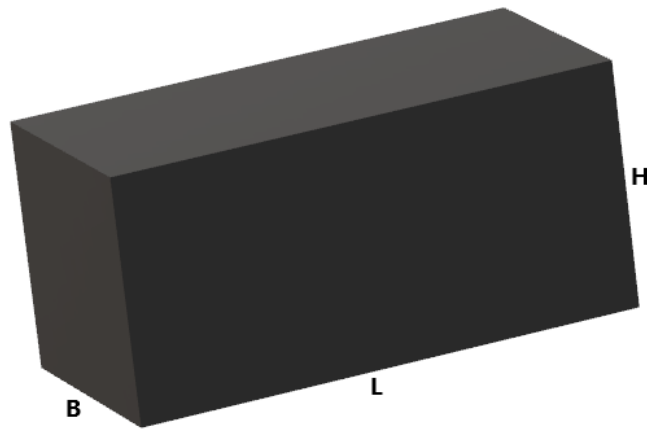
Figure 2.8: An example of a bluff body

For trucks
$$1 > \frac{H}{L} > \frac{B}{L}$$
2.1

In Figure 2.8, H is the vehicle height, L the length and B the width. The above equation 2.1 shows that the width of the truck is less than its height. This is primarily due to the type of payload trucks carry. There are some mid-size trucks which are wider than their height, but these kinds of trucks come with a hefty loss on their payload. Hence, recent light on truck development has been shed towards streamlining the vehicle body itself. The rounding of the leading edges for the tractor and trailer can reduce drag by a substantial amount. The degree of bluntness of on the front face of truck is determined by the radius of curvature at the leading edges. The optimal radius can be determined by experiments. However, the importance of leading-edge rounding can be seen in the Figure.2.9 below for a simplified tractor trailer model. The tractor with sharp edge tends to experience high leading-edge separation in Figure.2.9a when compared to tractor with curved front edge which experiences lower flow separation in Figure.2.9b. Hence the tractor with curved leading edge tend to generate lower drag coefficient.
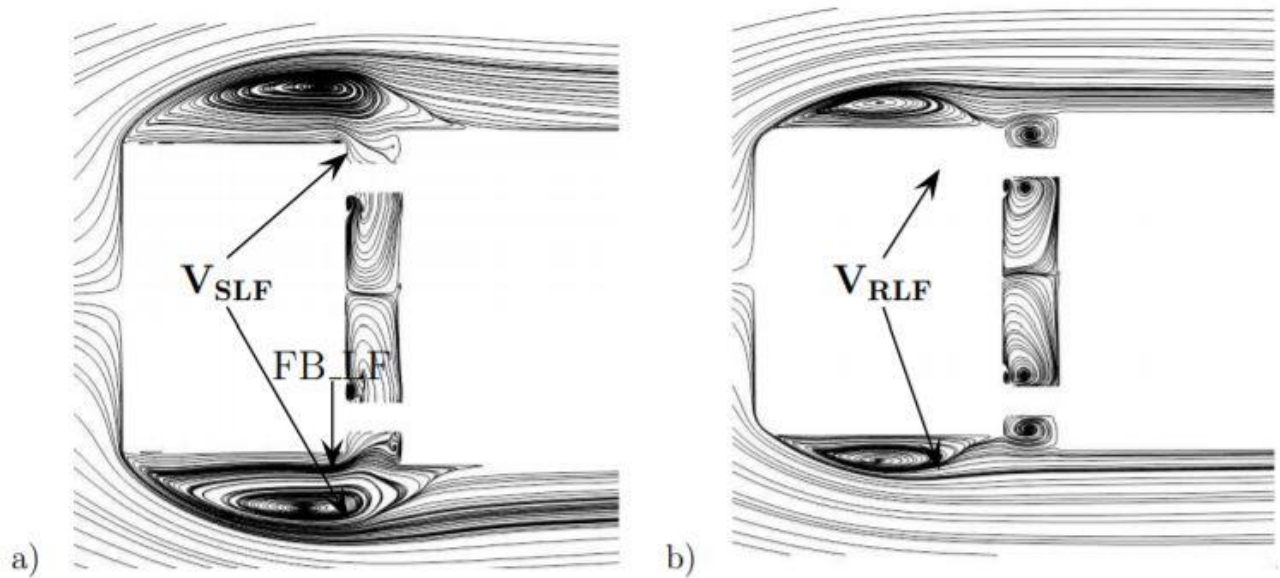
Figure.2.9: Change in flow field due to front edge rounding (Osth & Krajnovic, 2012).

Aerodynamic drag for any model increases with the square of the vehicle speeds. A complete relation between aerodynamic drag and vehicle speed is given in the equation below.

$$F_D = \frac{1}{2} C_d \rho A v^2 \qquad\qquad 2.2$$

where F_d is drag force, C_d is the drag coefficient, ρ the fluid density and A its frontal area. A pictorial representation of the projected frontal area is given in Figure 2.10. In order to determine the drag force
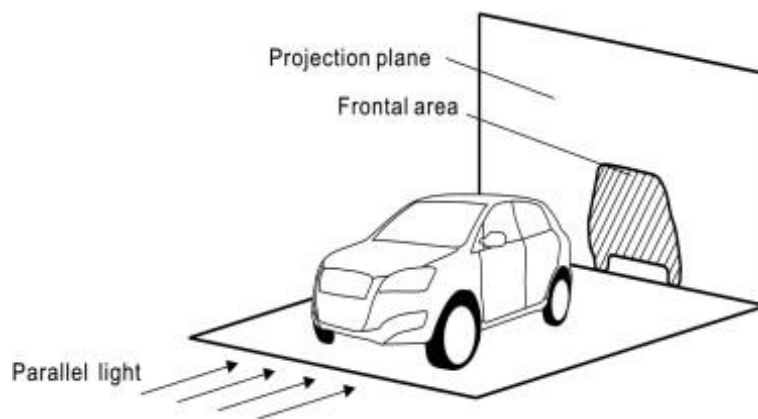
Figure 2.10:Vehicle projected frontal area (A) (Wu & Liu, 2011).

Since aerodynamic drag plays a crucial role in automotive aerodynamics, it is important to understand the difference between a streamlined body and a bluff body. When a streamlined body is kept in a fluid flow, it gives rise to a smaller wake which produces a low value of drag. When considering a bluff body, the wake characteristics is determined by the size and shape of the body. Hence the drag coefficient may vary depending on the flow around the body itself. Examples of streamlined and bluff bodies are given in Figure 2.11 & 2.12. All road vehicles especially trucks and buses are considered as bluff bodies. This is because of the large wake in combination with the separated flow on the edges produced by buses and trucks. To understand the importance of aerodynamics, every time a flow detaches from the surface of a bluff body, the coefficient of drag increases (Wood, 2006). An example of flow separation can be seen in Figure 2.13.
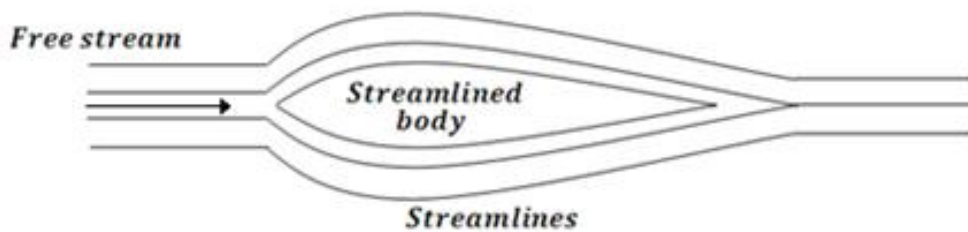
Figure 2.11: Flow field around a streamlined body.
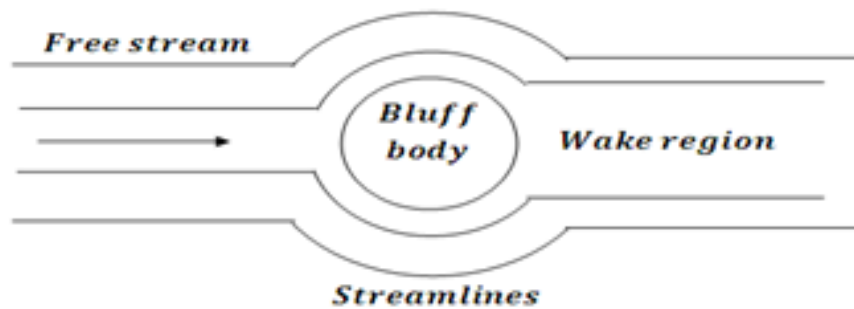
Figure 2.12: Flow field around a bluff body.
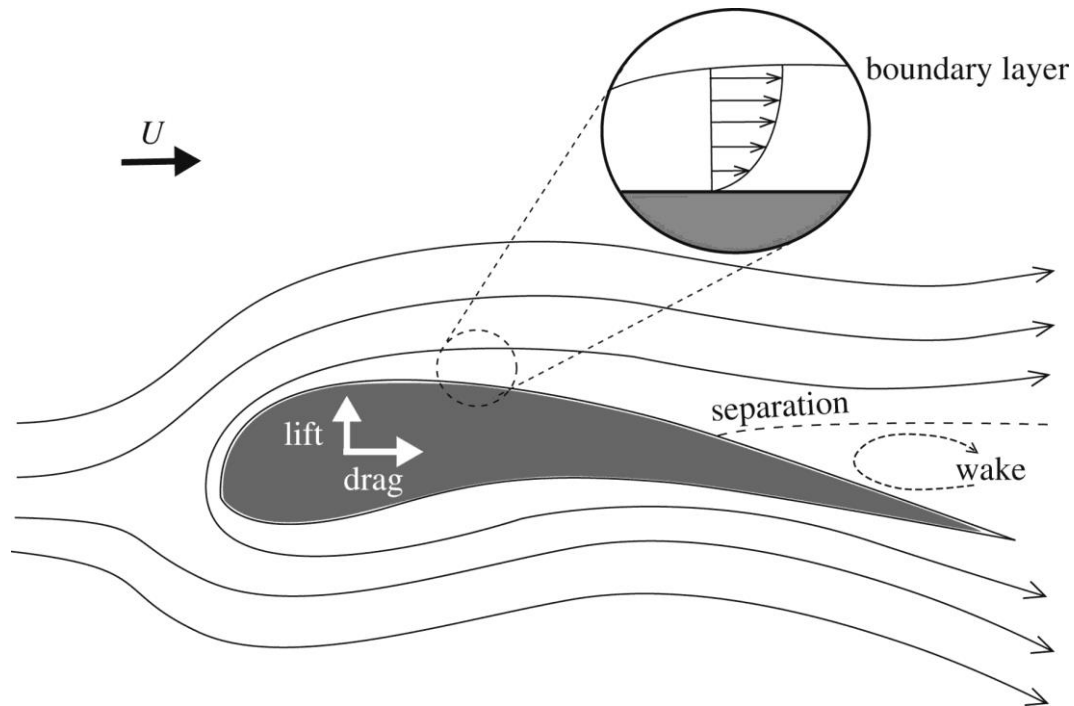
Figure 2.13: Flow separation as seen near boundary for an aerofoil at an angle (Thiria & Diana, 2018).

All flows around a road vehicle are categorised as bluff body flows. When considering a vehicle, drag is often increased by flow separation at the front or at the rear or both. With modern vehicle designed in a streamlined manner, there are still significant flow separation which takes place the rear, gap in body panels, underbody and roof. In general, the vehicle shape influences the air flow around itself, responsible for aerodynamic forces. Physical variables like velocity and pressure field around the vehicle affect the direction and magnitude of various aerodynamic forces including moments such as drag force and lift force, side and rolling moment.

The job of aerodynamicists and researchers is to investigate solutions to improve the aerodynamic performance of a vehicle. The primary objective from this is to reduce the aerodynamic drag of vehicle either by changing the shape of a vehicle and also by controlling the flow to ideally reduce flow separation around the body. Buses and trucks have a natural rectangular shape due to the type of payload carried by the vehicle. A truck can be represented by one rectangular block and a semi-truck can be represented by two rectangular blocks where the first block represents the tractor and second box represents the trailer. The front face of a tractor had substantial design improvements carried out over the years in order to reduce aerodynamic drag. One significant improvement carried over is the rounding of the edges as shown in Figure 2.14.
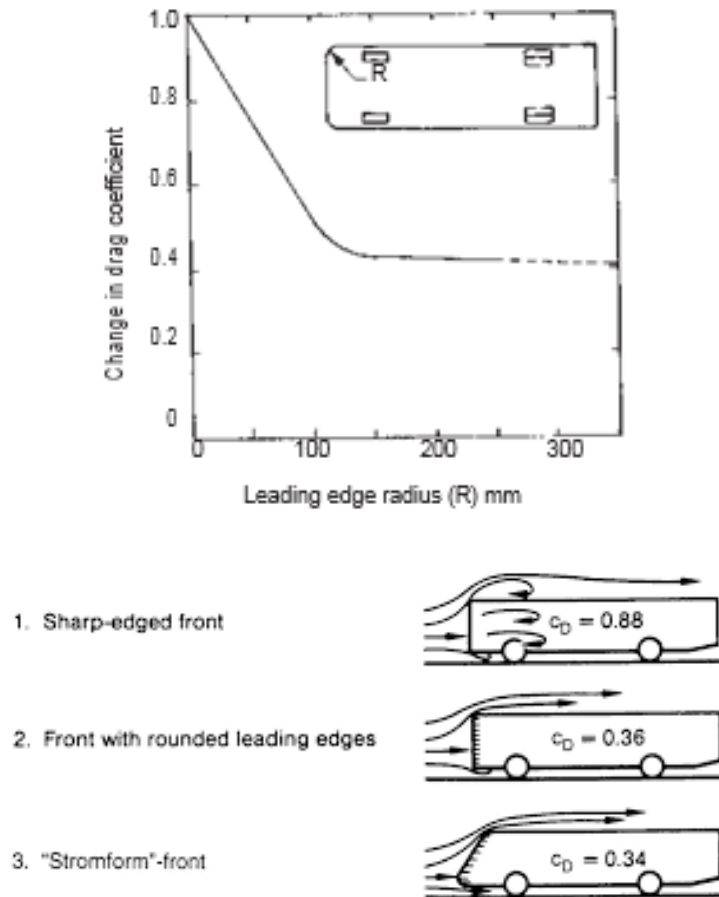
Figure 2.14: Effect of front edge rounding and drag coefficient for a typical simplified bus shaped test case (Hucho, 1998).

In Figure 2.14, the model with sharp edge has more than 50% higher drag coefficient when compared to the model with Stromform front. This is due to the flow accelerating over a curved surface. The accelerated flow thrusts a lower pressure on the curved surface. With an increase in radius to the edges, the exposed area in the streamwise direction also increases, this will lead to reduction of overall drag of a model. The overall drag coefficient of a vehicle is around 0.7, out of which 0.2 comes from the front, gap between tractor and trailer, wake behind trailer and 0.1 comes from the tires. Several devices have been implemented on a modern tractor-trailer to reduce the aerodynamic drag. Some of the most common examples are the roof deflectors, gap fairings and side extenders. These aerodynamic aids have proved to improve the flow field around a truck significantly. Several other techniques have been implemented to control the flow using cavities, boat tails and shaped actuators (Alti, et al., 2012) (Khaligi, et al., 2001) (Verzicco, et al., 2002) (Coon & Visser, 2004).

2.4 Types of Articulated Trucks

The shape and size of trucks are primarily the result of their function and legal constraints along with the aesthetics and tradition which have played an important role. Load carrying capacity have been the focus with aerodynamic characteristics only a by-product. Depending on the type of load being carried, the shape of a vehicle has been aerodynamically bluff rather than a more streamlined or efficient design. When considering trucks, there exists several different shapes for the trailer which are primarily classified based on the type of usage: Semi-trailer, dump truck trailers, tanker trailer and road trains or long combination vehicle. A pictorial representation of semi-trailers, dump trucks and tanker trailers are given in Figure 2.15, Figure 2.16 & Figure 2.17. Besides the above types there are also other types of trailers like flatbed trailer, car carriers and low boy trailers. Each of these trailers is designed specific types of cargo.

Majority of freight around the world is hauled by trucks which have two distinct and separate modules - a tractor and a trailer. Generalisation of a model is an easier approach since it utilised for research purpose and a general model gives a good reference point for production trucks. A semi-trailer can be split in two different sections which comprises of the tractor and the trailer. The two are connected by a bridge. For simplicity, we will be calling semi-trailer, tractor-trailer combination vehicles are 'Trucks' for the rest of the thesis.

Content removed due to copyright reasons.

Figure 2.15: Typical Semi trailer (Truck).

Content removed due to copyright reasons.

Figure 2.16: Example of dump truck trailer.

Content removed due to copyright reasons.

Figure 2.17: Example of tanker trucks.

2.5 Drag Coefficient

Drag coefficient is a universal term which defines the aerodynamic efficiency of a vehicle. The aerodynamic drag is a minor factor at low speeds but the magnitude changes with increase in speed. The force a moving vehicle needs to overcome aerodynamic drag increases with the increase in speed. There is also other resistance on a vehicle like tire rolling resistance and driveline friction effect. Drag coefficient along with rolling and driveline resistance can be seen in Figure 2.18. The rolling resistance remains a constant flat line while the aerodynamic drag resistance increases with the increase in speed. Along with drag, several other forces act on a vehicle locally like lift, side forces and moments are important.
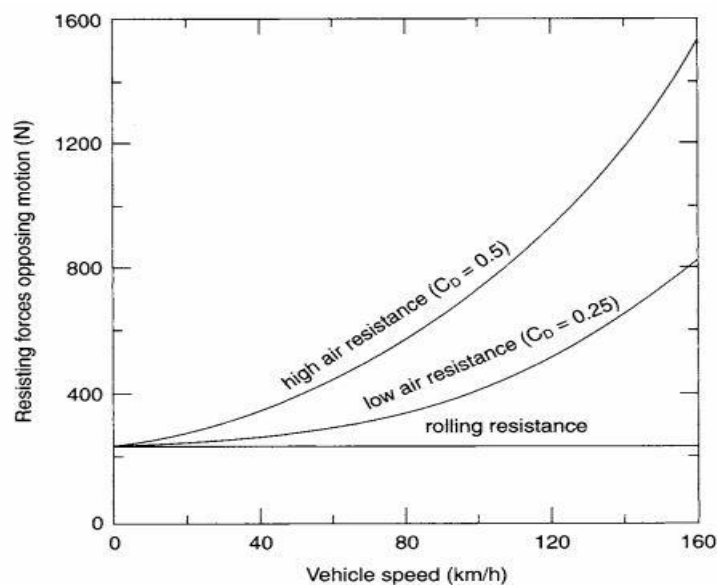
Figure 2.18: Comparison between drag coefficient and rolling resistance at difference vehicle speeds (Heisler, 2002).

The general concept of aerodynamics drag force is that it works against the intended or the desirable direction of vehicle. Almost every object experience drags in some form or the other. Aerodynamic drag force is the force which resists the movement of a body through a fluid medium. Drag is exerted in the form of pressure or friction. Hence the design of the vehicle is crucial to overcome drag but also not affect the payload of the vehicle. An aerodynamic design incurs drag that is less than the bluff body design. If an object is streamlined well enough, it is possible to achieve zero drag. Aerodynamic drag increases with the square of the vehicle velocity between the vehicle and surrounding air. When the vehicle travels through still air, increasing the vehicle speed by double will quadruple the aerodynamic drag coefficient of the vehicle. Engineers came up with a non-

dimensional number called drag coefficient which quantifies to how much a vehicle aerodynamically efficient. The drag coefficient of a vehicle is given by the equation below.

$$C_d = \frac{F_D}{0.5\rho U^2 A}$$

<div align="right">*2.3*</div>

Here, F_D is the drag force exerted on the vehicle, ρ is the fluid density, U is the velocity of fluid or vehicle speed, A is the frontal area.

Heavy vehicles are aerodynamically inefficient when compared to other ground vehicles. This is primarily due to large frontal area and bluff body shape. Due to their large bluff body like shape, trucks require a lot of energy to overcome aerodynamic drag (Croll, et al., 1996). A typical truck would usually travel in two different roads, namely urban road and motorways. Hence there exists a shift in the resistance the vehicle undergoes when commuting in these two environments. Under urban conditions, the mechanical losses of the vehicle are a dominant factor and when the truck is cruising in a motorway the aerodynamic losses become a dominant factor. However, the mechanical losses of a truck are an almost linear increase with vehicle speed. Table 2.1 shows the different source of resistance and losses for a truck operating in urban and motorway conditions. From the aerodynamic data in Table 2.1, a truck experiences an aerodynamic loss of 10%-25% based on the speed of the truck while operating on urban roads and 35%-55% while operating in motorway conditions. The increase in aerodynamic loss is due to the increase in vehicle speed between urban and motorway conditions.

Content removed due to copyright reasons.

Table 2.1: Engine power required to overcome different loses for a class 8 truck operating at urban and motorway conditions (Belzile, 2012).

The above data was taken from trucks which had properly inflated tires and internal power losses assume to a linear function of vehicle speed. Aerodynamic drag is one of the sources of fuel consumption and it is important to understand the effect it has on trucks. Partly because trucks spend most of their cargo hauling hours on the motorway where they cruise at motorway speeds. The various losses a truck undergoes at different speeds is given in Table 2.2. A truck cruising at 80km/h can achieve about 10% reduction in fuel consumption if the total aerodynamic drag of the truck is reduced by 20%.

Content removed due to copyright reasons.

Table 2.2: Engine power required to overcome losses for a class 8 truck at different vehicle speeds (Belzile, 2012).

Content removed due to copyright reasons.

Table 2.3: Percentage of fuel saving achievable with drag reduction at different road conditions (Hucho, 1998).

In equation 2.3 for drag coefficient given above, it is a function of vehicle speed, cross section area and force exerted. However, the drag coefficient of a vehicle is a combination of number of factors related to the vehicle and environment in which it operates. Some of the factors which influence drag coefficient based on vehicle and the environment are given below. Table 2.3 gives the fuel saving which can be achieved by reducing drag on different operating road conditions. The exact fuel saving for the data given in Table 2.3 is dependent on the type of truck and speed limit on the motorway.

2.6 Breakdown of Drag Distribution around a Truck

A truck geometry has many aspects to contribute to drag force. Whenever a flow detaches from the surface of a truck, the drag coefficient C_d of the vehicle increases. To better understand the economy payoff and technical challenge due to aerodynamic drag generated around a truck, it is necessary to understand the drag distribution around a truck. Drag source/distribution around a truck can be classified into the following regions:

1. Truck geometry.
2. Front face of tractor
3. Gap between tractor and trailer.
4. Under body of trailer.
5. Rear end of trailer.

A schematic representation of percentage drag regions around a semi-trailer are given in the Figure 2.19.
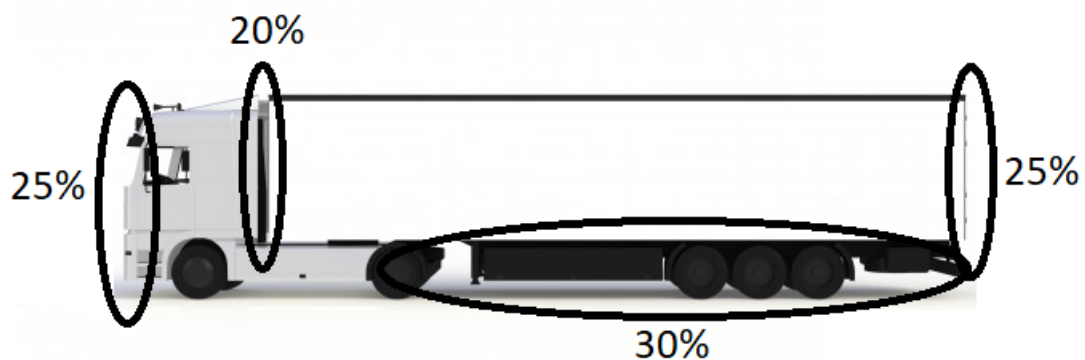
Figure 2.19: Graphic depicting percentage of drag generated at different regions around a truck (Wood, 2006).

The graphic depicts the dominant drag distribution around a truck. The flow field at the fore body of a semi-trailer is complicated when compared to a bus. This is because the tractor and trailer have two major forward-facing surfaces due to their two-body configuration and hence they are considered as two separate bluff bodies with the tractor shielding a large portion of the trailer.

Factors affecting drag coefficient due to vehicle:

1. Tractor design
2. Trailer design and configuration (Boxy shape, flatbed, dry bed etc.)
3. Gap between the tractor and trailer.
4. Accessories (Mirrors, deflectors, side skirts etc.)

Environmental factors:

1. Wind properties (directions, velocity and turbulence)
2. Air properties (Temperature, pressure and humidity)

In order to assess a vehicle, drag, wind averaged drag is an important metric value because some of addon drag reduction devices used on a truck are typically developed at zero yaw angle. Hucho (Hucho, 1998) had stated that there are two main mechanism which is closely related to aerodynamic drag around road vehicle. These two mechanisms are skin friction and pressure which acts normal to the surface of the body. Both these mechanisms are illustrated in the Figure 2.20.

2.5.1 Skin Friction Drag

It is the component which acts parallel to the surface of a vehicle resulting in shear and viscous effects which takes place between the surface and the layer of fluid immediately above it. The above is mainly due to momentum transfer from the fluid molecules to the surface of a near wall region. When a solid object is kept in a fluid flow, a layer of fluid immediately next to the surface may become attached to it. This results in shearing taking place between the layers of fluid. The stress acting between the first moving fluid layer and the wall is called wall shear stress. The drag due to skin friction is typically less than 20% of the total drag (Hucho, 1998) (Ahamed, et al., 1984). Skin frication drag is so small that when changing the geometry of the vehicle, skin friction drag remains a constant (Howell & Good, 2008) (Perry, et al., 2015). Alternatively, skin friction can also be directly proportional to the wetted area of the geometry (Varney, et al., 2017).

$$D_f = \oint (\tau . cos\theta) dA \qquad \qquad 2.4$$

where D_f, the drag due to skin friction, τ is the shear stress (Pa), θ is the angle to the drag axis, dA is the area over which τ is acting.

2.5.2 Pressure Drag

Pressure drag is generated by resolving force components due to pressure acting normal to the surface at all points. Pressure drag is computed as an integral of flow direction component of pressure forces acting at all point on a body (Houghton & Valentine, 2015). Pressure drag has several distinct causes like induced drag, wave drag, and form drag. The shape of the body can determine the level of pressure drag generated. The most forward face of any vehicle will have the stagnation point where the velocity of the flow is zero and perpendicular to the face as shown by the arrow in Figure 2.20. The rear of the model creates a considerably large wake. The suction of the flow from the base of the model occurs due to a fixed separation point at the rear face of the model or due to strong adverse pressure gradient. The wake region consists of a velocity which is lower than the actual free stream velocity and flow reversal resulting a low-pressure wake.

D_p drag due to pressure is given by:

$$D_p = \oint (P.sin\theta)dA \qquad\qquad 2.5$$

Where P is the pressure normal to the surface.

.
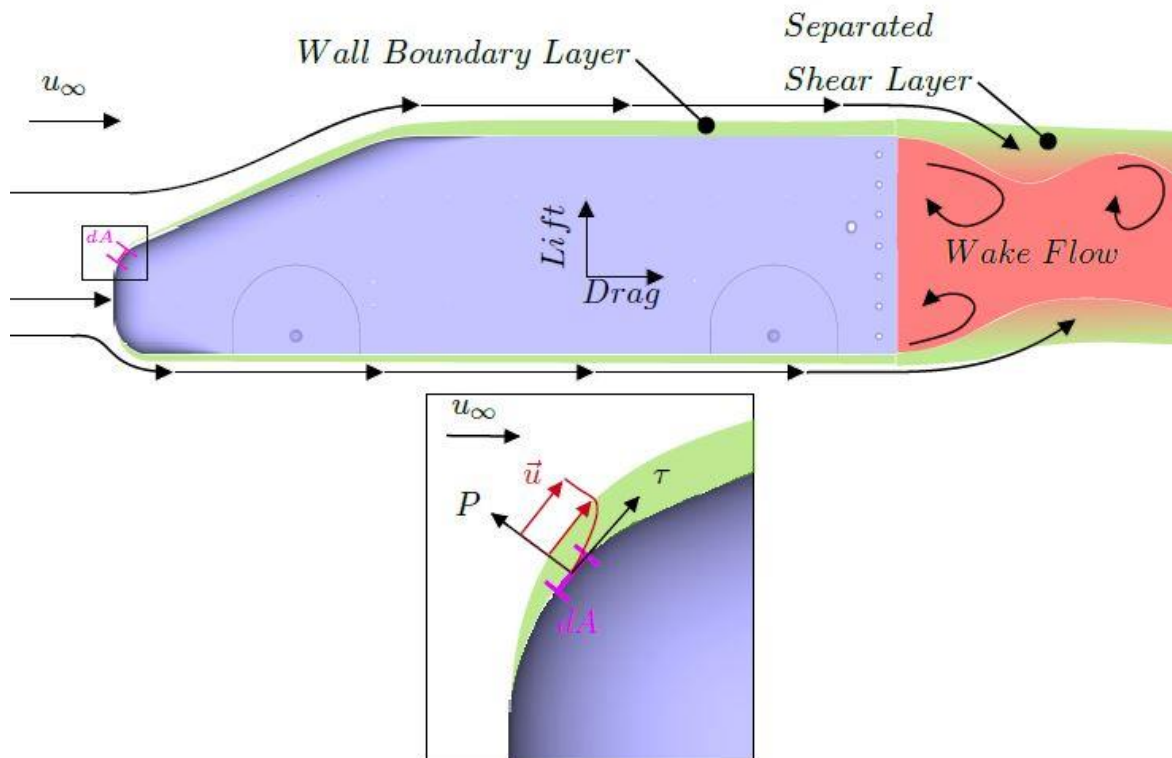
Figure 2.20: Schematic showing normal and shear pressure drag around a square back Windsor model (Varney, 2018).

The pressure exerted on a model is highly dependent on the shape of the model. This pressure is highly dependent on the Reynold number (Bearman, 1997) given in the equation below. At a Reynold number ≤ 1000 a cylinder can undergo several flow regimes. The boundary layer over the cylinder can be laminar. A laminar boundary layer creates a flow separation which is before the top dead centre as illustrate in Figure 2.21a. This creates a large wake and a high drag. With increase in Reynolds number, the point at which the transition to a turbulent boundary layer would occur moves upstream. Figure 2.21b, flow separation has occurred well past the top dead centre. This kind of transition usually occurs over a Reynolds number of 2×10^5. As a result of higher Reynolds number, the wake is much smaller combined with a lower drag for the cylinder (Hummel, 1987).

$$R_e = \frac{\rho . u . L}{\mu} \qquad\qquad 2.6$$

In the equations, L is the length of the model (m), μ is the dynamic viscosity ($Pa.s$).

(a)   (b)
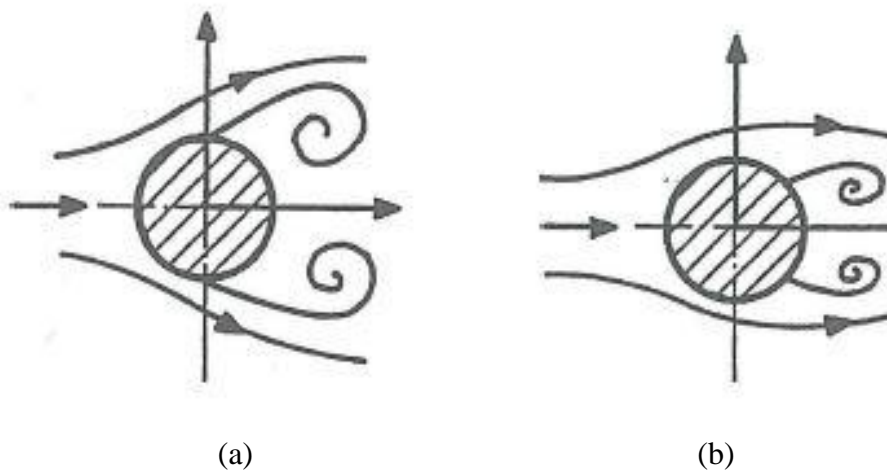
Figure 2.21: Schematic of flow field around a cylinder. (a) Pre critical Reynold number. (b) Post critical Reynold number (Hummel, 1987).

Considering three-dimensional flow, bluff bodies or an automotive model, the shape of a body has significant influence on the pressure drag which the model could generate. Bearman (Bearman, 1997) states that the vortices in the streamwise direction dominate the wake region of 3D flow. When comparing this to 2D flow, the wake region is dominated by spanwise vortices. A close relation has been identified in other literature from Ahmed (Ahamed, et al., 1985) (Hanfeng, et al., 2016) (Grandemange, 2013) and Windsor geometry (Howell, et al., 2013).

For heavy vehicle like trucks, busses and long combination vehicle, pressure drag makes up the dominant force exerted on a vehicle body. This is due to their large surface area being perpendicular to the main flow direction and in combination with the large wake at the back end of a vehicle. In terms of a semi-trailer, the pressure forces which act on the front, gap region, back end and the base of the vehicle play a dominant role.

For road vehicle friction drag is very minimal or close to negligible. Their contribution to the overall drag of a vehicle is miniscule when compared to pressure drag. In order to reduce pressure drag around the entire truck, the aerodynamicist is also responsible to control the 6 degree of motion as shown in Figure 2.22 like yaw moment, roll moment, pitching moment, vertical or lift force, lateral and longitudinal forces (Englar, et al., 1996).
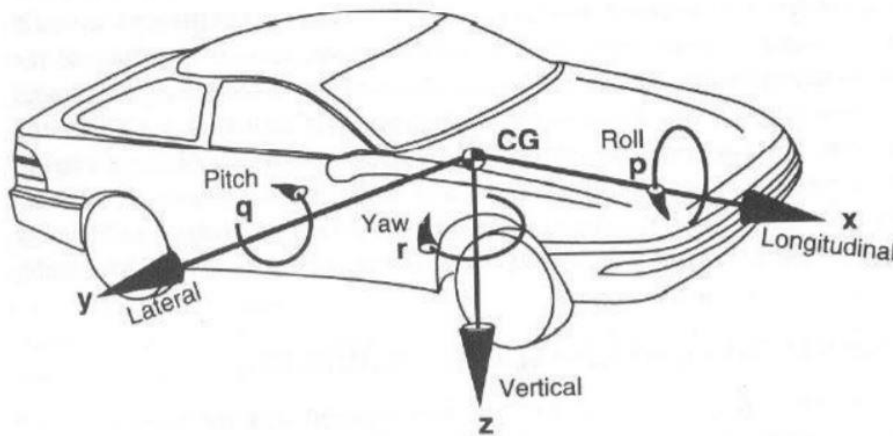
Figure 2.22: Example of 6 degrees of motion for a car (Larson, 2011).

Drag around road vehicle is highly influenced by the degree of bluntness of the front end. Hammache et al (Hammache & Browand, 2004) conducted experiments on the GTS model with two different leading-edge curvature. The author conducted experiments to find the optimal radius of curvature, measuring drag based on inlet velocity, Reynolds number and cross-sectional area. The significance of leading-edge rounding can be seen in Figure 2.23 for an isolated tractor based on the cross section of two mean values of front radius of curvature. Plotting the same data against Reynolds number based on front radius curvature in Figure 2.24, the two curves can be seen close to each other. Drag coefficient can be seen becoming a linear curve from Re = 70,000 onwards suggesting that the flow is not prone to leading edge curvature above a critical Reynold number. Hence it can be concluded that any further rounding is not going to reduce drag coefficient any further.
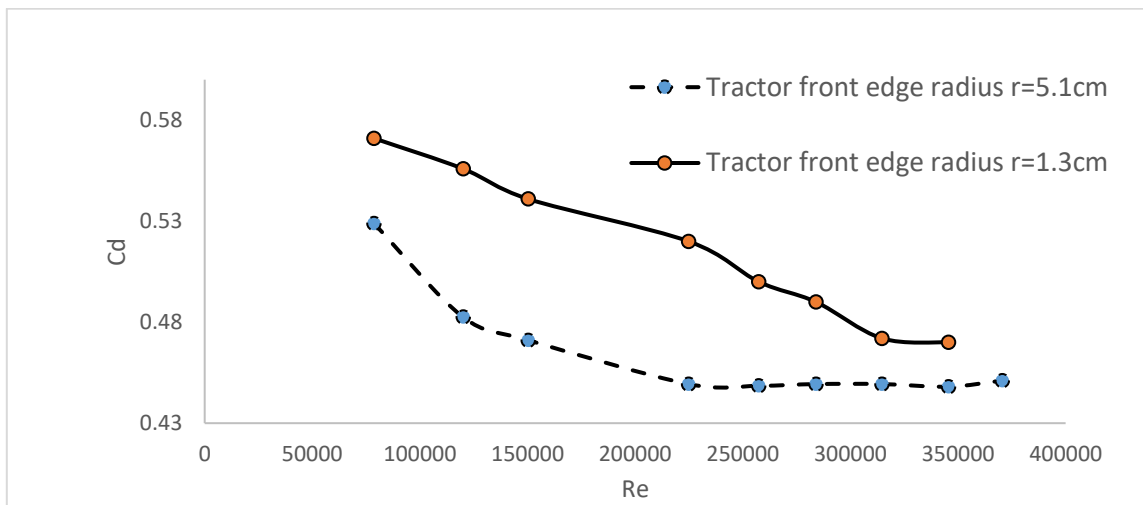
Figure 2.23: Drag coefficient vs Reynold number (Hammache & Browand, 2004).
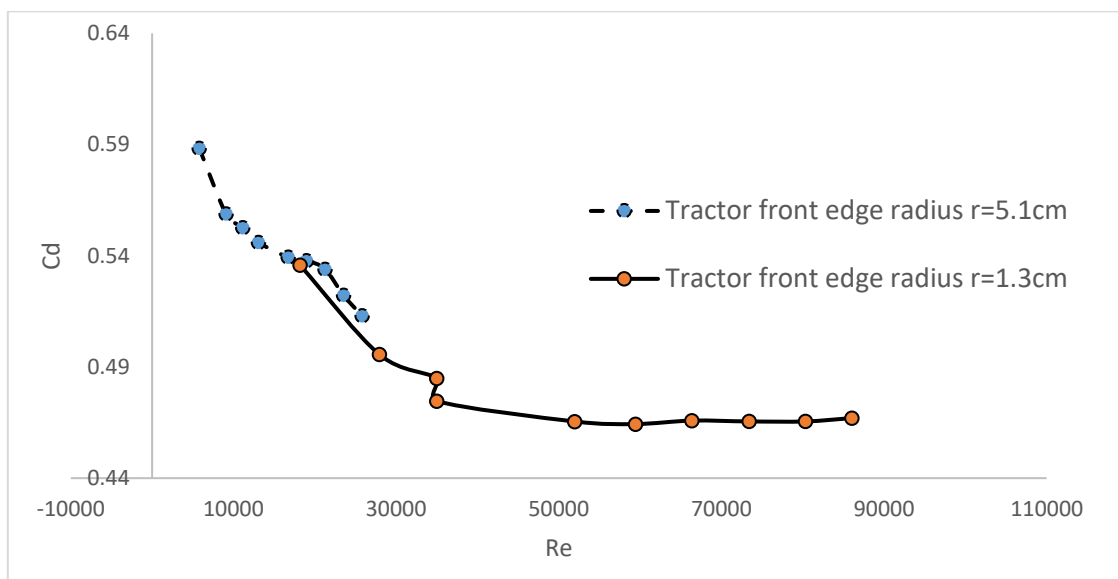
Figure 2.24: Drag coefficient on an isolated tractor as a function of Reynolds number based on the front edge radius curvature (Hammache & Browand, 2004).

In the recent decade, the aerodynamic optimization with respect to performance and geometry of a truck have received an increased attention and a number of studies have been conducted to reduce aerodynamic drag (Hyams, et al., 2011) (Croll, et al., 1996). For a truck driving on the highway, nearly 45% of the total drag is from the cab alone (Cooper, 2002). Hence the shape of the cab can determine the flow field around the rest of the truck. For example, a sharp edged cab takes the full air drag and ends up completely shielding the rest of the truck behind it because of the distinct

separation of flow, which could lead to the rest of the truck experiencing zero drag or partial drag (Hucho, 1998).

Tractors operate with a variety of different trailers. Low drag of the cab alone does not necessarily guarantee low drag for the entire truck. Hence add-on devices which reduce drag for the trailer should work in combination with the flow field around the truck. Add on devices in order to improve the aerodynamic flow field of a vehicle have been used extensively in modern tractor trailer for several decades. With oil crisis in the 1970's, a demand for energy efficient transportation of heavy vehicle emerged which led to extensive research in 1970s and 80s to improve the aerodynamic characteristics of trucks (Cooper, 2002)

2.7 Aerodynamic add on Devices

Much research has focused on developing drag reducing devices for existing cab shape and insufficient effort have been given to optimizing the shape of the cab itself. The approach of optimizing the shape of the cab comes at an additional cost however it avoids the use of pneumatic accessories (roof deflector, side extenders, boat tail etc) which adjust the height and width of several aerodynamic devices to aid the reduction of aerodynamic drag (Peng, et al., 2018). Further to the already existing drag reduction techniques, some of the major commercial vehicle brands like Scania, Volvo or the Tesla semi electric tractor trailer have begun exploring new styling to optimise the styling and designs of the cab to reduce the aerodynamic drag force of tractor and trailer.

Add-on devices have been extensively used on trucks to improve the air flow around them. When the oil crisis in the 70's began, an increase in effort to improve the efficiency of truck became the centre of focus in the 70's and 80's. Unlike a car, the shape and size of commercial vehicle are determined by the type of payload and cargo they carry. A typical truck carries a cuboid shaped trailer for most of the freight hauling time. In order to carry the maximum allowable load possible and to satisfy regulations from local governing bodies, aerodynamicists have very limited possibility to modify and reshape the load carrying part of a vehicle (Hucho, 1998).

The tractor units of trucks can be classified into two types, (a) Cab behind engine and (b) Cab over engine. For a cab behind engine the tractor is generally longer in length than a cab over engine tractor. A pictorial representation of the two-cab design is given in Figure 2.25 & Figure 2.26. The width of a cab behind engine is usually smaller than the width of a trailer unit (Obidi, 2004). Trucks have tremendously been redesigned and modified in the last few years. From sharp edges to flat front faces of tractors, we now have rounded edges and less of a flat front which have improved fluid flow around the tractor. The most common examples are roof deflectors and side extenders, which tremendously improve the aerodynamic efficiency of a truck (Obidi, 2004) (Kuo & Mehta, 2005) (Imam, et al., 2011) (Mason & Beebe, 1978) (Hammache & Browand, 2004).

Several aerodynamic measures integrated on trucks with Cab behind engine are not directly transferable to the Cab over engine trucks. This is mainly due to the aesthetic design of these trucks which have been introduced by different legislations in countries where these trucks operate. As discussed earlier in (Dimensional regulation of trucks) trucks in US have freedom to manage the overall length of the trucks when compared to the Europe where the entire length of the truck must be within certain dimension. Hence truck operators in the US have the liberty to modify the length

of tractors (Hariram, et al., 2019). Flap used on trailing edge (Alti, et al., 2012), underbody flow treatments (Pankajakshan, et al., 2007), side skirts and boat tails (Wood & Bauer, 2003) and few other add on devices have been trialled and investigated in recent times. The primary focus of these devices is to delay flow separation and thus directly reduces the effect from the wake. These devices are called Passive drag reduction devices. Some of these techniques have been applied widely with various success. These devices are known to work under any type of climatic condition.
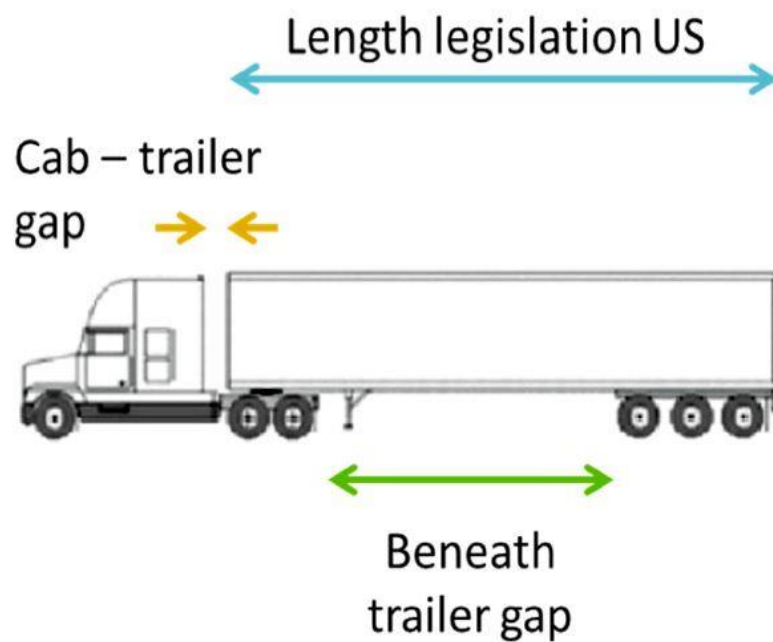
Figure 2.25: Example of truck with Cab behind engine (Hariram, et al., 2019)
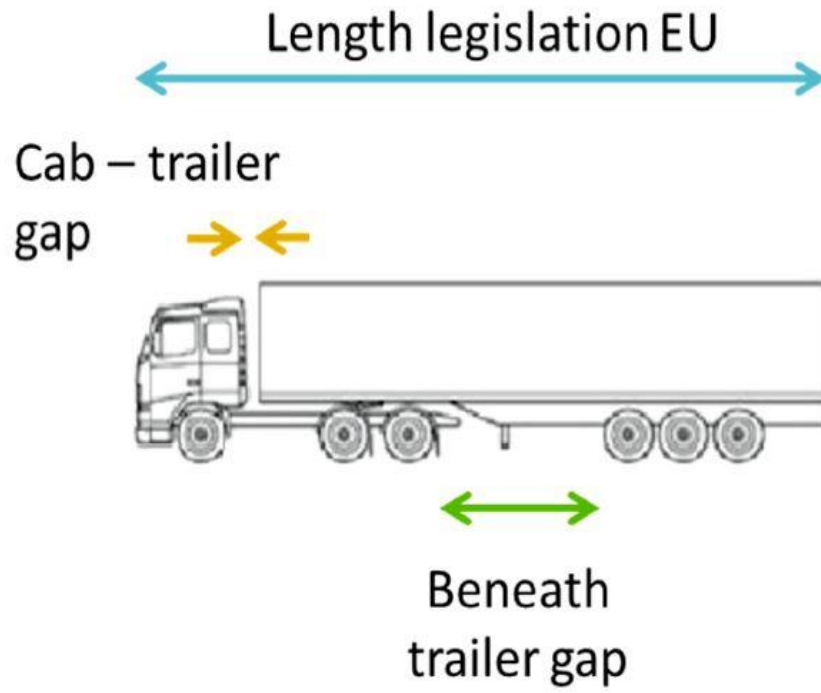
Figure 2.26: Example of truck with cab over engine (Hariram, et al., 2019).
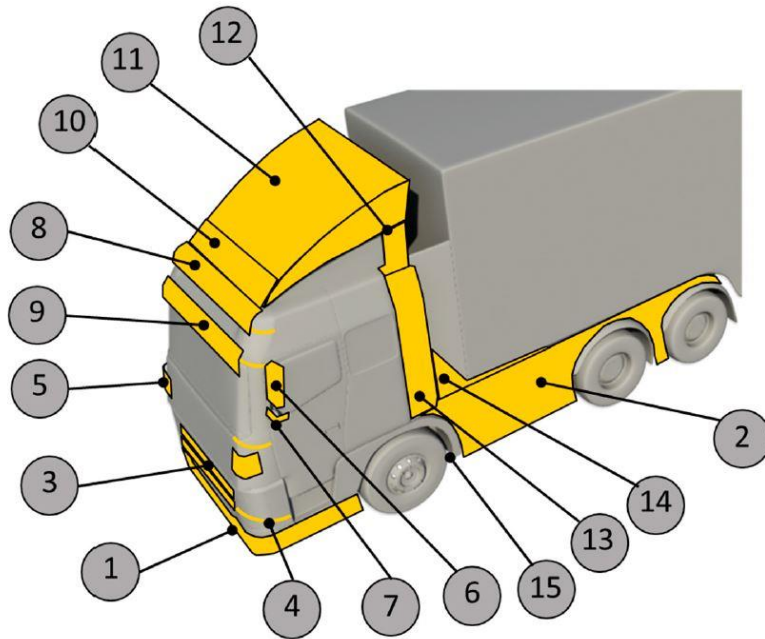
Figure 2.27: Locations of aerodynamic intervention around a tractor (Hariram, et al., 2019).

1.	Air Dam
2.	Tractor Side Panel
3.	Active Grill Shutter
4.	Cab side edge radius
5.	Cab side edge turning vanes
6.	Low drag mirrors
7.	Side View Cameras
8.	Cab roof Rim
9.	Cab sun visor
10.	Cab roof deflector
11.	Cab roof fairing
12.	Cab roof collar
13.	Cab side extenders
14.	Tractor chassis filler panels
15.	Smooth underbody.

Table 2.4: Notations used in fig 2.26.

In Figure 2.27, some of the major aerodynamic interventions carried out on a typical Cab over engine truck are shown. Some of these aerodynamic features have been explained in (SAE China, 2001) and (Freight best practise, 2007). A brief description of each of the aerodynamics intervention has been discussed in the numerical order.

1. An air dam is an extension on the bumper. This device is in the bottom half of a bumper and is responsible to guide airflow around that region. An air dam in most cases is integrated into the bumper itself (Iveco, 2008).

2. Tractor side panels cover a significant amount of area between the two axles. This area usually contains the two fuel tanks on either side with a drive shaft in the middle. The side panels in this area are responsible to reduce the turbulence which is caused by the tyres and fuel tank (Hjelm & Bergqvist, 2009).

3. Grill shutters are responsible to control the airflow which enters the engine for cooling purpose. The flow around an engine is highly dirty in nature and hence these shutters open and close when an engine requires extra cooling. They also serve an aerodynamic purpose by controlling the level of turbulent flow which could occur around an engine (Iveco, 2008).

4. Cab side edge radius is a tiny device which directs the airflow from the front of the truck to the sides. This device is responsible to control the airflow from becoming turbulent in the region (Bracco, et al., 2016).

5. Cab side edge turning vanes are responsible to control the airflow which separates from the leading edge of a cab. If a tractor does not have the correct radius to reduce flow separation, side edge turning vanes can be used to reduce flow separation (Hjelm & Bergqvist, 2009) (SAE China, 2001).

6. Low drag mirrors are a well rounded off structure which includes the arms and brackets to reduce the turbulence produced and also to direct the airflow (Hjelm & Bergqvist, 2009) (SAE China, 2001).

7. An alternative to low drag mirrors is the side view cameras. These cameras are mounted on the door and are much smaller in size. However, the overall shape of these cameras has to be optimized because the cameras could alter the flow around the entire truck itself.

8. A cab roof rim is a small rounded off edge which reduces the flow separation from the leading edge of the tractor (SAE China, 2001) (Hjelm & Bergqvist, 2009).

9. A sub visor is not considered in modern day trucks because they tend to increase drag. These devices were aerodynamic aids in the early days of trucks (Hjelm & Bergqvist, 2009) (SAE China, 2001).

10. The cab roof deflector is responsible to guide the flow on the upper edge of the trailer. It is also responsible to reduce the guide the flow without creating turbulence (Hjelm & Bergqvist, 2009) (SAE China, 2001).

11. The cab roof fairing is one of the ground-breaking aerodynamic aid ever invented for trucks. These are widely used devices which range from small trucks to road trains. they are rigid and contoured device mounted on the roof of the tractor and responsible to guide the airflow over the tractor and onto the trailer (Hucho, 1998).

12. The cab roof fairing and collar are extenders as part of the tractor which reduce the volume of air flow entering the gap. These devices also help in crosswind conditions (Hjelm & Bergqvist, 2009) (SAE China, 2001).

13. The side fairing is useful when the trailer is wider than the tractor. They guide the airflow to the width of the trailer which ultimately prevents the flow from impinging onto the front face of the trailer (Hjelm & Bergqvist, 2009).

14. The chassis filler panels are responsible to smooth the flow out around the bridge of a truck.

15. The underbody of a truck can generates a lot of turbulence due to the presence of axles, wheels, power train and few other members. Hence the underbody of a tractor can reduce drag by fitting with smooth underbody panels (Hariram, et al., 2019).

Jing-Peng et al (Peng, et al., 2018) carried out numerical research to understand the aerodynamic characteristics of cab design. The researcher aimed to modify the front end of a cab with two configuration of cab length as seen in Figure 2.28. The tractor has a protruding length. The angle of the A-pillar is kept at 70° which played a key factor in this research since this affects the aerodynamic characteristics of the vehicle (Fu, 2011). The numerical simulations gave a maximum of 8.49% reduction with the 500mm- 125° combination.
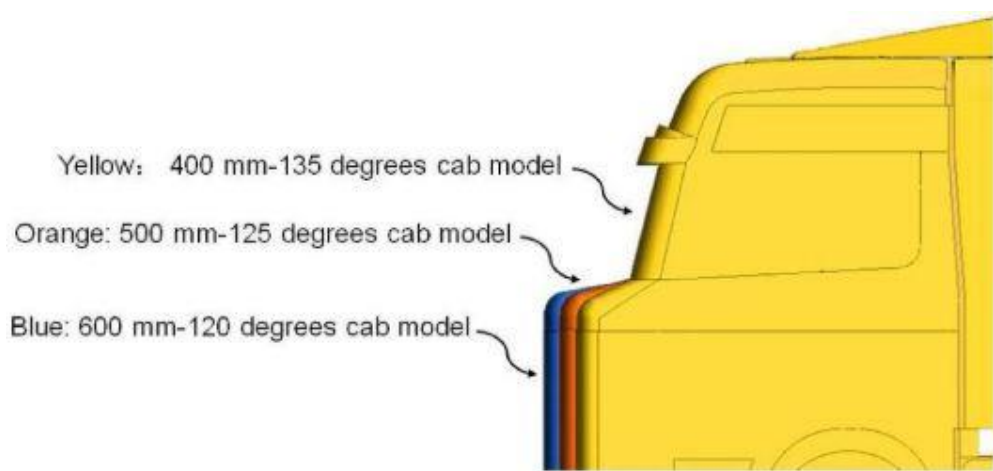
Figure 2.28:Cab designs (Peng, et al., 2018).

Figure 2.29 is an example of the most recent tractor from original equipment manufacturer (OEM). These tractors roll out of the factory with almost all the above-mentioned aerodynamic aids as seen in Table 2.4: Notations used in fig 2.26.. All the aerodynamic aids have been designed and optimised around the designated tractor to make the tractor aerodynamically efficient.

Content removed due to copyright reasons.

Figure 2.29:Example of a typical OEM tractor (Mercedes Benz, 2020)

2.8 Trailer Aerodynamics

The flow in the gap between the tractor and trailer is a significant feature which affects the drag coefficient of the truck ultimately leading to change in fuel consumption fuel consumption and driving stability of a truck. Numerous experimental and computational work have been carried out to predict and understand the flow field in the gap. Zheng et al (Zhiying, et al., 2010) in his work analysing the flow field around a 1:10 model found out the drag coefficient of the model was smallest at a tractor-trailer gap of 55mm. However, this work focuses only on one model, hence it can be said that the results are specific to the model. Yue Yang et al (Yang, et al., 2017) studied the flow field mechanism in the gap between tractor trailer model using Large Eddy Simulation. The study was mainly aimed at using different frontal area ratio for tractor. He concludes that the frontal area ratio between the tractor and trailer has a significant impact on the aerodynamics of the truck: the truck with a smaller frontal area for the tractor has a higher drag coefficient because of the mainstream flow impinging on the trailers front face. In order to reduce the drag coefficient, the author suggested the difference between the frontal area of the tractor and trailer should be close to low. Figure 2.31 shows the difference in drag coefficient between the three models numerically simulated with different tractor trailer gap ratios. The author also concludes that the increase in gap between the tractor and trailer enlarges the size of vortices present in the gap which lead to larger drag force whereas smaller gap creates a lot of flow separation at the top of the carriage to increase lift. Figure 2.30 shows the change in flow field around the test case with different tractor height and gap ratios. Hence, if the gap is either too big or too small, the flow field around a truck is highly turbulent. The optimal gap ratio between the tractor and trailer is different for different models considering numerous trucks of different shaped and sizes.
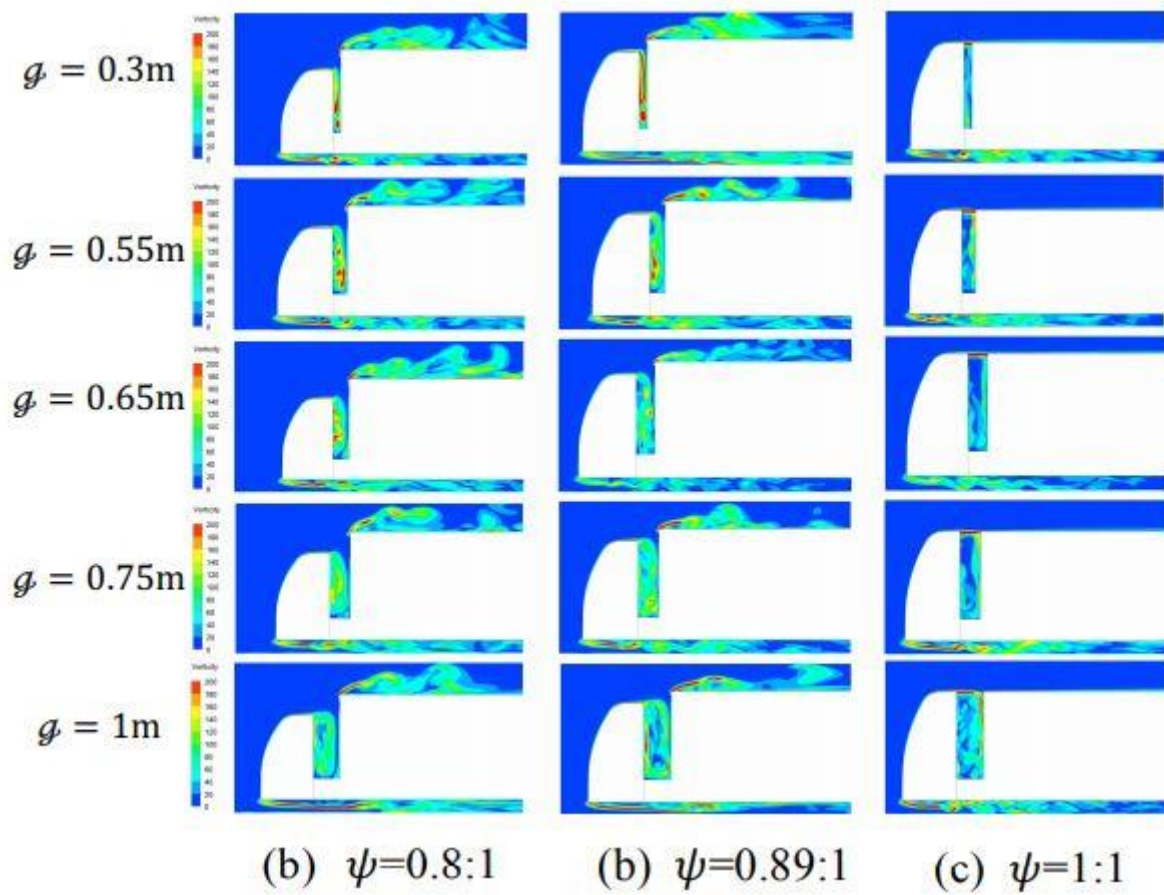
Figure 2.30:Vorticity contours on the XY plane (Yang, et al., 2017).
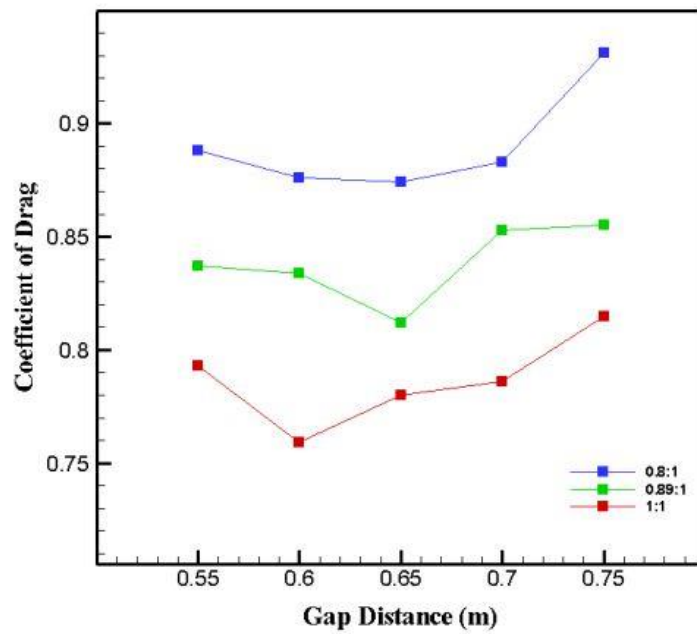
Figure 2.31:Cd with different gap widths (Yang, et al., 2017).

Flow control is an attempt to favourably alter the character and disposition of a flow field that is of concern (Hak, 2005). Humans first applied flow control to an arrow by using fin stabilizers. Several different similar empirical attempts had been practised on different devices. However, the science of flow control commenced in 1904 with the boundary layer theory and a scientific formulation for flow control was introduced by Prandtl (Minelli, 2017). It was in the late 1970's in the advent of the petroleum crisis, a boom to aerodynamic research was experienced and still continued to be performed on heavy vehicle (Cooper, 2002). The 20th century proved to be a push for major inventions and new theories formulated from different parts of the world. New methodologies were discovered to overcome challenges to new possibilities.

The challenge in today's world is to understand the flow behaviours, the physics behind the flow and ways to control the flow in order to reduce vehicle drag. In trucks, the challenge is more because of vehicle exceptional dimension and strict regulations etc. Trucks are designed to carry freight and stocks which require a boxy shaped trailer. This boxy shape is combined with a tractor which has the cab mounted over engine, making the truck least favourable in terms of aerodynamic body shape. Therefore, the main challenge is to keep the shape of the truck and to come up with effective design which is aerodynamically optimized to the already existing shape.

When looking at Figure 2.32, there are four main areas of interest around the trailer where aerodynamic interventions can be focused. The first of these areas is the roof of the trailer, the second in the front face/gap between the tractor and trailer, the third is the bottom part of the trailer where the spare wheels, tool boxes, run protection and few other elements would exist in a typical trailer and the last area is the wake region of the trailer. Table 2.5 shows the areas around a truck where aerodynamic interventions have been developed over the years in order to reduce the drag.
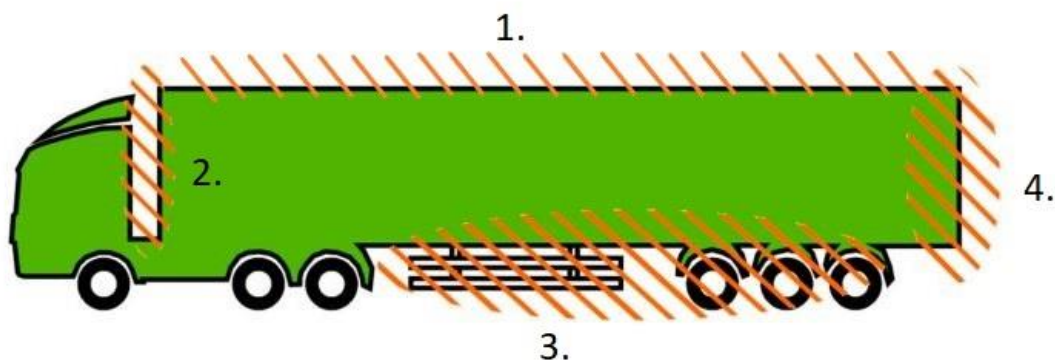
Figure 2.32: Critical area of drag generated around a trailer.

No.	Drag generating regions around a trailer.
1.	Roof of trailer.
2.	Gap between tractor and trailer.
3.	Under carriage of trailer.
4.	Rear end/wake region of trailer.

Table 2.5: Notation used in Figure 2.32.

2.7.1 Roof of Trailer

Most significant aerodynamic upgrade to the roof of the trailer is the tear drop shape. Figure 2.33 shows the wind tunnel illustration around a truck with a standard trailer and

Figure 2.34 shows the wind tunnel illustration around a truck with tear drop shaped trailer. Observing the top of the trailer in Figure 2.33, the flow in that region is highly turbulent when compared to the flow around the trailer in

Figure 2.34. The roof of this trailer is designed to improve the flow over the truck and reduce the base wake. This design does not increase the loading volume of the trailer itself but instead improves the flow field.

Content removed due to copyright reasons.

Figure 2.33: Standard 4.2m high trailer (Don Bur, 2016).

Content removed due to copyright reasons.

Figure 2.34: Tear drop shaped trailer (Don Bur, 2016).

2.7.2 Gap between Tractor and Trailer

A typical tractor-trailer consists of an air gap between the tractor and trailer in order to allow articulation when the vehicle is turning. The Figure 2.35 depicts the schematics of flow pattern in the gap. As it can be seen the gap allows high velocity flow to impinge on the front face of the trailer resulting in an aerodynamic drag. This inward turning flow impinges onto the front face of the trailer resulting in a high pressure. The high pressure on the front face directly causes and increases the drag of trailer which ultimately contributes towards an increase in the overall drag coefficient of the whole truck. Crosswind can also have a detrimental effect when the flow enters the gap due to the flow separation which occur on the leeward side of the trailer resulting in high side force which can hinder vehicle handling (Wood, 2006).
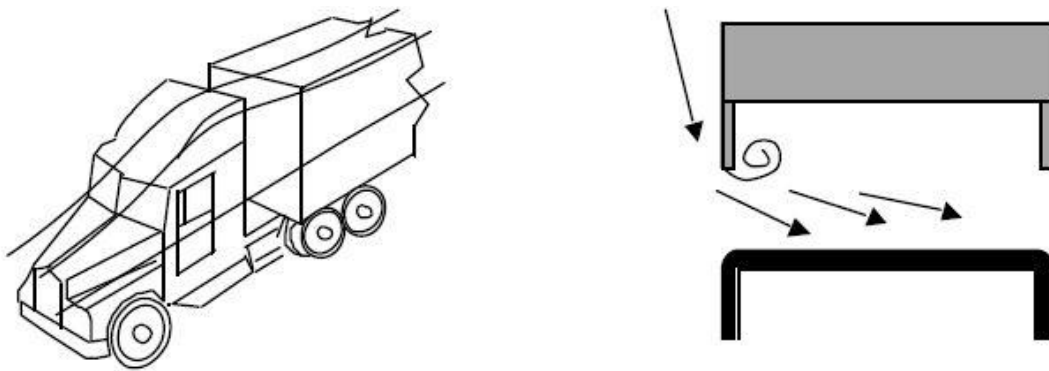
Figure 2.35: Schematic depicting the flow field in the gap for a typical tractor – trailer (Wood, 2006).
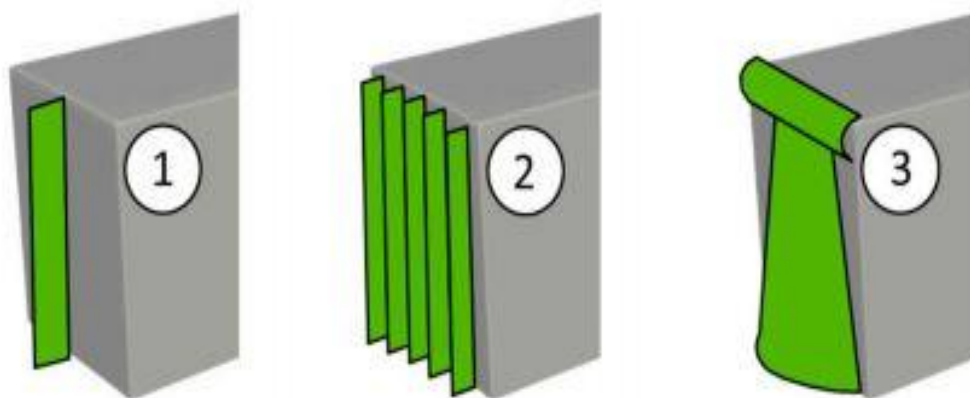
Figure 2.36: 1. Splitter plate, 2. Vortex trap device and 3. Air cone (Hariram, et al., 2019).

Richard (Wood, 2006)discussed gap treatment using a simple fixed device which was tested out after reviewing the concepts with fleet owners. The concept was of minimal maintenance, good safety, low weight, cost effective and aerodynamic loads. He came up with an idea of two vortex flow devices for operational testing as shown in Figure 2.35. These two devices were cross vortex trap device and vortex strake device. However, only cross vortex trap device was used in the gap between the tractor and trailer. This device followed the principle based on trapped vortex technology.

Figure 2.36 shows some of the modification to improve the flow field in the gap between the tractor and trailer ultimately reducing drag. The splitter plate and vortex trap device are devices which are meagrely used on trucks. The splitter plate is responsible to split the fluid flow along the vertical height of the trailer's front face. In cross wind conditions the splitter plate extends to blocks any form of cross flow occurring in the gap. A vortex stabiliser is a device like the splitter plate. This device consists of vertical slats on the front face of the trailer. The number of slats varies with the width of the truck. These slats are usually equally spaced. The vortex stabiliser is an improved form of the splitter plate in terms of function. They are highly effective in cross wind condition. A vortex trap device is located on the front face of a trailer. The device works by capturing the inward turning flow which enters the gap between the tractor and trailer. The captured crossflow then separates at the leading edge of each CVTD and generates a vortex that is trapped between adjacent CVTD's as seen in Figure 2.37a. The device is responsible to impart low and a more even pressure distribution on the front face of the trailer. The local velocity of the trapped vortices within adjacent slabs is greater than the velocity of the surrounding flow thereby producing low pressure on the front face of the trailer. The pressure on the adjacent slabs is high, however the forces are perpendicular to vehicle axis. This does not contribute to aerodynamic drag. The forces acting on adjacent slabs are equal and opposite of each other and hence they do not contribute to vehicle side forces either. Air cones are responsible to act as guides to the air flow which is immediately around the tractor. Depending on the function of the device, it can close the gap and reduce the turbulence cause during cross wind conditions without forming any big vortices. Figure 2.37b and Figure 2.38 show the flow trapping mechanism achieved using CVTD.
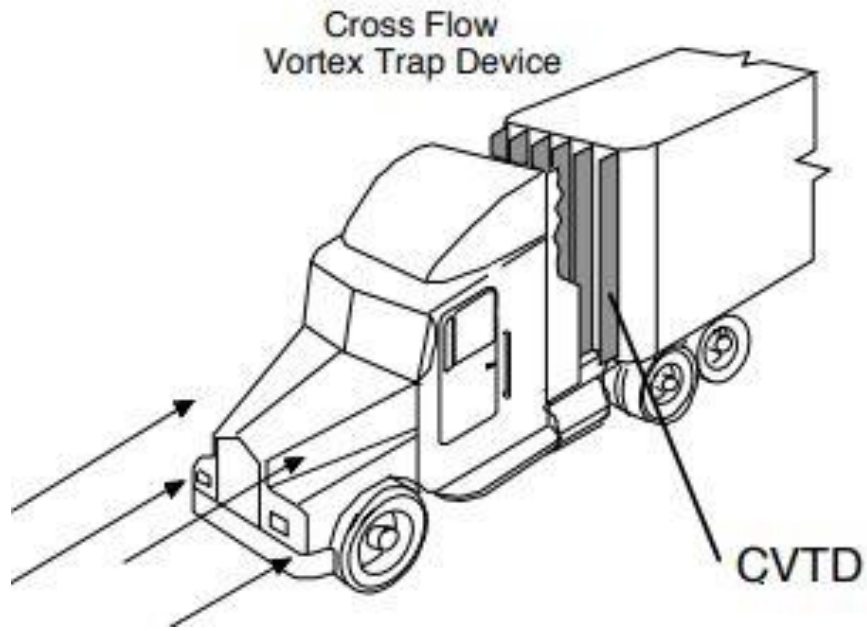
(a)
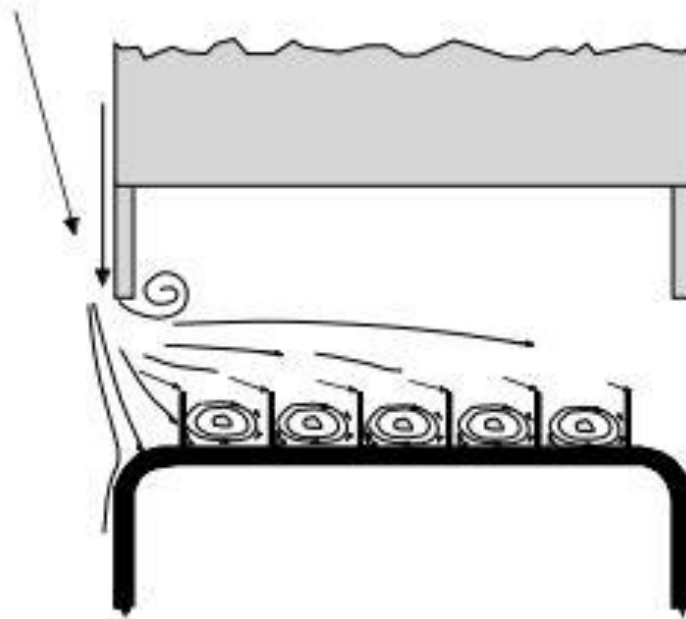
(b)

Figure 2.37:(a) Truck with CVTD installed on the front face of the trailer (b) Flow mechanism in the gap region using CVTD.
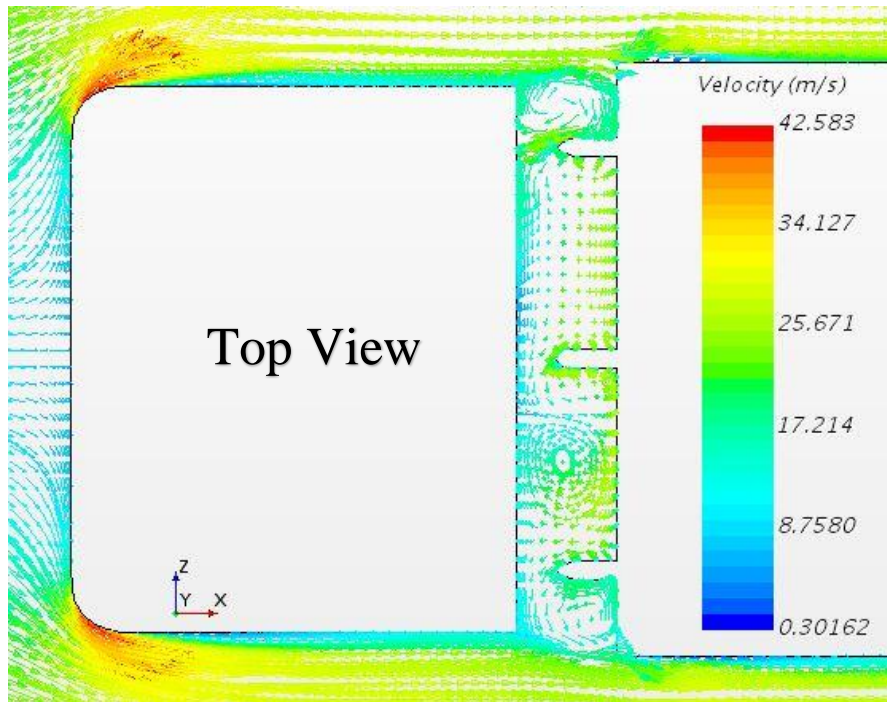
Figure 2.38: Velocity contour displayed on the XZ plane (Charles, et al., 2019).

A fence shaped device (Figure 2.39) was trialled by author (Ni & Qi, 2011) mounted on front face of the rear body above the cab. The devices were numerically and experimentally simulated on a generic low duty truck model. The device is mounted onto the truck as seen in Figure 2.40. The overall drag of the model was reduced by nearly 22%. However, this device has proved to produce fluctuating drag coefficient at different gap width between the cab and the body work itself. The author highlights the need to optimise the device with change in gap ratios. The height and length of the fence must change with change in gap ratios D. With increase in the size of the device, the aerodynamic drag of the truck increases and then decreases. A minimum drag coefficient also exists which the author highlights is important for drag reduction for trucks. The device requires the best position and size to achieve drag reduction and improve the flow field.
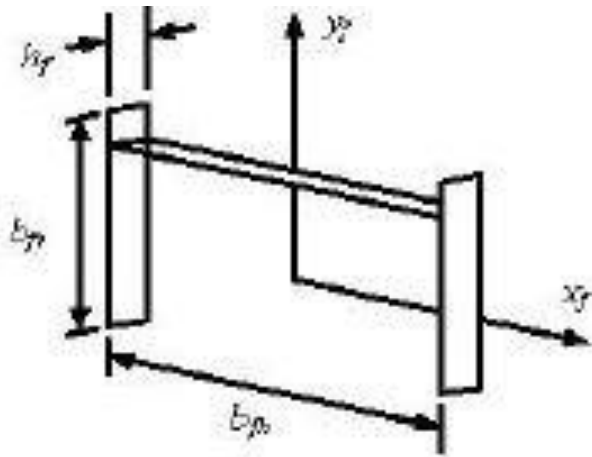
Figure 2.39:Sketch of fence shaped device (Ni & Qi, 2011).
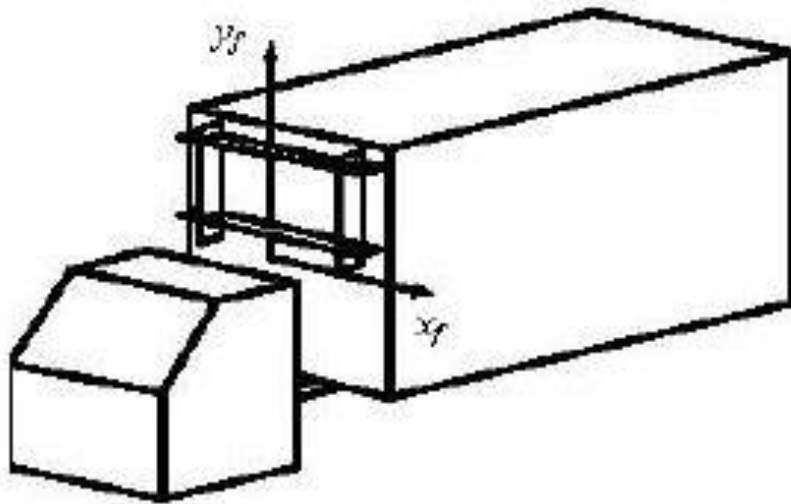
Figure 2.40:Device mounted onto truck test case (Ni & Qi, 2011).
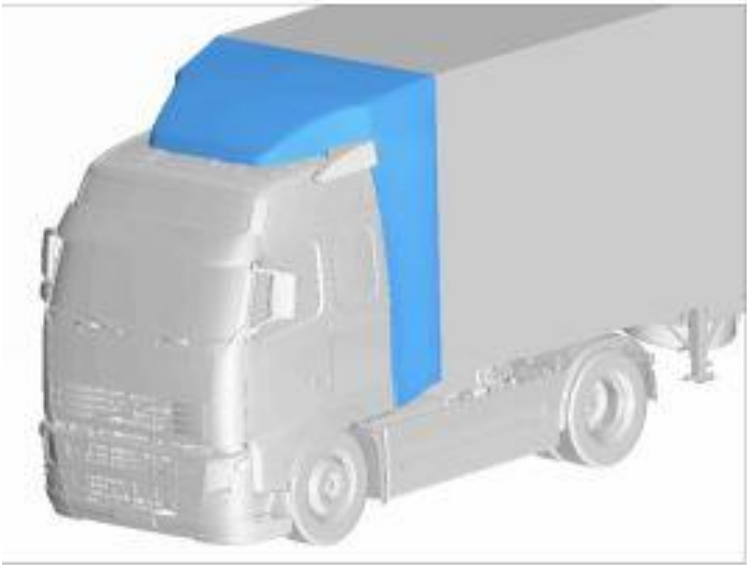
(a)
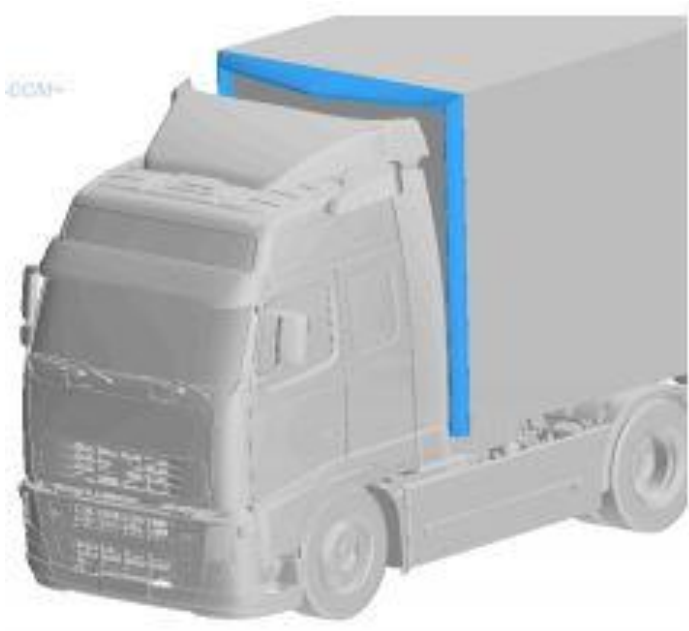
(b)

Figure 2.41: Examples of two types of gap treatment (a)Sealed gap and (b)gap Fairing (Hakkansson & Lenngren, 2010).

In Figure 2.41a, this device seals the airgap between the tractor and trailer. This may seem like an ideal solution, but it does not consist of any realistic usage and consider the trucks turning ability. Figure 2.41b shows a picture of gap fairing. This type of device effectively improves the reattachment of the flow from the tractor to the trailers leading edges. The device can effectively reduce the high-pressure peaks which appear on the edges of the front face of the trailer (Hakkansson & Lenngren, 2010). Figure 2.42 shows the flow around a truck using gap fairing. Observing the gap, a smoother flow is visible over the gap resulting in an improved attachment that reduces the size of the bubble at the top of the trailer.
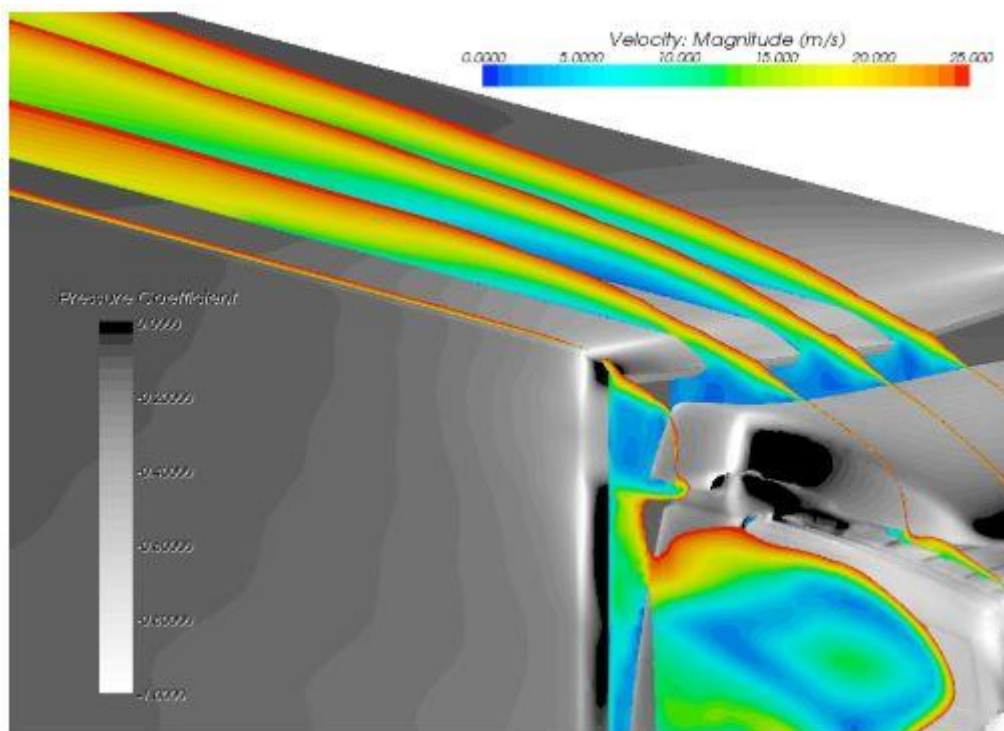
Figure 2.42: Velocity contours on different y-planes (Hakkansson & Lenngren, 2010).

V.Malviya et al (Malviya, et al., 2009) investigated a passive drag reduction technique with cab roof fairing and moving surface boundary layer control (MSBC). The MSBC device is a rotating cylinder which is mounted to the leading edge of the trailer. The cylinder is attached to motors which are responsible to drive the cylinder. The system modifies the flow field by changing the boundary layer separation. The flow field changes by the additional kinetic energy to the air flow next to the surface of the trailer. This technique also reduces pressure from the front face of the trailer. The flow field can be viewed on the XY plane in Figure 2.43b. From Figure 2.43, observing the leading edge of the trailer, a reduction in flow separation can be visualised with the use of this device. However, this technique results in compromising a small portion in the total volume of the trailer and uses motors to drive the MSBC device itself. The device is classified under active aerodynamic devices due to the rotating nature of the cylinder mounted on the trailer as seen in Figure 2.43a. Several techniques have been applied over the last few years to reduce aerodynamic drag by delaying boundary layer separation.

| (a) | (b) |
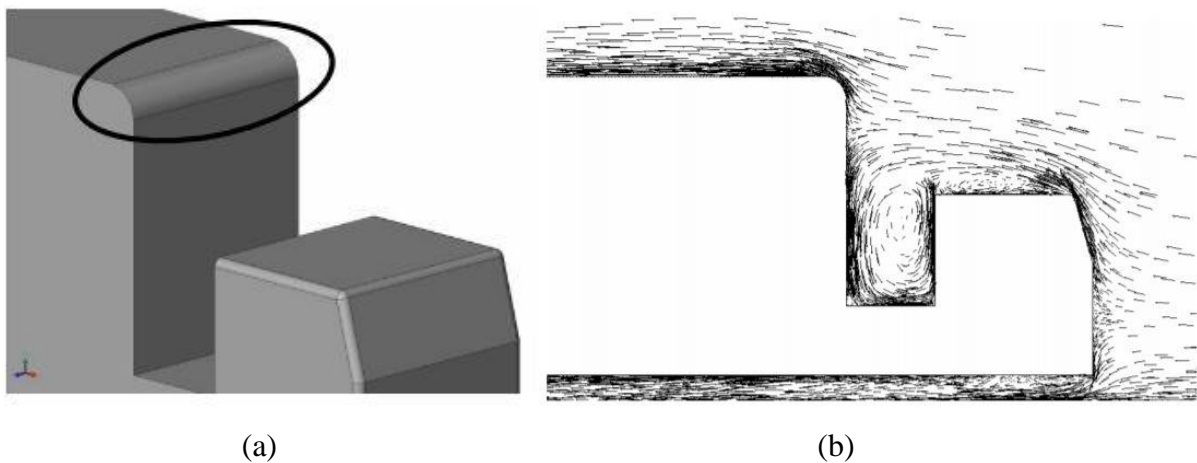
Figure 2.43: (a) Pictorial representation of location of MSBC device, (b) Flow field viewed on the XY symmetry plane using the MSBC device (Malviya, et al., 2009).

2.7.3 Under Carriage of Trailer
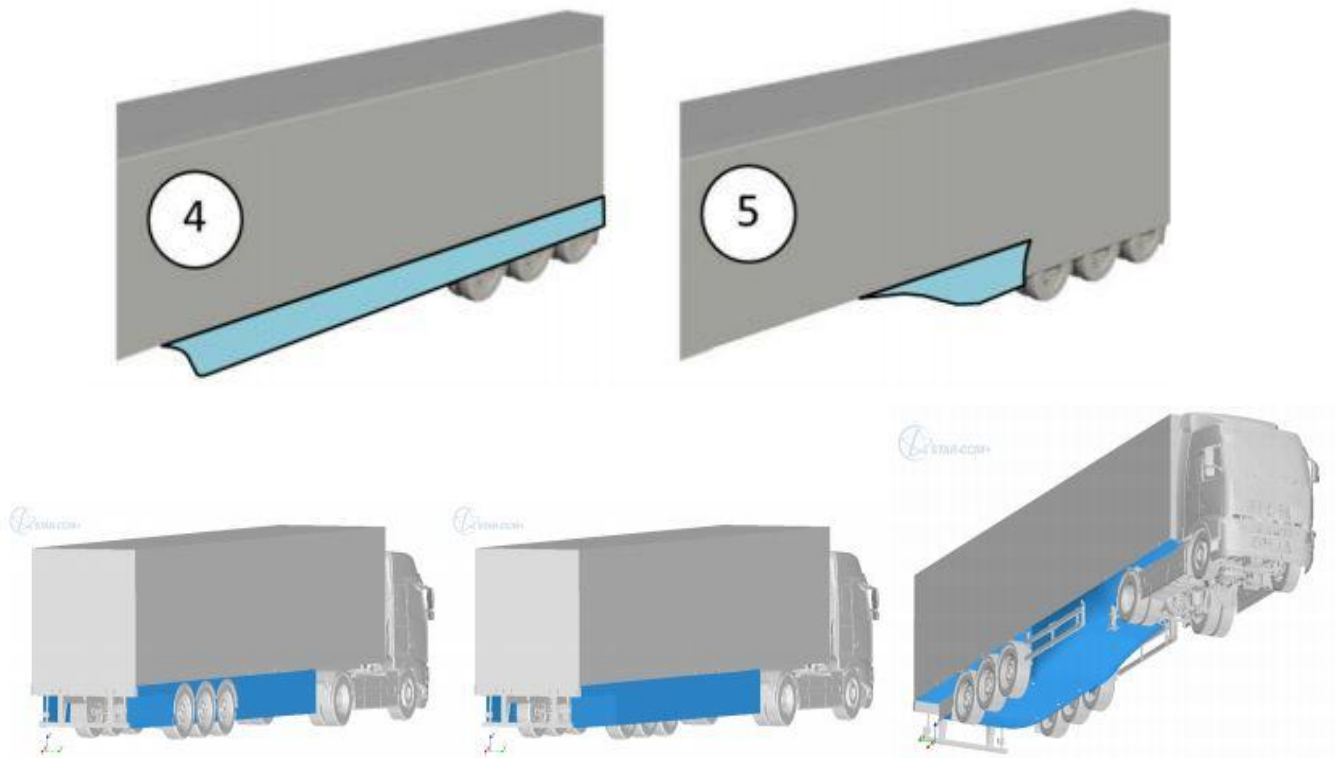
Figure 2.44: Some examples of under carriage treatment used by truck operators (Hariram, et al., 2019) (Hakkansson & Lenngren, 2010).

Under carriage of a truck is a widely investigated region for the truck itself. This is because the flow in the under carriage of a truck is highly turbulent due to the presence of spare tyre, toolboxes, axles, guard rails etc. The flow in this region is not smooth so that the region contributes nearly 25% drag of the truck. The under-carriage devices can be of different configurations like side skirts, sealed wheels and a smooth underbody. All these devices tend to smoothen the flow in the under-carriage region resulting in reduction of turbulent nature of the flow (Hakkansson & Lenngren, 2010). Several trailer skirt shapes have been evaluated over the years in the past, with the most recent being the DOE heavy truck consortium (Mccallen, et al., 2004) and National Research Council Canada (Cooper & Leuschen, 2005). Side skirts are common practise to be added to trailers. Figure 2.44shows some under-carriage treatment which have been used in commercial trucks. Truck Manufacturers association (Truck Manufactueres Association, 2007) wind tunnel experimented on several aerodynamic devices with different shapes for a realistic full-scale truck.

The experiments were investigated on three different categories based on the following:

1. Various Skirt types.
2. Skirt height and trailer height impact.
3. Belly box.

The experiments were carried out with different shape and size. Each of the above design categories had three different shapes and fitted to the undercarriage of the trailer as seen in Figure 2.45 and Figure 2.46. The data given in Figure 2.47 are compared between percentage of drag coefficient to ground clearance (h/d). The results showed that the closer the skirt is to the ground, the higher the drag reduction for the truck. The experiments predicted a total of 8-11% drag reduction for straight side skirt (h/d = 0.07). straight skirts also achieved nearly 3-4% drag reduction than a U or V-shaped skirt at a similar ground clearance ratio. The belly boxes proved to have a comparable drag reduction to the straight skirts with similar ground clearance ratio.

Content removed due to copyright reasons.

Figure 2.45: Three configurations of side skirt shapes tested in the wind tunnel (Truck Manufactueres Association, 2007).

Content removed due to copyright reasons.

Figure 2.46: Belly Box (Truck Manufactueres Association, 2007).

Content removed due to copyright reasons.

Figure 2.47:Percentage drag reduction using Side skirts and belly box with different ground clearance (Truck Manufactueres Association, 2007).

2.7.4 Rear End of Trailer

Rear end of a trailer is another widely researched area due to the complexity of flow fields which exists in the wake of a truck. The trailer can create certain amount of wake flow due to its considerably large cross section. Some of the examples of rear end aerodynamic designs are given in the Figure 2.48, Figure 2.49 & Figure 2.50. Figure 2.48 shows the tapered trailer design. In this the rear end geometry of the trailer is tapered on either side to improve the airflow and reduce flow separation which ultimately reduces aerodynamic drag. However, this design in fact results in reduction in the actual volume of the trailer (Hakkansson & Lenngren, 2010).

Tomas et al (Skrucany, et al., 2016) investigated undercarriage treatment and rear end tapering using a generic 1/24 scaled wind tunnel truck model. The complete model is mounted inside a wind tunnel shown in Figure 2.49. Figure 2.50 shows the rear end treatment experimented in the research. The author measured the influence of each device has on the air flow around the model in terms of drag count (%). The measurements were carried out at 0° and 5° yaw angle. Figure 2.51 shows the improvement each device has made in terms of percentage for the model. The author concludes that the model with static wheels and roads will have very minimal difference to those models of rotating wheels and a moving road.
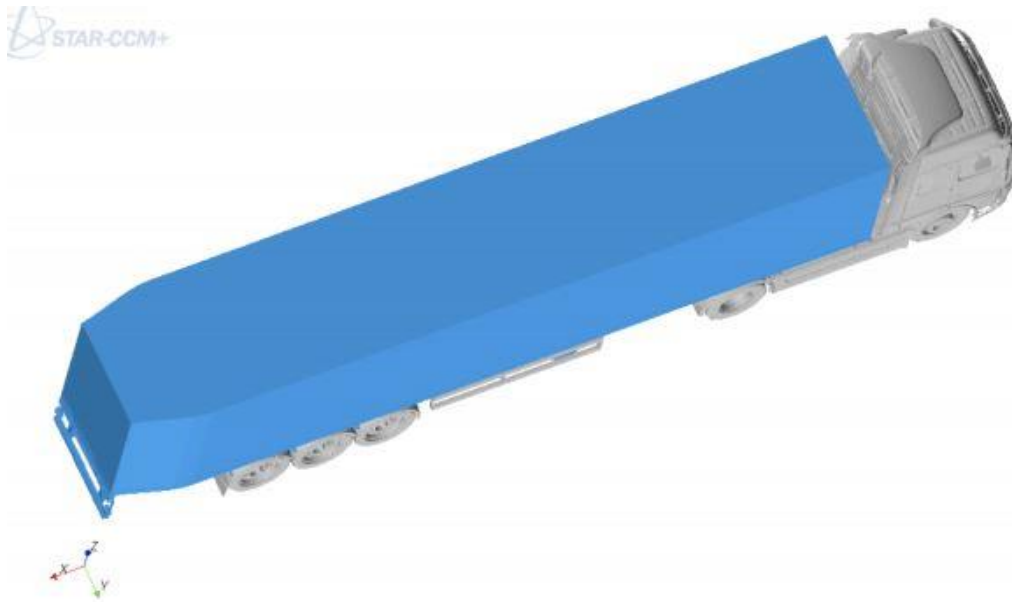
Figure 2.48: Tapered rear end of trailer (Hakkansson & Lenngren, 2010).

Content removed due to copyright reasons.

Figure 2.49: Wind tunnel model with sealed wheels (Skrucany, et al., 2016).

Content removed due to copyright reasons.

Figure 2.50:Rear end modifications on a trailer (Skrucany, et al., 2016).

Content removed due to copyright reasons.

Figure 2.51:Drag reduction for the test case in terms of percentage. (Skrucany, et al., 2016)

Chilbule et al (Chilbule, et al., 2014) carried out profile modification on a simplified tractor-trailer model. The author primarily focussed on aerodynamic modifications like roof deflectors, vortex trap devices, under carriage device and frame extension with aerodynamic revolute. A pictorial representation of a generic truck and modified truck is shown in Figure 2.52. The authors compared the results obtained for generic and modified model using static pressure contours, turbulent kinetic energy contours, velocity streamlines velocity contours and swirling vortices. Figure 2.52(a & b) presented the comparison of the total kinetic energy between the generic test case and test case with boat tail. The wake region of the trailer shows the peak pressure of the recirculation region is considerably reduced. A total of 21% drag reduction was achieved on the modified truck model which equates to a reduction from 23kN to 18.14kN. This would lead to a total of 4.2 litres reduction in fuel consumption for every 100 km for a truck cruising at 30m/s.
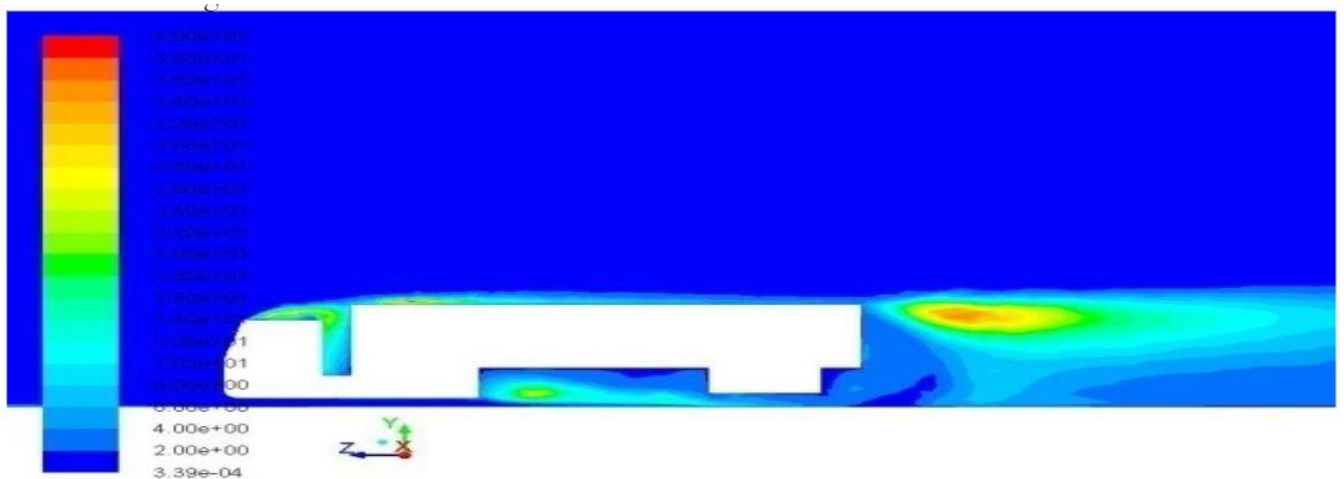
(a)
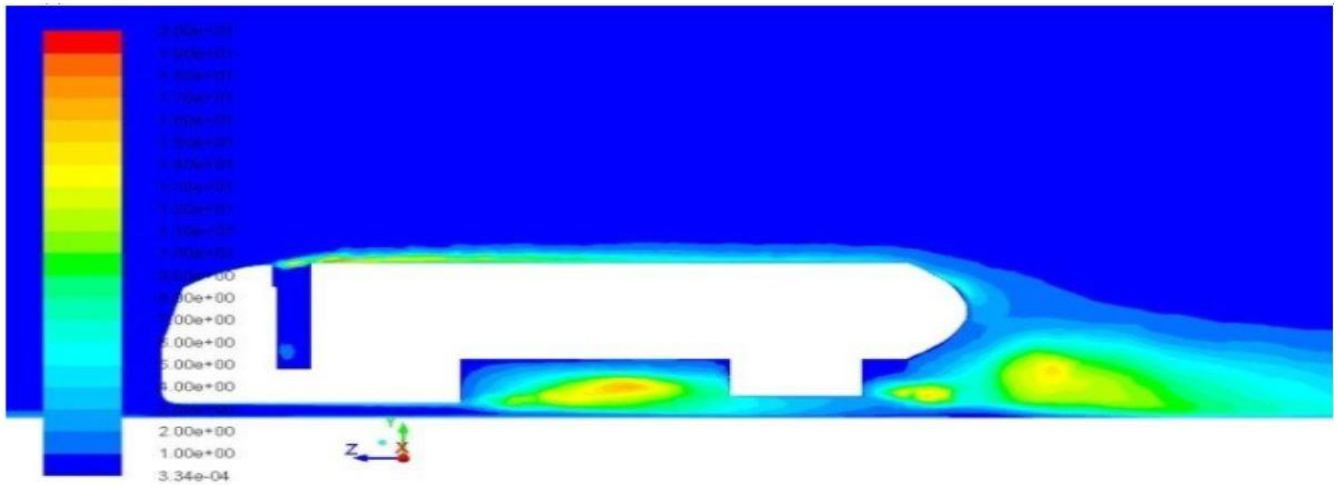
(b)

Figure 2.52:Turbulent Kinetic energy viewed on the XY symmetry plane (a) Generic Truck, (b) Modified truck with boat tail (Chilbule, et al., 2014).
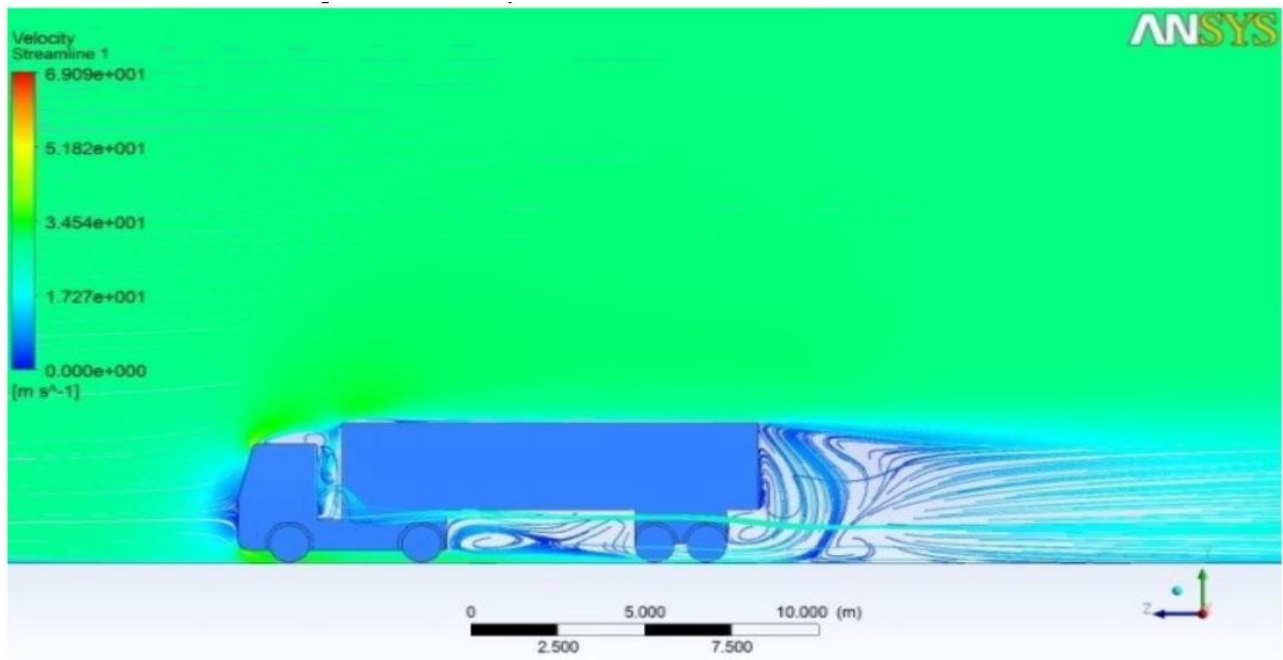
(a)
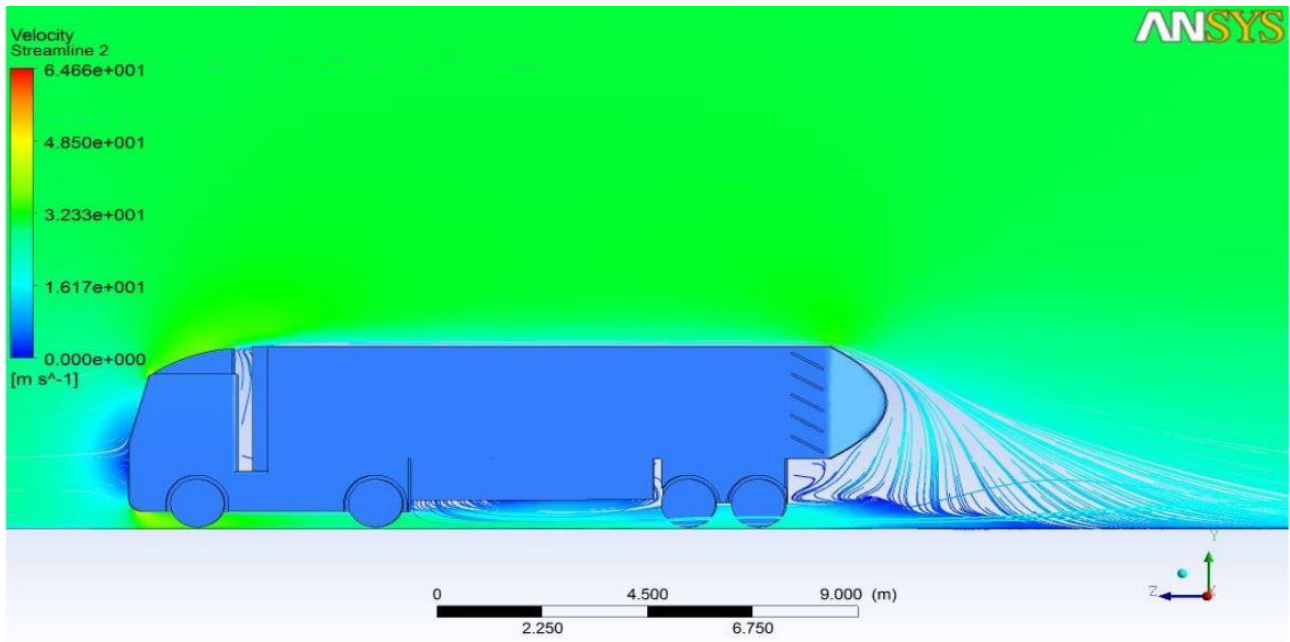
(b)

Figure 2.53:Velocity streamline viewed on the XY symmetry plane (a) Generic test case; (b) Modified test case (Chilbule, et al., 2014).

In Figure 2.53 (a & b) velocity streamlines are viewed on the y-symmetry plane for a generic test case and a modified test. The streamlines give a clear picture of the flow around the truck. The significant improvement in flow field can be seen in the gap between the tractor and trailer, under carriage of trailer and the rear end of trailer. The streamlines around the basic truck are not as smooth as the modified truck, which proves that the level of turbulence around the truck has been considerable reduced for the modified truck.

2.9 Flow Field in the Gap between Tractor and Trailer

In general, the wider the gap the less aerodynamic the truck becomes which directly increases the aerodynamic drag. There exists a critical gap which varies depending on the geometry of the truck. This critical gap tends to be the gap at which the truck reaches the maximum drag which can be seen in Figure 2.54. Hence, beyond this gap the tractor and trailer become essentially decoupled. Wind tunnel experiments have been used to identify the relationship which exists between the tractor-trailer gap and vehicle drag. At a critical gap, the relationship is given by:

$$\frac{G_{critical}}{\sqrt{A}} = 0.5$$

Here in the equation A is the cross-sectional area which is normal to the longitudinal flow and G is the gap between the tractor and trailer. At the critical gap there exists a major jump in drag coefficient. This is mainly due to a major part of the flow impinging onto the trailer (Hammache & Browand, 2004). The shape and design of tractor trailer have drastically improved over the years from a flat front end to a more aerodynamic shape.
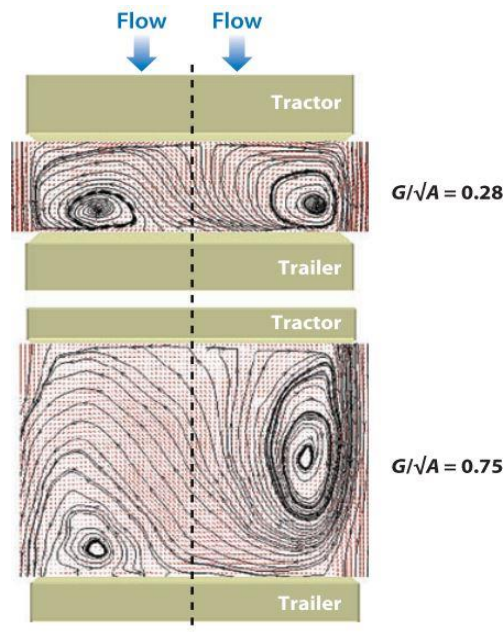
Figure 2.54:Time averaged flow structures in the gap at two different gap ratios for the Ground Transport System model (Hammache & Browand, 2004).

Drag can only be reduced around a truck by controlling the flow around the vehicle. This section gives an insight into the flow field within the gap and around it at different gap ratios. A number of experimental and computational studies have been carried out to examine this flow field in the gap (Castelucci & Salari, 2005) (Hammache & Browand, 2004) (Osth & Krajnovic, 2012). Hammache and Browand (Hammache & Browand, 2004) in their work showed that the flow field in the gap vary vastly depending on the gap width and their resulting influence on drag coefficient is significant. Figure 2.55 gives a graphical representation of change in drag coefficient to gap width. Gap width is given as a ratio of gap length and square root of frontal area. At $\frac{G}{\sqrt{A}} < 0.5$, the drag coefficient of the trailer shows a plateau. In this regime the flow field in the gap is symmetric and counter rotating vortices. The author also mentioned that the flow in the gap is also close to steady state flow resulting in a low-pressure region at the front face of the trailer and hence lower drag coefficient. At lower gaps i.e. $\frac{G}{\sqrt{A}} < 0.1$, the pressure inside the gap increases which increases the ultimately increases the base pressure on the tractor resulting in further drag reduction. With the reduction in base pressure for the tractor, the trailer experiences a higher pressure on its front face. However this close gap width of $\frac{G}{\sqrt{A}} < 0.1$ is not practically possible due to the working behaviour of an articulated truck. The gap is too close for the truck to articulate. At critical gap widths i.e. $0.5 < \frac{G}{\sqrt{A}} > 0.6$, the flow symmetry in the gap breaks down. The flow is characterised by unsteady nature from the trailing edge of the tractor. This kind of flow feature increases the drag coefficient of the trailer and is carried over up to a gap width of $\frac{G}{\sqrt{A}} \sim 0.8$ and then the curve linear as seen in Figure 2.55. Trucks without any add on devices or shape modifications, the point of flow separation is from the trailing edge of the trailer body. There is also a large wake region which also have a significant pressure drop.
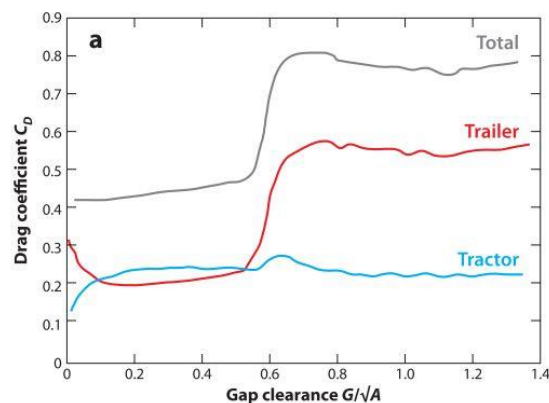
Figure 2.55: Drag coefficient data compared with tract-trailer gap width for the Ground Transport System model (Hammache & Browand, 2004).

2.10 Simplified Test Case

The results from several models have been discussed in the earlier part of the thesis. There are several different simplified test cases available beyond the above discussed models. It is important to select a geometry which is appropriate to this research being conducted. The test case considered here have been specifically chosen to understand the flow field in the gap between the tractor and trailer. The test case aims at achieving representative vehicle flow field. In this section the procedure of this project is described. The test cases are modelled and computed using commercial software Star CCM+. The study was performed using steady state numerical simulations which is good enough to predict the large-scale turbulent feature of the flow.

2.10.1 Test Case Models

The Ahmed model is the most used test case across the automotive industry. The Ahmed model is used to study drag reduction with several backlight angles (Vino, et al., 2005). The model has a flat front face with curved out leading edges. The leading edges are curved out at 50mm radius to reduce the flow separation. The Ahmed model has a standard dimension as seen in Figure 2.56a, however the model has several adaptations used so far where the total length of the model is reduced or the radius of curvature on the leading edges are reduced (Cooper, 1985). The above Ahmed model was developed as a reference model for cars.

The Windsor model was developed in the 1980's. The model was created by Windsor and Howell to represent a car. The model was used to carry out parametric studies on geometry modifications focussing mainly on the slant angle. This model has the same length as the Ahmed body but with a long slant angle at the front and a relatively short, flat roof section. This means that the flow around the fore body is far more closely linked to the wake structure and hence it is an important representation of the vehicle. A schematic of the Windsor model can be seen in Figure 2.56b.

Content removed due to copyright reasons.

(a)   (b)

Figure 2.56:Dimensions of simplified models. (a) Ahmed model and (b) Windsor model (Perry, 2016) (Good & Garry, 2004).

Few other simple test cases include the David model developed at the Imperial College as shown in Figure 2.57, the docton model developed at the Durham University in 1996 shown in Figure 2.58. The David test case is frequently used for cross wind investigation, both in steady and transient flow conditions along with changes to geometry such as backlight angle. The Docton test case is mainly used to perform transient simulations.

Content removed due to copyright reasons.

Figure 2.57:Schematic of the Davis model (Good & Garry, 2004).

Content removed due to copyright reasons.

Figure 2.58:Docton model (Good & Garry, 2004).

All these above models have been used as a generic test case to understand the flow field around a car or a truck on several papers. Geometrically a tractor and trailer consist of two rectangular bodies which work together in a tandem arrangement. The flow around these tandem bodies consists of several stagnation point, gap flow, underbody flow and huge wake region. All these tend to create drag for the vehicle (Buil & Herrer, 2009) (Cooper, 2002) (Wood, 2006). The Ahmed model is the most popular model which is widely used till date for various numerical and experimental purposes. After many years of research work using experimental and computational methods, the Heavy Vehicle Aerodynamic Drag Consortium came up with two simplified versions of a tractor trailer model, The Ground Transport System model and the Generic Conventional model.

2.10.2 The GTS Test Case

The Ground Transport System model (Croll, et al., 1996) consists of two bluff bodies which are geometrically simplified without any extra features. This model has been extensively researched in the automotive industry (Storms, et al., 2001) (Rao & Minelli, 2018) (Srinivas, et al., 2006). The model has been used as a test case for experimenting and numerically simulating truck and bus like models with a wide range of add-on devices on them (Croll, et al., 1996) (Castelucci & Salari, 2005). The GTS model consists of two individual bluff bodies separated by a gap, kept in tandem arrangement. The front body represents the tractor and rear body represents the trailer. The model was developed as part of a multiyear research project by Heavy Vehicle Aerodynamic Drag Consortium (Ross & Mahta, 2006). The objective of developing this model was to obtain a clear understanding of the flow phenomenon responsible for aerodynamic drag around a truck (Choi, et al., 2013). The GTS model does not consist of any under carriage in order to simplify the test case. When observing the pictorial representation in Figure 2.59 the length of the tractor is considerably long when compared to trucks in Europe with curved edges. The flow field around such tractors remain more attached making it less drag and more aerodynamic. However, the GTS model is more focussed for trucks in America based on shape and size. The trucks in the United states have freedom to play around with the overall length of the truck itself, however only the length of the trailer must be regulated. Hence most of the trucks in the united states have varying gap lengths.
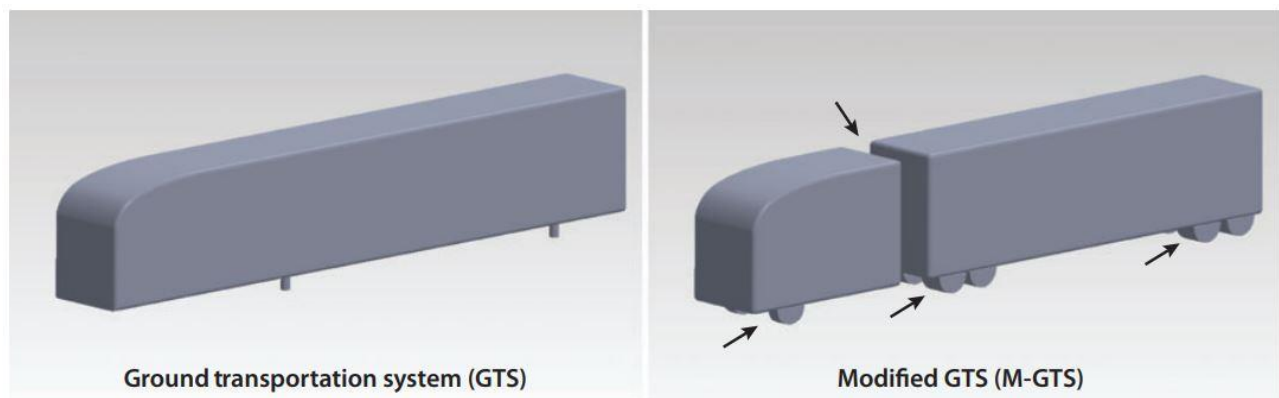
Figure 2.59: A pictorial representation of a generic GTS and a modified GTS model in tractor trailer arrangement (Choi, et al., 2013).

2.10.3 The GCM Model

The GCM model is in contrast to the GTS model. The test case has lot more realistic features in terms of tractor trailer gap along with a streamlined tractor shape as seen in Figure 2.60. The test case does not consist of an undercarriage for the tractor and trailer i.e a flat and smooth floor is applied. The research was further carried out by adding modifications to the GCM model as seen in Figure 2.60. An example of the wheel housing used by R Pankajakshan et al (Pankajakshan, et al., 2007) in his numerical simulation is given in Figure 2.61. The GCM test case is a good example of a Cab behind Engine tractor.
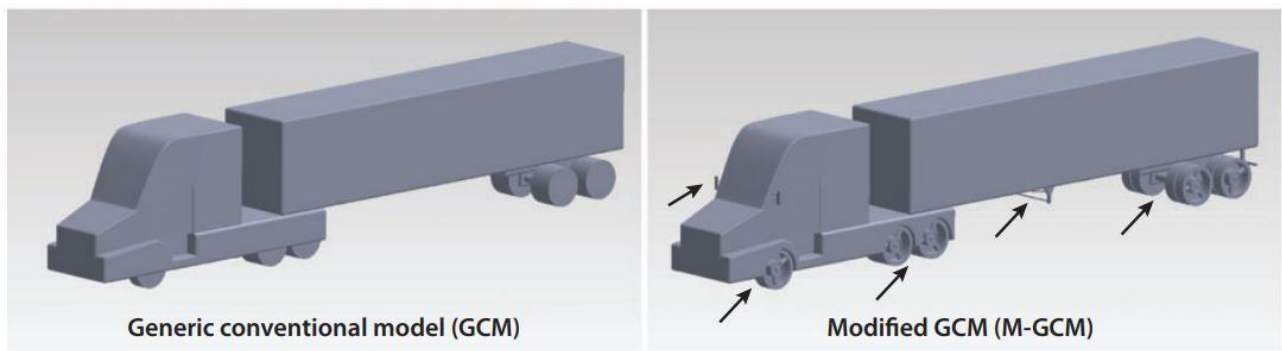
Figure 2.60: Pictorial representation of generic GCM model and a modified GCM model (Choi, et al., 2013)
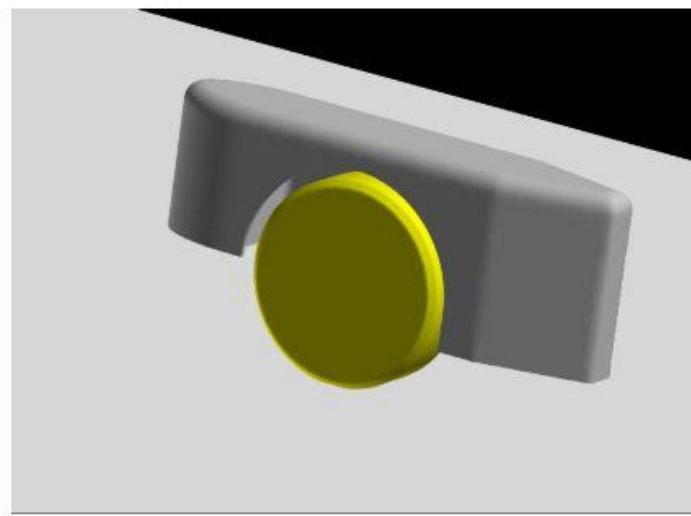
Figure 2.61: Wheel housing which was used in the numerical simulation (Pankajakshan, et al., 2007).

2.10.4 Simplified Tractor-Trailer Model

The test case considered for this research is shown in Figure 2.62. The simplified tractor-trailer model is a better representative model for the trucks which operate on European roads when compared to the previous models presented above. The test case was first experimentally simulated by Allan (Allan, 1981). The dimensions shown in Figure 2.62 are a ratio as proportion of the height of the rear box (trailer) b=0.305m. Both the tractor and trailer have a square cross section. The model used in this research in the test case with rounded leading edges for the tractor. The vertical and horizontal leading edges of the tractor are rounded to a non-dimensional value of 0.08b which is the same from the from the experiments conducted by Alan (Allan, 1981). The tractor and trailer are connected together by a cylinder which has a radius of 0.04b. The cylinders are places horizontally and attached to the back face of the tractor and front face of the trailer.
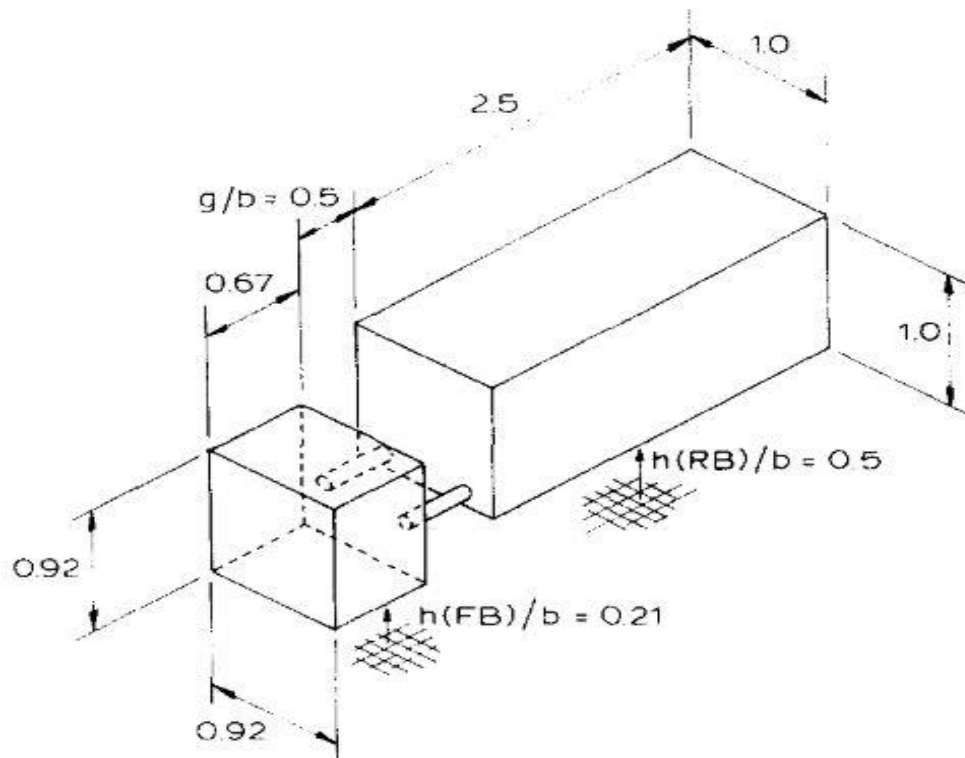
Figure 2.62:Schematic of test case considered for this research (Allan, 1981).

Chapter 3

Methodology

3.1 Introduction

Computational fluid dynamics (CFD) has become a widely used tool for both designing and analysing flow. Flow solution can be obtained which were not analytically available. This has made CFD a primary tool in the industry. Even though CFD has gained a huge importance in the past decade, experimental research still remains the pinnacle of ultimate test.

CFD uses computers to numerically simulate a flow around and inside a model in almost any scenario. Specifically, in this case, it is used for automotive aerodynamics. In solving Navier-stokes equations, if pressure and velocity are known at every point within the domain including the surface, then the forces on the body can be obtained. CFD has become a powerful tool used by aerodynamicist which reduce time and cost to develop an aerodynamically efficient products.

Turbulence modelling is the most challenging problem in the CFD. The semi-empirical models are usually required to calculate these unknown correlations. Most practical applications of CFD requires three key elements: (Celik, 1999)

1. Grid Generation.
2. Algorithm Developments.
3. Turbulence modelling.

In the above three elements, the first two elements consist of precise mathematical theories. However, the theory behind turbulence modelling is far less precise due to the complex natures of a turbulent flow. A turbulent flow in CFD could be time dependent and three dimensional. This has been assisted by an increase in the computational resources over the past decade making this tool a vital platform in terms of cutting costs. The data which can be generated by computational methods for any kind of fluid flow problem give a huge advantage for CFD over experimental approach. Some of the important advantages of CFD is the reduction in time required for numerically simulating a particular problem.

3.2 Turbulence Modelling

There are two different kinds of flows: Laminar flow and turbulent flow. The turbulent flow consists of numerous eddies which cascade in a complex manner within a flow. Almost every engineering problem consists of turbulent flow which consists of strong mixing within the flow itself.

The Navier-Stokes equation is the heart of any CFD problem. The equation can be used to predict fluid flow around an element. Due to a high Reynolds number of interests, the turbulent motion can be fully resolved with a grid of sizeable to resolve the smallest turbulent length scales which requires the Kolmogorov scale. Even for approximate estimates, a simple problem would require around 10^{20} to solve all the turbulent scales at a Reynolds number of 10^{6}. In order to capture every possible detail of turbulence, the simulation should resolve time dependant 3D behaviour in the Kolmogorov scale. This approach would be considered as the Direct Numerical Simulation (DNS). The DNS approach requires a very fine mesh to capture every scale which is present in a given flow. Hence the DNS approach is an expensive approach and is advisable only to simple geometries.

The next approach would be the Reynolds Averaged Navier Stokes (RANS) method which is quicker in terms of solving the problem and can be used to numerically simulate flow around complicated geometries. This is a widely used approach in the industry to simulate turbulent flow since it is cost effective. However, this approach sometimes fails to capture some small turbulent features accurately.

The third approach is the Large Eddy Simulation (LES) which lies in between the DNS and RANS approach. The LES approach has gained popularity lately within the automotive and aerospace industries. The LES approach computes large eddies while modelling the smaller eddies. LES approach uses spatial filtering to distinguish between the larger and smaller eddies. The larger scales are resolved directly, and smaller scales sub grid scales tend are homogenous in nature are approximated. The equations for this approach are obtained from spatial filtering. This approach is cheaper than DNS approach but still far expensive the RANS method.

3.3 Reynolds Average Navier-Stokes Equation

Considering turbulent flows, several different fields such as pressure, velocity and density vary randomly with time. Reynolds averaging approach separated the flow quantities into stationary and random parts. The instantaneous quantities are then presented in the form of sum of the mean flow value and fluctuating counterpart.

$$\emptyset = \bar{\emptyset} + \emptyset'$$ 3.1

In equation 3.1 the quantity $\bar{\emptyset}$ is the mean part of the quantity and $\emptyset'$ fluctuating part of the quantity.
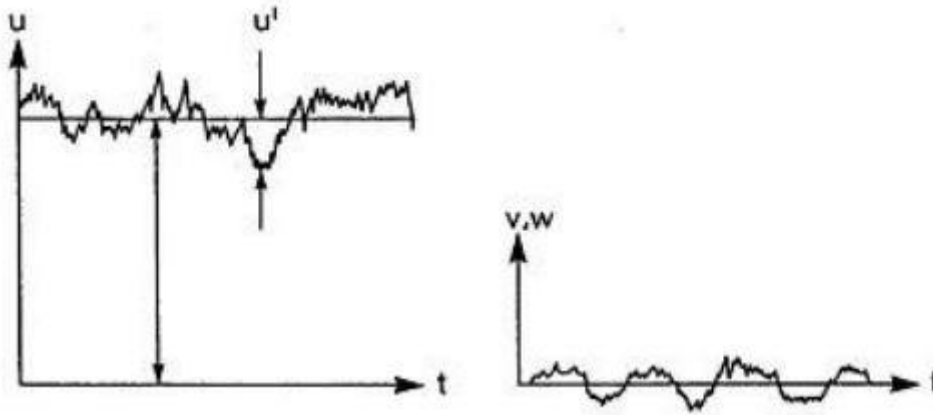
Figure 3.1: Turbulent velocity fluctuation in pipe flow with respect to function of time (Yang, 2020).

The above formulation and conservation equations are inserted together. This process is known as Reynolds averaging. Time averaging is the one of the most common averaging method used in CFD industry. The flow field are predicted in mean values. To time average, the monetary values are decomposed into several parts of mean values and fluctuating values as shown in the Figure 3.1. The time averaging variable can be defined as:

$$\bar{\varphi} = \frac{1}{t_a} \int_{t}^{t+t_a} \varphi \, dt$$ *3.2*

In Figure 3.1, momentary velocity component is u and it is denoted as $\bar{u}$ in the time averaged notation. The fluctuating velocity is denoted as u'. This will help in defining the decomposition equation in the mathematical form as follows:

$$u = \bar{u} + u'$$
$$v = \bar{v} + v'$$
$$w = \bar{w} + w'$$
$$p = \bar{p} + p'$$
3.3

Considering incompressible flow, Reynolds decomposition is applied to the continuity equation as follows:

$$\frac{\partial}{dx_j} u_j = 0 \qquad\qquad 3.4$$

$$\frac{\partial \bar{u}_j}{dx_j} + \frac{\partial u'}{dx_j} = 0 \qquad\qquad 3.5$$

Averaging both the terms,

$$\overline{\frac{\partial \bar{u}_j}{dx_j}} + \overline{\frac{\partial u'_j}{dx_j}} = 0 \qquad\qquad 3.6$$

Since the term $\bar{\bar{u}}' = 0$, the above equation becomes,

$$\frac{\partial \bar{u}_j}{\partial x_j} = 0 \qquad\qquad 3.7$$

Applying decomposition as shown in the above equations to the Navier-Stokes equation:

$$\rho \left(\frac{\partial \bar{u}_i}{\partial t} + \bar{u}_j \frac{\partial \bar{u}_i}{\partial x_j} \right) = -\frac{\partial \bar{p}}{\partial x_i} + \frac{\partial}{\partial x_j}\left(\mu \frac{\partial \bar{u}_i}{\partial x_j} \right) + \frac{\partial}{\partial x_j}(-\rho \overline{u'_i u'_j}) \qquad 3.8$$

The decomposed Navier-Stokes equation has the original terms replaced with the instantaneous terms. In the above equation the term $\rho \overline{u'_i u'_j}$ is the Reynolds stress tensor. The stress tensor is an unknown which consists of six independent components. The Reynolds stress tensor also consists of the pressure component along with three velocity components which complete the closure problem. The closure problem has more unknown quantities. In order to simplify the closure problem, we introduce the Boussinesq hypothesis. The hypothesis can be called as an eddy viscosity model which in RANS includes zero equation model, one equation model or two equation model. A brief description of the Boussinesq hypothesis and the three models are given below.

3.4 Boussinesq Model

The Boussinesq hypothesis is based on an analogy between viscous and Reynolds stresses. The Boussinesq model describes the Reynold stresses as a product of velocity gradient and eddy viscosity (μ_t). The model is expressed as below:

$$-\overline{\rho\mu_i'\mu_j'} = \mu_t\left[\left(\frac{\partial u_i}{\partial x_j} + \frac{\partial u_j}{\partial x_i}\right) - \frac{2}{3}\delta_{ij}\frac{\partial u_k}{\partial x_k}\right] - \frac{2}{3}\rho\delta_{ij}k \qquad 3.9$$

The primary idea of the hypothesis is that Reynold stresses can be calculated as a product of strain rate tensor of the mean flow and dynamic eddy viscosity.

$$-\overline{\rho\mu_i'\mu_j'} = 2\mu_t S_{ij} - \frac{2}{3}\delta_{ij}k \qquad 3.10$$

Here S_{ij} can further be written as:

$$S_{ij} = \frac{1}{2}\left(\frac{\partial u_i}{\partial x_j} + \frac{\partial u_j}{\partial x_i} - \frac{2}{3}\delta_{ij}\frac{\partial u_k}{\partial x_k}\right) \qquad 3.11$$

Here the eddy viscosity μ_t is a scalar quantity and Reynold, stresses are linearly proportional to the main strain rate tensor. In order to compute eddy viscosity μ_t further calculations are required. In order to further model μ_t, turbulence model is required. Turbulence models are categorised based on the number of transport equations each model uses to calculate μ_t. Hence depending on the number of transport equations and the turbulence models used, the Boussinesq hypothesis classifies the following:

1. **Algebraic or zero equation model:** Baldwin-Lomax (Baldwin & Lomax, 1978) model.
2. **One equation model:** Spalart Allmaras (Spalart & Allmaras, 1992) model
3. **Two equation models:** models such as $k - \varepsilon$ (Launder, 1972), $k - \omega$ (Wilcox, 1988).

3.5 Algebraic or Zero Equation Model

The algebraic of the zero equation turbulence models do not require solution of equations and calculate directly from the flow variables. Hence, the zero-equation model may not be able to calculate the effects of turbulence, such as convections and diffusion terms of the turbulent energy. These models are very simples to be used for a general CFD problem. However, they can be used to simulate a simple flow or to initiate a flow situation (E.g. At the initial phase of a complicated flow simulation) (Baldwin & Lomax, 1978).

3.6 One Equation Model

The one equation model was developed to improve the ability of the algebraic model in order to account for the convection and diffusion of turbulence. This was achieved by using a transport equation. This gave the realisation of the kinetic energy of turbulence, k. A general form of the transport equation can be written in the following form:

$$\frac{\partial k}{\partial t} + \mu_j \frac{\partial k}{\partial x_j} = \tau_{ij} \frac{\partial u_i}{\partial x_j} - \varepsilon + \frac{\partial}{\partial x_j}\left[\frac{\mu}{\rho}\frac{\partial k}{\partial x_j} - \frac{1}{2}\overline{u_i'u_i'u_j'} - \frac{1}{\rho}\overline{p'u_j'}\right] \qquad 3.12$$

The term $\tau_{ij}\frac{\partial u_i}{\partial x_j}$ represents the turbulence production in the equation. Considering the terms within square brackets, the first one $\frac{\mu}{\rho}\frac{\partial k}{\partial x_j}$ is the molecular diffusion, the second term $\overline{u_i'u_i'u_j'}$ is the turbulent flux within the turbulent kinetic energy and the third term $\frac{1}{\rho}\overline{p'u_j'}$ is the pressure diffusion. The third term is usually neglected due to small contribution. The two terms $\boldsymbol{\varepsilon}$ and k are the dissipation rate per unit mass of fluid. Hence $\boldsymbol{\varepsilon}$ can be defined as

$$\varepsilon = \overline{\frac{\mu}{\rho}\frac{\partial u_i'}{\partial x_k}\frac{\partial u_i'}{\partial x_k}} \qquad 3.13$$

The one equation Spalart-Almaras model is the most common one equation model in use today. Turbulent kinetic energy profile is better accounted for in the one equation model due to the addition differential equation. This equation comes in handy for non-equilibrium flows and therefore provides better results than algebraic models. Spalart-Almaras model are specifically useful for fluid flow with adverse pressure gradients and transonic flow conditions where the mean velocity gradients are zero. Improved prediction of the near wall effects and the transition can be integrated into the model's equation by adding an extra term because of their modular design. Hence for these reasons the one equation model was popular among the aerospace industry. However, the disadvantage of this model is that the length scale, l, cannot be computed. This could improve the prediction of high turbulent flows which have a wider range of length scales, making it difficult to predict.

3.7 Two- Equation Model

3.7.1 $k - \varepsilon$ Model

The two-equation model is by far the widely used turbulence model. The two equation are highly reliable and complete set of equations i.e. the turbulence model can predict properties of a given flow without any prior knowledge of the turbulence flow structure or flow geometry. The two-equation model consists of two different sets of transport equations which calculate turbulent kinetic energy, k, and turbulent length scale, l, or a function of the turbulent length scale. Several proposals for the choice of the 2nd arbitrary variable was considered. Some of the popular ones used in the CFD industry are given below.

1. τ – Turbulent time scale.
2. ε – Dissipation rate of turbulence.
3. $\omega - k$ – specific dissipation rate

One of the most widely used turbulence model is the $k - \varepsilon$ turbulence model. One of the initial version of the $k - \varepsilon$ turbulence model was developed by Jones and Lauder (Jones & Launder, 1972). In this model, turbulent scale is calculated using the second transport equation for the turbulent dissipation rate, ε. The eddy viscosity is derived using the below equation.

$$\mu_t = C_\mu \rho \frac{k^2}{\varepsilon} \qquad\qquad 3.14$$

Here C_μ is the model coefficient. The $k - \varepsilon$ model is the able to predict attached flow which consists of thin shear layers and jets. However, this model fails to satisfactorily predict correct flow behaviour in the presence of adverse pressure gradients, separated flow regions, swirl motion in the flow and curvature generated secondary flows.

An advanced version of the $k - \varepsilon$ model is a Realizable $k - \varepsilon$ model. One of the initial Realizable $k - \varepsilon$ was formulated by Shih et al (Shih, et al., 1995). The realizable model contains a new transport equation for the turbulent dissipation rate. The critical model coefficient C_μ is not considered to be a constant and instead it is a function of mean flow and turbulent properties. This allows the model to meet with certain mathematical constraints on the normal stresses consistent with the physics of turbulence. With the variable C_μ, it remained consistent with experimental observation along the boundary layers (Star CCM+, 2020). The other difference is a new transport equation for the dissipation rate ε which is derived from the same equation for the transport of the

mean square vorticity fluctuation. As a results, this gives a superior ability to capture the flow of complex structures including flow involving rotational boundary layers under a strong adverse pressure gradients (Seyyedvalilu, 2018). This model is considered to be more accurate and is more reliable and accurate to give data (Star CCM+, 2020).

3.7.2 Realizable $k - \varepsilon$ Model

The realizable k-epsilon model has an improved version of the transport equations for the turbulent dissipation rate. This means the critical coefficient of the model C_μ is expressed as a mean flow function and the turbulent properties instead being assumed as a constant in the standard k-epsilon model. The realizable model allows to satisfy certain mathematical constraints of the normal stress which are consistent with the physics of turbulence. The model coefficients C_μ are also consistent with experimental observations in boundary layers.

The realizable model has proven to be better than the standard k-epsilon model for many practical applications and can be relied upon to give results which are closer to experimental results. The realizable k-epsilon can be used as a two-layer approach which will enable solving both low and high y^+ wall treatment. A detailed explanation of wall treatment is given in the next section.

3.7.3 $k - \omega$ Model

The $k - \omega$ turbulence model is a solver which follows the similar policy as the $k - \varepsilon$ of using two equation to solve the transport equations for the turbulent kinetic energy and the dissipation rate ω i.e. the dissipation per unit turbulent kinetic energy determines the turbulent eddy viscosity. The advantage with the $k - \omega$ model is the improved prediction for boundary layers adverse pressure gradients. However, a more significant advantage is that it can be applied throughout the boundary layer which includes viscous dominated region without any modifications.

3.7.4 Shear Stress Transport $k - \omega$ Model

The $k - \omega$ turbulence model began as a linear $k - \omega$ two equation model. Wilcox (Wilcox, 1988) in 1988 presented the linear $k - \omega$ model. However, the most notable changes to the $k - \omega$ model was proposed by Menter (Menter, 1994) who introduced the hybridisation method. He blended $k - \omega$ and $k - \varepsilon$ equations and further described the parameters to compute low Reynold number flow properties. Combining the two equations of $k - \varepsilon$ and $k - \omega$ model coefficients for α, β, σ_k^{-1} and σ_ω^{-1} (notations) given in the equation below (Spentzos, 2005).

Type of Model $(k - \omega)$	σ_k	σ_ω	S_1
Wilcox (Wilcox, 1988)	2	2	0
Menter (SST) (Menter, 1994)	$\dfrac{1}{B\binom{0.85}{1.0}}$	$\dfrac{1}{B\binom{0.5}{0.856}}$	$B\left(\dfrac{0}{\dfrac{1.71}{\omega}\nabla k.\nabla w}\right)$

Table 3.1:Values for constants used in linear k-w model (Spentzos, 2005).

Blending function is defined by

$$F_1 = \tanh\left(arg_1^4\right) \qquad 3.15$$

In equation 3.16 τ is an auxiliary variable and can be expressed by:

$$arg_1 = \min\left[\max\left(\frac{k^{\frac{1}{2}}}{\beta * \omega y}, \frac{500v}{y_n^2 \omega}\right), \frac{2k\omega}{y_n^2 \max(\nabla k.\nabla\omega, 0.0)}\right] \qquad 3.16$$

In the SST $k - \omega$ turbulence model, an issue with sensitivity to the inlet free streaming conditions was addressed by Menter (Menter, 1994). The author modified the ε in the transport equation of the standard $k - \varepsilon$ model and transformed it to an ω transport equation. This new equation looks like the standard $k - \omega$ model but with an extra non-conservative cross diffusion term containing

the dot product of $\Delta k \cdot \Delta \omega$. Including the term in the transport equation helps the $k - \omega$ model give identical results to the $k - \varepsilon$ model. The author (Menter, 1994) further blended the equation with a function of wall distance which could include cross diffusion far from walls instead of near wall. This approach uses the $k - \varepsilon$ model in the near wall and the $k - \omega$ model away from the wall. With the introduction to linear constitutive equation, the model containing the above modifications was named SST (Shear Stress Turbulence) $k - \omega$ model. The SST model gives an additional vorticity based on the shear stress. Hence the second blending function is written as:

$$F_2 = \tanh(arg_2^2), \qquad\qquad 3.17$$

$$arg_2 = \max\left(\frac{2k^{\frac{1}{2}}}{\beta * \omega y}, \frac{500v}{y^2 \omega}\right) \qquad\qquad 3.18$$

For computations which involve lower Reynolds number, the $k - \omega$ model and Menters baseline $k - \omega$ and SST model have the following boundary conditions which are assumed as a direct integration to the wall itself.

Hence,

$$\text{For k: } k_\omega = 0, flux(k)_w = 0 \qquad\qquad 3.19$$

$$\text{For ω: } \omega = \infty, flux(w)_w = -v\nabla w \qquad\qquad 3.20$$

In the above equations the subscript w denoted the value at the wall.

There exists a linear relation between Reynold stresses and the mean strain rate which tends to strongly underpredict the anisotropy of turbulence. Turbulence tends to be anisotropic in most of the complex flows. Some of the examples of complex flows are shear layer or boundary layer flows, strong swirls and streamline curvature. This anisotropy not only affect the fields but also the turbulent transport of scalars (Temperature, concentration, passive scalar) (Star CCM+, 2020).

3.8 Grid

The initial phase of a computational analysis is to decompose the large physical system into smaller sub-domains. This is known as spatial discretisation. In CFD, the fluid domain or the volume is broken down into small elements (cells or meshes) in which the solution for fluid flow and variables are determined. The interaction of these small elements gives a clearer picture of a complex problem. The cell or mesh is an element which consists of discrete number of points overlaying the domain and geometry (Jiyuan, et al., 2018).

Mesh generation is one of the most important steps in CFD during the pre-process stage. Mesh generation is a critical numerical step. A specific mesh for a given fluid flow problem can determine whether the computational solution is right or wrong. Principally the mesh should be fine enough to provide geometrical accuracy and capture the tiniest of flow features but also not be too refined to waste computational time and resources. For simulations to capture vorticity and steep flow gradients it is important to refine the mesh locally and clustering the mesh towards the boundary wall. Local mesh refinement is also important for flows consisting of shear layers or temperature gradients. The quality of mesh also determines the convergence and stability of the numerical simulation along with its accuracy of results. A detailed grid generation technique is explained in the next few paragraphs.

During mesh generation – the subdivision of a domain into smaller regions, several smaller mesh or cells are thereby generated. Hence the mesh must be generated in such a way that it adequately resolves the important physics and captures the geometrical details of the domain within the flow region. Generating a fine and optimized mesh is no mean trivial. Grid generation in the CFD industry has become an individual topic by itself and remains a very challenging area in research and development (Jiyuan, et al., 2018).

When considering mesh, there are currently two different types of mesh generating techniques: Structured and Unstructured. A structured grid is the simplest method used in grid generation. The structured grid has a defined number of grid lines, defined using coordinate surfaces, distributed in each coordinate direction, well defined cell to cell connectivity. An unstructured grid on the other hand does not have any restrictions on the grid lines. This is because the connectivity is defined locally by involving only reference to each neighbouring cell. A structured grid is made up of hexahedral elements. However, an unstructured grid is made up of a combination of elements like tetrahedral, prisms, hexahedral's and pyramids. Hence it can be said that the mesh is a discretised representation of a geometric domain.

Unstructured grid consists of simple shapes which are either triangle or tetrahedral. These grids are usually used in finite volume analysis. Unlike structured grids, unstructured grids are required to input a list of connectivity which specifies the vertices which makeup to the individual element. The quality of an unstructured mesh depends on the rate of change of cell size and then the skewness of the cell and faces. Mesh with high skew elements will result in low accuracy in the local region of the solution. The mesh produced can be improved using edge/face swapping and Laplacian smoothing. This reduces the skewness of some bad cell. As described earlier, generating a mesh involves the representation of a physical place by a suitable simulation domain.

3.9 Finite Volume Approach

There exist three types of discretization methods: Finite Differencing Method (FDM), Finite Volume Method (FVM) and Finite Element Method (FEM). The most commonly used method in fluid dynamics to solve a problem is the finite volume method. The FVM approach also resolves the Partial Differential Equation (PDE) of the conservation laws required for a CFD problem. The FVM approach carries the physical method of conservation at each cell within the entire domain. Hence it satisfies the requirement for conservation laws. Another strength of the FVM approach is that it only needs to do flux evaluation for the cell boundaries which is also applicable for non-linear problems. In this method, a domain is separated into several discrete subdomains. Each set of these sub domains are given a set of points as shown in Figure 3.2.
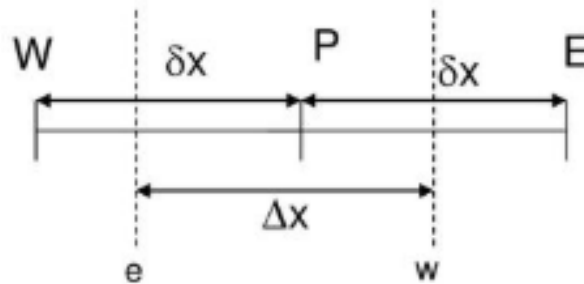
Figure 3.2: Example of Finite Volume method in 1D.

The governing equations are converted into an algebraic equation for each discrete point in the 1-dimensional model shown in Figure 3.2. The equation can be of the form

$$[A]x = B$$

3.21

Here, [A] is the sparse matrix which consists of coefficients of the algebraic equations, B is the source of vector and x is the vector of the unknown dependent.

3.10 Wall function

Wall functions rely on the law of the wall which states that velocity distribution nearer to the wall is similar for almost all turbulent flows. One of the most important parameters when calculating the applicability of wall function is the dimensionless distance y^+. Interpreting the y^+ with the Reynolds number, the magnitude can be determined along with the viscous and turbulent processes.

Walls can be a source of error in most of the flow problems. Hence, an accurate prediction of the flow and the turbulent parameters across the wall is essential. The three wall treatments are given in Figure 3.3. The wall region can be split into three sub regions:

1. Viscous sublayer
2. Log-law layer
3. Buffer layer

The non-dimensional value y^+ is used to define the thickness of these sublayers. The following plots give an insight to non-dimensional velocity u^+, as a function of y^+ across three sublayers.
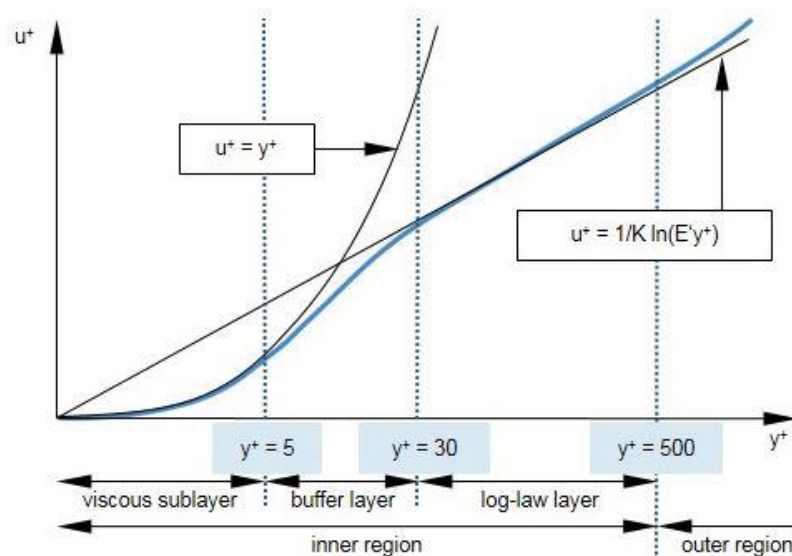
Figure 3.3: Wall y+ value for three sublayers (Star CCM+, 2020).

1. From Figure 3.3, the low y^+ wall treatment tends to resolve all the viscous sublayer. Therefore, these layers need little or no modelling to predict the flow across the wall boundary. Transport equations are solved all the way up to the wall cell. The shear stress along the wall are computed as a laminar flow. In order to resolve the viscous sublayer, an extremely fine mesh is required by these models near the wall located at y^+ around unity. The computational requirements for this kind of approach can be significant to large Reynold number flow where the viscous sublayer is very thin. Hence this wall treatment is suitable only for low Reynolds number flows.
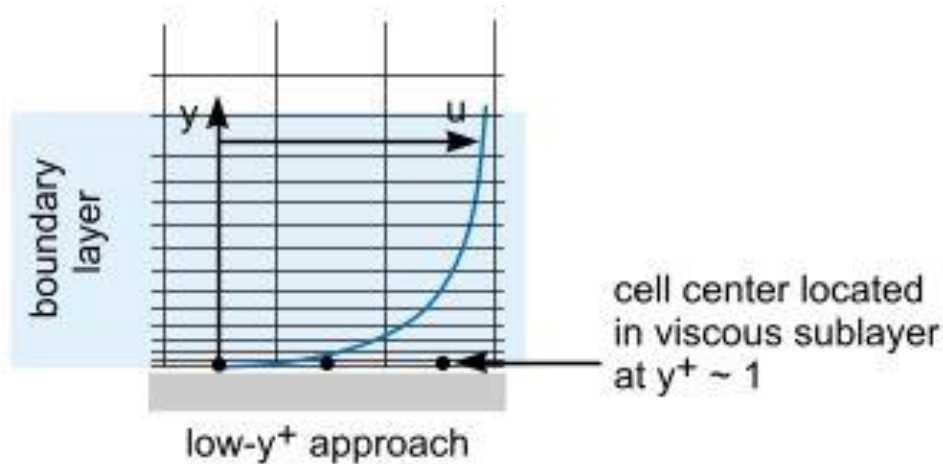
Figure 3.4: Low y+ wall approach (Star CCM+, 2020).

2. The high y^+ wall treatment is opposite to the low y^+ wall treatment. It resolves all the cells which lie at $y^+>30$ as seen in Figure 3.4. The wall shear stresses, turbulent product and dissipation rate are derived from the equilibrium turbulent boundary layer theory. The primary advantage of the high y^+ wall treatment is that there is a significant saving in the cells used.
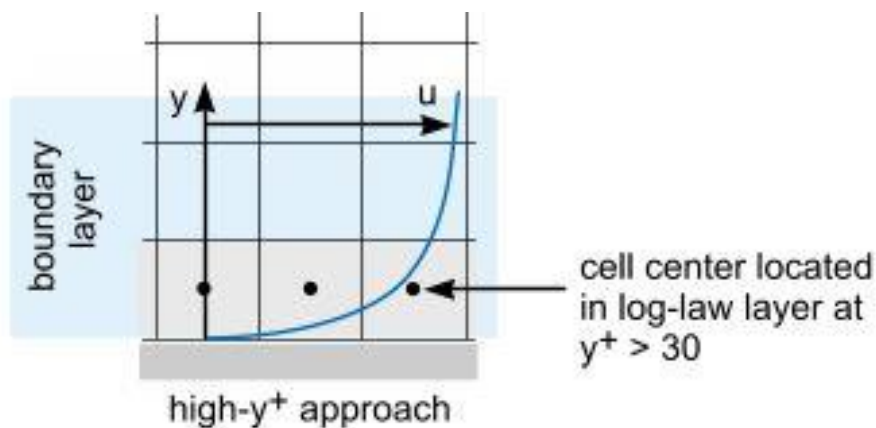
Figure 3.5: High y+ wall treatment (Star CCM+, 2020).

3. The third and final wall treatment is the all y^+ wall treatment. This is a hybrid approach which combines both the low and high y^+ wall treatment for a considerably coarse mesh. All y^+ wall treatment tend to give a reasonably good result for intermediate mesh when the wall cell centroid falls within the buffer region of the boundary layer. Hence the blending function can be used to calculate turbulent quantities like dissipation, production and stress tensor. A pictorial representation of the high wall y+ treatment can be seen in Figure 3.5.
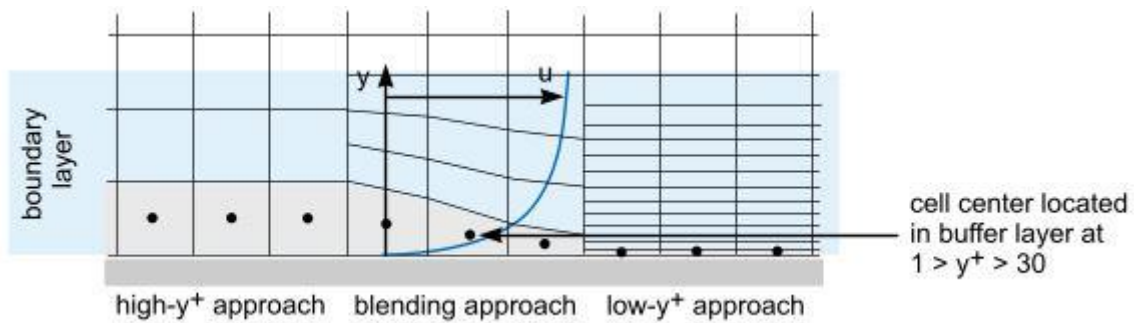
Figure 3.6: All y+ wall treatment (Star CCM+, 2020).

Not all the of the above wall treatment functions are available for RANS turbulence models. Some of the models lacks the ability to attenuate the turbulence modelling in the viscous affected regions and hence therefore can only process using a high y+ wall treatment and low Reynold number models can be simulated using a low y+ wall or all y+ wall treatment. Hence, wall treatments are optimised to the selected turbulence model. A two layer all y+ wall treatment is available for the two-layer turbulence models. This wall treatment uses an approach which is like the all y+ wall treatment. This approach contains a specific wall boundary condition for the epsilon which is consistent with the two-layer formulation in the $k - \varepsilon$ and the RSM turbulence models.

3.11 Relationship between Trucks and Tandem Bluff Bodies

From literature it is quite clear that long haul trucks are aerodynamically inefficient compared to other ground vehicles. Aerodynamic drag around a truck is identified in 4 different regions around a truck as shown in Figure 2.19. The flow field around a truck is like a flow field around tandem bluff bodies. Hence, to better understand the flow field in the gap between the tractor and trailer, an in-depth flow field analysis of the 2D and 3D tandem bluff bodies have been carried out.

Numerical simulations around 3D tandem bluff bodies give a better understanding of the flow field in the gap between the tractor and trailer and 2D simulations explain the sudden increase in drag at a critical spacing. At close spacing for the 3D bluff bodies, flow field in the gap between the bluff bodies is similar to the flow field in the gap between tractor and trailer. Strong fluid interaction exists between the vortices and main flow field around the cubes (Werle & Gallon, 1973).

The flow around multiple bluff bodies have been studied due to its practical applications (Martinuzzi & Havel, 2004) (Said, et al., 2008). Nevertheless, more detailed studies are needed on the flow field in the gap region between two bluff bodies. The current work focusses on the detailed study of the flow fields in the gap region between two identical cubes in tandem arrangement, specifically the effect of gap size on the flow field. Improved understanding of the flow field in the gap region will lead to a better understanding of the aerodynamic drag generation mechanism.

Some experimental results were reported on truck like bluff bodies in tandem by J.W.Allan (Allan, 1981) and obtained similar drag curves for both the front and rear obstacle published by Roberto.J. Martinuzzi (Martinuzzi & Havel, 2004). These two obstacles experienced drag forces in opposite signs till a critical gap. The drag becomes positive for the downstream obstacle when the gap exceeds this critical one.

Fluctuating Drag coefficients were also observed for various spacing ratios by Sakamoto et al (Sakamoto, et al., 1988). It was noted that above and below a spacing ratio, different flow patterns were observed and significant changes in aerodynamic forces found. The two different flow patterns straddling the critical spacing ratio were observed from experiments (Okajima, 1979). The first pattern resulted in shear layers separating from the upstream obstacle reattached to the downstream obstacle forming a quasi-steady vortex region within the spacing of the two obstacles. The second pattern resulted in shear layers rolling into the

spacing between the obstacles before they could reattach to the front face of the downstream obstacle (Zdravkovich, 1977). In the first flow pattern, the magnitude of negative pressure on the wake region of the front obstacle decreases and hence reduces the C_d value. In the second instance the periodically separated shear layer from the upstream obstacle move into the gap between the two obstacles resulting in increase of magnitude of negative pressure and this results in increase of C_d value. As stated by Kim et al (Kim, et al., 2008), the characteristics of aerodynamics forces strongly depend on shape (Sakamoto, et al., 1987) and spacing between structures and the direction of wind. In this study we will only focus on a simple approach to investigate and understand these characteristics from a practical point of view.

Figure 3.7 shows the predicted drag coefficient results for the GTS test case and Figure 3.8 shows the mean drag coefficient as predicted around the downstream cube of 2D and 3D tandem surface mounted bluff bodies. From both Figure 3.7 & Figure 3.8, a trend of a sudden rise in the drag coefficient of the downstream bluff body was observed.
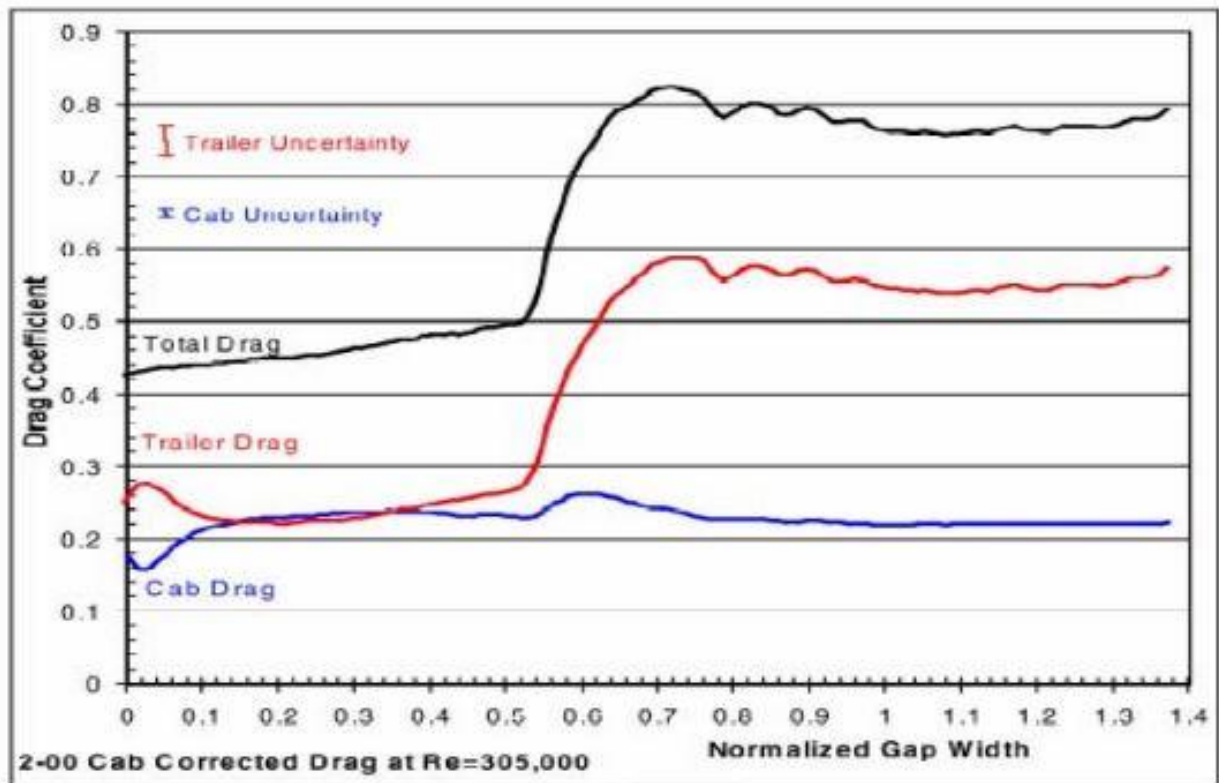
Figure 3.7: Drag coefficient of the GTS model (Sitlani & Aung, 2006).
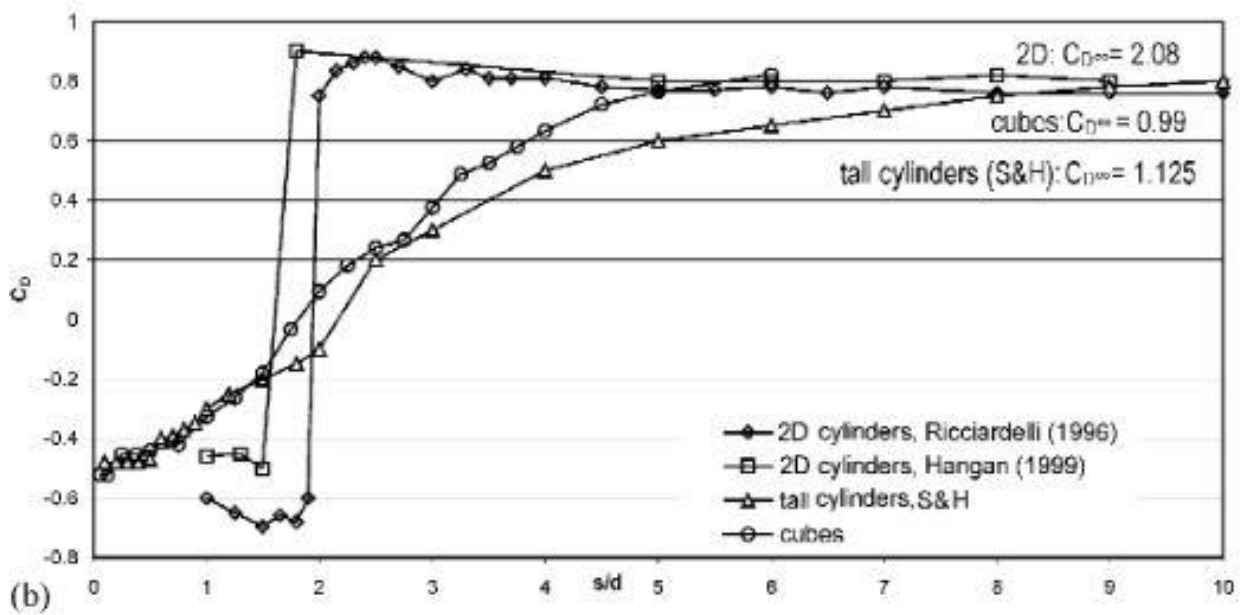
Figure 3.8: Mean drag coefficient as predicted on the downstream cube at various D/H ratios (Havel, et al., 2001).

93

3.12 Scope and Objective of Thesis

This present study aims to assess and improve the flow field in the gap between a tractor and trailer using computation fluid dynamics (CFD) method. Several objectives are outlined from the previous sections about the flow field in the gap.

- To simulate suitable test case to predict and understand flow field in the gap between tandem bluff bodies (2D and 3D tandem bluff bodies).
- To validate steady state numerical results with the data from published experimental results.
- To examine the flow field in the gap at different gap ratios to understand the changes in flow field.
- To analyse the flow field and understand the flow mechanism within the gap region between the trailer and tractor.
- To analyse the latest aerodynamic drag reduction devices.
- To develop an efficient device to minimise the aerodynamic drag generated from the gap.

Chapter 4

Two Dimensional and Three Dimensional Bluff Body Flow

Abstract

Numerical simulations have been carried out to advance our current understanding of flow around two dimensional (2D) and three dimensional (3D) square shaped tandem bluff bodies at a Reynolds number of 22,000, especially to shed light on the sudden change of the downstream cube drag coefficient. A steady Reynolds-Averaged Navier-Stokes (RANS) approach has been employed in the present study and the predicted drag coefficients compare reasonably well with available experimental data. Better understanding of flow fields has been achieved by analysing streamlines, velocity contours for both 2D and 3D cases in a horizontal plane and a vertical plane. The pressure distributions on various faces of the cubes have been examined in detail. The sudden jump in drag coefficient for the 2D case is well captured numerically, which is due to the flow around the upstream cube impinging onto the front face of the downstream cube. For the 3D case the drag coefficient is predicted to increase gradually, consistent with the previous experimental findings, and this is because vortical structures formed in the 3D case are quite different, resulting in smooth change of flow fields around the cubes and hence leading to gradual, not sudden, increase of drag coefficient.

Chapter 4 is split into two sections. The first section explains the flow field in the gap region for two dimensional cubes and the second section deals with the flow field in the gap region for three dimensional cubes.

Section 4.1

Impacts of Gap Size between Two Bluff Bodies (2D) on the Flow Field within the Gap

4.1.1 Introduction

The aerodynamic study of bluff bodies has been a subject of interest in variety of scientific research. Tandem bluff bodies have several practical significances. Fluid flow research around bluff bodies is being used across number of engineering applications like solar heating systems, offshore structures, aerospace, heat exchangers, automotive, skyscrapers etc. The area of interest in bluff body aerodynamics is the flow field in and around the two cubes in tandem. The wake of a bluff body generates several forces that have the potential to affect a neighbouring bluff body. In order to reduce the impact caused by the wake of bluff bodies several strategies have been researched which could weaken the wake and reduce the amplitude of the fluctuating forces (Darekar & Sherwin, 2001).

The research has been focussed on wake study and drag of bluff bodies which can be related to several different engineering disciplines. Research on these topics have increased in the last few decades due to their simple yet practical and realistic values. Wake from a bluff body can potentially affect a neighbouring bluff body. Hence, flow field around a bluff body could significantly impact the neighbouring structures. Fluid flow around a rigid bluff body strongly depends on their shape and size, distance between each body, their orientation with respect to each other and their individual orientation to the active external forces. Hence controlling this flow and improving the flow field around these bluff bodies have been a major cause of concern and cause numerous problems for engineers in fluid mechanics.

A number of experimental studies have been conducted for high Reynold number flow past a square cylinder which has been widely investigated since the beginning of 1990s (Park, 1995), which has laid the foundation for computational simulations to be carried out (Stoesser, et al., 2003). Several experimental investigations have been carried out on tandem bluff bodies. The focus has been on understanding the wake around the cubes with respect

to change in gap ratios (Havel, et al., 2001) (Martinuzzi & Havel, 2004). Several studies on bluff bodies have been conducted on a single cylinder or cube which is either two dimensional (2D) or three dimensional (3D) in shape. A 2D obstacle is an object which extends a long way (theoretically, it should be infinitely) in the spanwise direction in order to neglect three dimensional effects of the flow. A 3D body is a surface mounted cube placed on the floor of the domain. Flows around a 2D geometry differ considerably compared with a 3D geometry due to vorticity from the oncoming boundary layer.
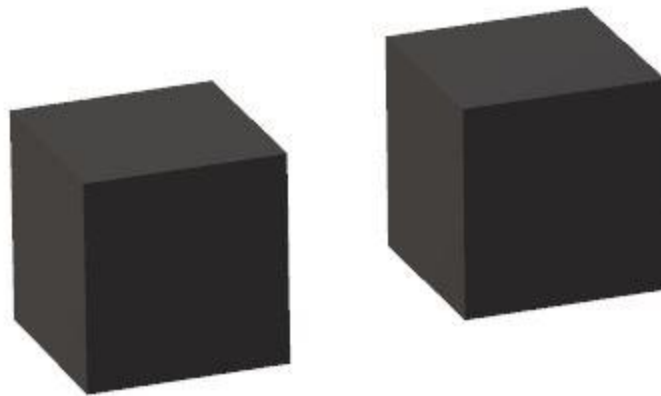
Figure 4.1:Tandem bluff bodies with square cross section.

Experiments carried out by Zdravkovich (Zdravkovich, 1977) provide an extensive information for twin circular cylinders in a tandem arrangement. The author identified 5 different flow field regimes in his experiments as depending on the inter obstacle spacing. (1) For a small spacing, the separated shear layer from the first obstacle tends to overshoot the second obstacle. Wake characteristics are very similar to that of a flow around a single body. (2) For a slightly increased spacing, the shear layers from the upstream cylinder alternately reattach along the sides of the second obstacle. (3) For increased spacing, the author describes the flow experiencing a quasi-steady reattachment, resulting in an irregular flow pattern and loading on the cubes. (4) When the second cube is mounted at the end of the recirculation region, the boundary layer form the second cube is disturbed and the vortex street become intermittent and (5) for a larger spacing the wake of both the upstream and downstream cube do not interrupt with each other and are independent of the main flow. The type of flow experienced in (2) and (3) are described as a bi-stable regime by Zhang and Melbourne (Zhang & Melbourne, 1992). From (Havel, et al., 2001) , the wake of a 2D model is characterized by large scale vortical structures which rotate about the span wise axis. Five different flow patterns have been identified from previous experimental test by

(Zdravkovich, 1977) (Hangan & Vikery, 1999) and these patterns are qualitatively similar to those found by (Zhang & Melbourne, 1992) for circular cylinders.

In this chapter, the numerical approach used to investigate 2D and 3D models will be presented briefly and the flow fields around those two models as a function of inter cubic spacing will be analysed. The bluff bodies are positioned on the centreline of the domain. The flow field analysis is carried out using flow visualization and comparison with data from previous literature will also be presented. The first part of the chapter discusses about the methods, computational setup and results for 2D bluff bodies and the second part of the chapter discusses about 3D bluff bodies.

4.1.2 Computational Domain and Boundary Conditions
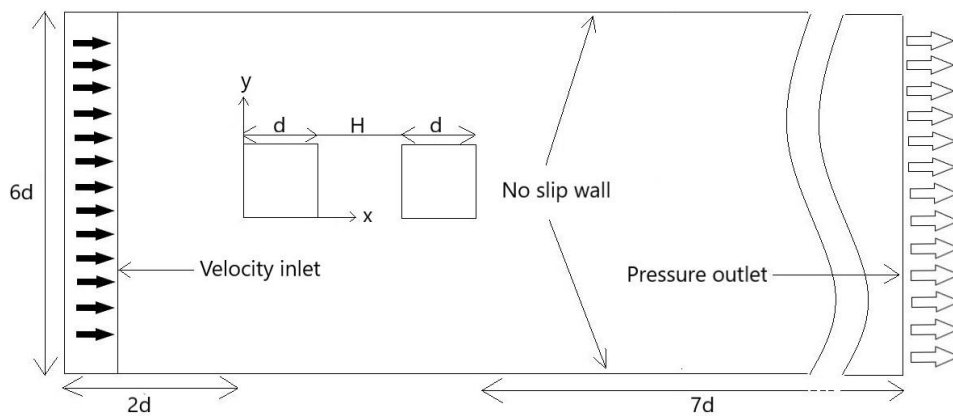
Figure 4.2: 2D computational domain (Side view).
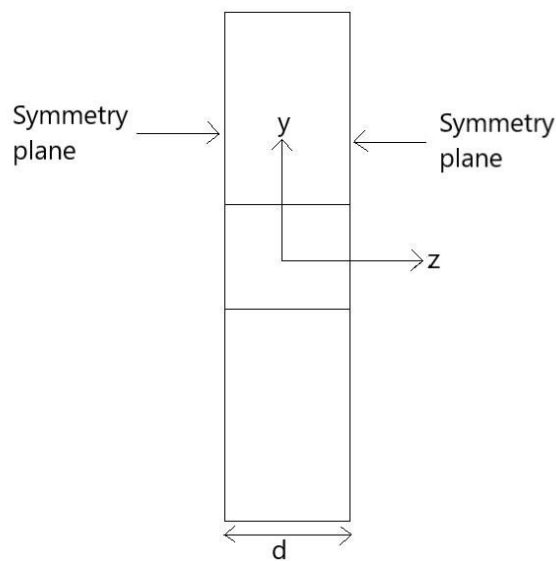
Figure 4.3:2D computational domain (Front view).

The dimensions of the computational domain are the same as the wind tunnel used for experiments by R.J. Martinuzzi (Martinuzzi & Havel, 2004). A schematic of the 2D computational domain is shown in Figure 4.2 and the domain has an upstream length of 2×D (D =0.04m) and a downstream length of 7×D from the back face of the 2nd cube. The width of the domain is equal to the width of the cube (D) as seen in Figure 4.3. The two lateral walls of the domain are assigned to symmetry plane to make sure that it is two-dimensional flow (flow over a 2D body which had an infinite length in the third dimension). Two identical cubes (D = 40mm) are mounted in tandem. Simulations have been carried out to investigate the flow field at various gap sizes (H, the distance between the two cubes). The top and bottom wall of the domain are assigned to a no slip wall condition. Wall boundary conditions of the computational domain are set to match the wind tunnel conditions from experiments (Havel, et al., 2001). A velocity inlet is assigned at the inlet of the domain and pressure outlet is assigned at the outlet.

4.1.3 Numerical Procedure

The incompressible turbulent steady flow around 2D and 3D tandem bluff body is modelled using the so-called Reynolds-Averaged Navier-Stokes (RANS) approach (the instantaneous governing equations are time averaged). The RANS governing equations (continuity and the momentum equations) for incompressible flow can be written as:

$$\nabla.(\rho\bar{v}) = 0 \qquad \qquad 4.1$$
$$\nabla.(\rho\bar{v}\otimes\bar{v}) = -\nabla.\bar{p}I + \nabla.(T + T_t) + f_b \qquad \qquad 4.2$$

Here, $\bar{v}$ is the mean velocity contour, ρ is density, I is the unit identity tensor, T is the viscous stress tensor, T_t is the Reynolds stress tensor, f_b is the body forces (usually neglected). A turbulence model is needed to approximate T_t before the above equations can be solved and there are many turbulence models available. In the present study, the realizable $k - \varepsilon$ turbulence model is chosen since this turbulence model can predict complex flow structures such as vorticity, separation, re-circulation better than the standard $k - \varepsilon$ model [4] and other two equation turbulence models. More advanced turbulence models based on Reynolds stress transport equations, called Reynolds Stress Models (RSM), are available but computationally it is very expensive to use a RSM and also in many flow cases a RSM does not show superiority over two equation turbulence models.

The transport equations for kinetic energy k and dissipation rate ε in the realizable $k - \varepsilon$ turbulence model cab be written as:

$$\frac{\partial}{\partial t}(\rho k) + \nabla.(\rho k \bar{v}) = \nabla.\left[\left(\mu + \frac{\mu_t}{\sigma_k}\right)\nabla k\right] + P_k - \rho(\varepsilon - \varepsilon_0) + S_k \qquad 4.3$$

$$\frac{\partial}{\partial t}(\rho \varepsilon) + \nabla.(\rho \varepsilon \bar{v}) = \nabla.\left[\left(\mu + \frac{\mu_t}{\sigma_\varepsilon}\right)\nabla \varepsilon\right] + \frac{1}{T_\varepsilon}C_{\varepsilon 1}P_\varepsilon - C_{\varepsilon 2}f_2 \rho \left(\frac{\varepsilon}{T_\varepsilon} - \frac{\varepsilon_0}{T_0}\right) + S_\varepsilon \qquad 4.4$$

Here, f_2 is a damping function, μ is dynamic viscosity, μ_t is the turbulent viscosity, $\bar{v}$ is the mean velocity contour, ε_0 is the ambient turbulence value, $\sigma_k, \sigma_\varepsilon, C_{\varepsilon 1}$ and $C_{\varepsilon 2}$ are model coefficients.

Simulations have been performed using a commercial CFD package - Star CCM+ and a 2nd order upwind scheme is used which enable Taylor's series expansion for the cell centroid (Ansys, INC;, 2009).An all y+ wall treatment which combines high y+ wall treatment for the coarse grid and low y+ wall treatment for the fine grid are employed (Research Gate,, 2016).

The drag coefficient and pressure coefficient are defined below as:

$$C_d = \frac{2F_d}{\rho U^2 A} \qquad 4.5$$

$$C_p = \frac{p - p_\infty}{0.5\rho_\infty U_\infty^2} \qquad 4.6$$

In the above equations 4.5 & 4.6 for drag coefficient and pressure coefficient, F_D is the drag force, A is frontal area, ρ is the fluid density, U is the fluid velocity, p is the statis pressure and p_∞ is the static pressure in the freestream. In the above equation the drag force F_D can be calculated by:

$$F_D = kU^2 \qquad 4.7$$

Where k is the air resistance coefficient.

4.1.4 Drag Coefficient
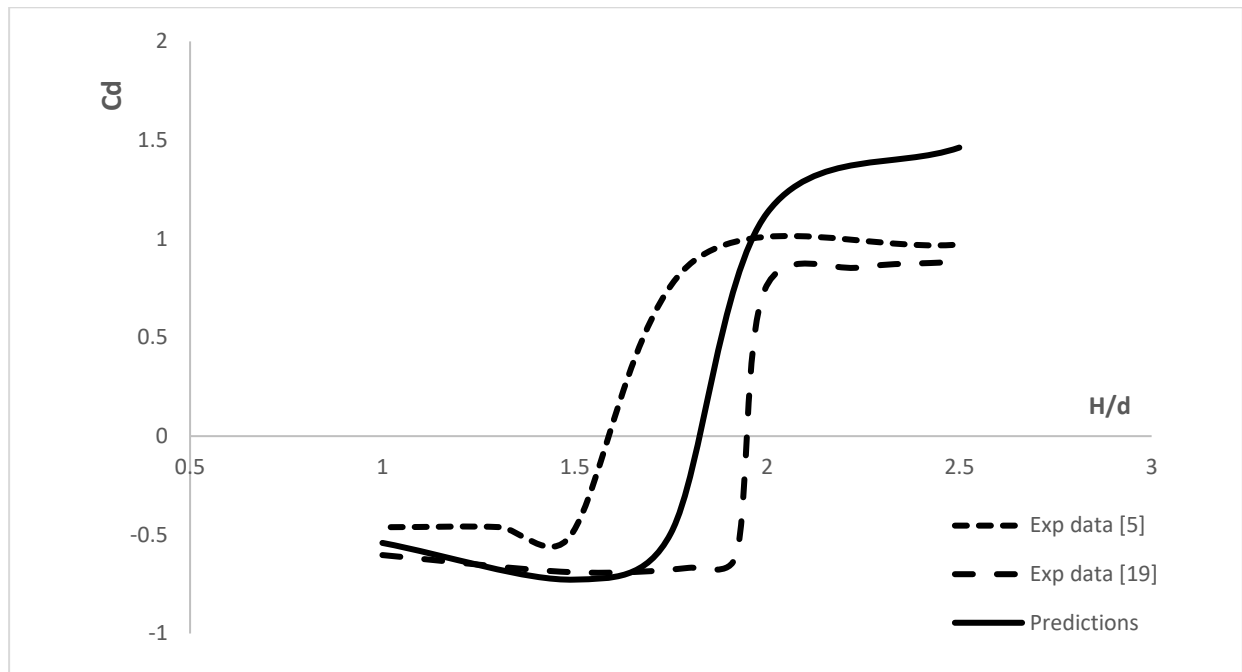
Figure 4.4: Comparison between the predicted drag coefficients and the experimental data for the downstream cube.

Figure 4.4 presents drag coefficients against the dimensionless gap size (H/D) for the downstream cube and experimental data (Hangan & Vikery, 1999) (Ricciardelli, 1994) show a sudden increase of drag coefficients at certain gap sizes. This sudden increase of drag coefficients is well captured by the predictions. Nevertheless, the predicted jump occurs at around H/D = 1.7 and the data by Ricciardeli (Ricciardelli, 1994) show that the jump happens at about H/D = 1.45 whereas the data by Hangan & Vickery (Hangan & Vikery, 1999) show that the jump takes place at about H/D = 1.95. The predicted drag coefficient values are reasonably close to the experimental data before the jump. However after the jump there are some discrepancies between the predictions and the experimental data since the predicted drag coefficients still keep on increasing gradually with the gap size whereas the measured drag coefficients are more or less the same, not changing with the gap size. Detailed analysis will be presented below to reveal the change of the flow fields when the gap size changes, leading to a better understanding of the drag coefficient variations observed in Figure 4.4.

4.1.5 Flow Field
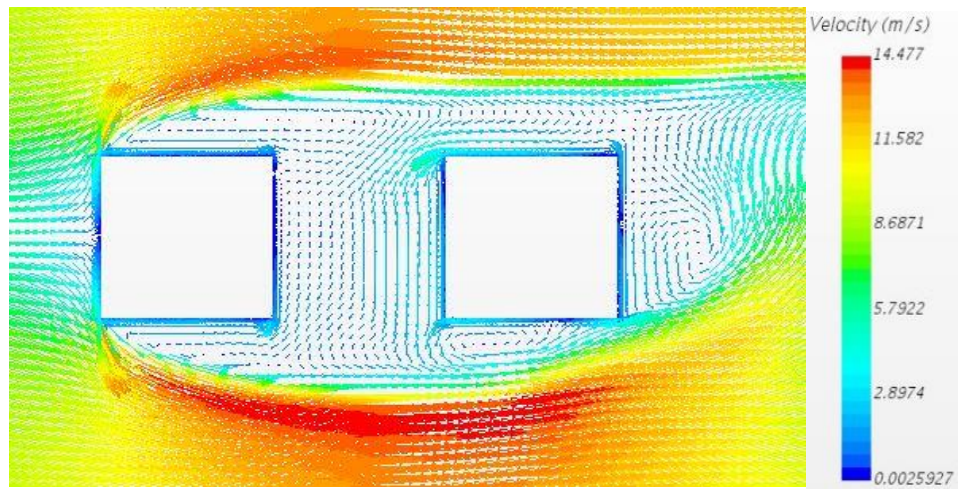
(a)
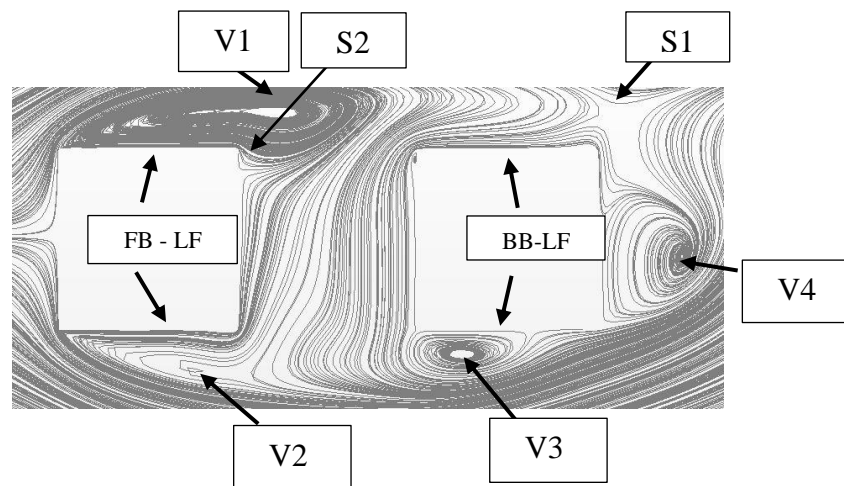
(b)

Figure 4.5: Flow field viewed at a gap ratio of H/D = 1 for 2D tandem bluff bodies. (a)Velocity contours, (b) streamlines.
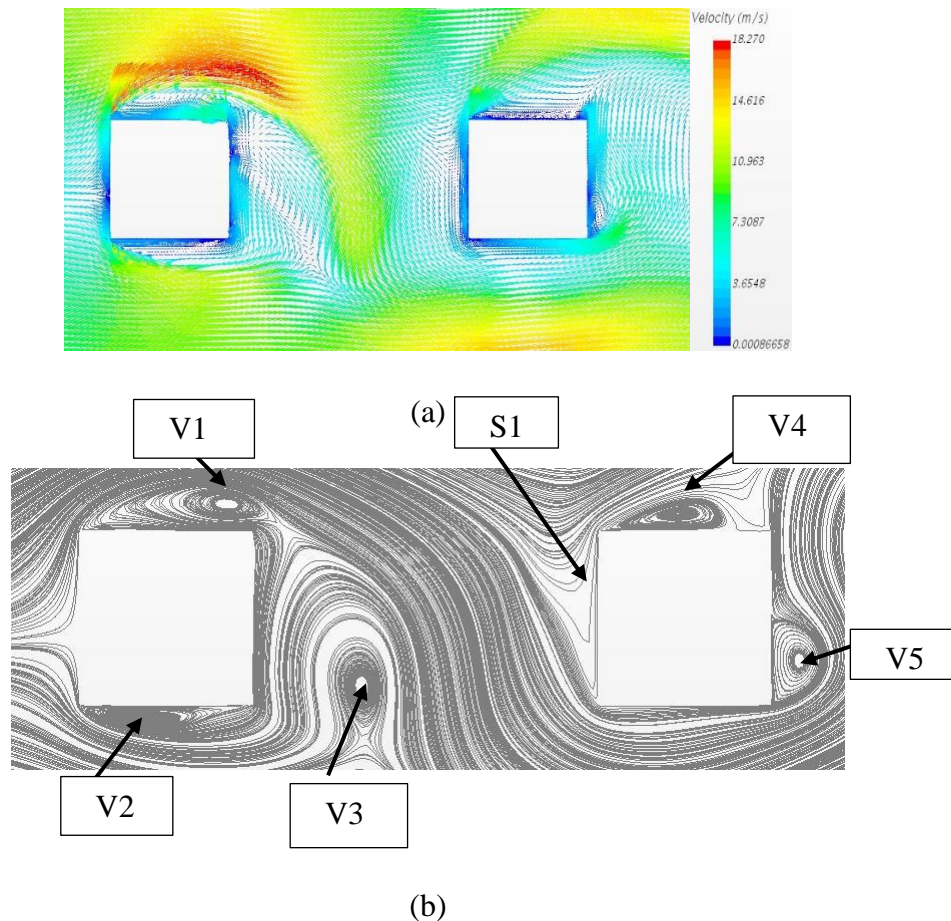
Figure 4.6:Flow field viewed at a gap ratio of H/D = 2 for 2D tandem bluff bodies. (a)Velocity contour, (b) streamlines.

Figure 4.5 & Figure 4.6 show the mean velocity contour and streamlines around 2D tandem bluff bodies at two gap ratios (H/D= 1, 2) and it can be seen from Figure 4.5a that at H/D = 1, after flow impinges on the front face of the cube about half of the flow goes upwards and another half goes downwards, and then separates at the leading edge of the top and bottom surfaces of the cube. One distinct feature is that the top flow and bottom are not symmetric at all. It can be seen more clearly from Figure 4.5b that a large recirculation bubble (V1) appears on the top surface of the upstream cube and a large portion of the flow around the top surface of the upstream cube enter the inter cube region (gap region). However, on the bottom surface of the upstream cube a smaller recirculation bubble forms (V2) and only a small percentage of flow enters the gap region. The flow around the downstream is even more asymmetric since there exists a separation bubble (V3) near the leading edge of the bottom surface while no such a separation bubble forms near the leading edge of the top surface at all. In the wake region behind the downstream cube a single large recirculation region is clearly observable. A similar flow pattern appears in (Hangan & Vikery, 1999) where a single vortex is formed in the wake region on the backward face of the downstream

105

cube. As shown in Figure 4.4 that at this gap ratio (H/D = 1) the drag coefficient for the downstream cube is negative and this is because the pressure force on the back face of the downstream cube is larger than the pressure force on the front face of the downstream cube. The relatively low pressure on the front face of the downstream cube is due to the fact that there is no direct impingement of flow on this face and also that the flow travels through the gap region relatively quickly compared with the flow at the back face where a large vortex is formed there.

When the gap size increases to H/D = 2, the flow becomes more asymmetric apart from the flow on top and bottom of the upstream cube where reasonably two similar separation bubbles (V1 & V2) appear as shown in Figure 4.6. The uneven size of the vortices V1 and V2 influence the flow field on the front face of the cube, resulting in a separation point away from the centre of the cube. Significant change can be observed behind the upstream cube with a large vortex formed in the gap region (V3) as shown in Figure 4.6b. The flow in the gap region is mainly from top of the upstream cube, which impinges at angle onto the front face of the downstream cube, resulting in high pressure on this surface and this is why the pressure coefficient for the downstream cube increases rapidly from a negative value to a positive value as shown in Figure 4.4. The flow filed on top of the downstream cube is totally different from that at the bottom as shown in Figure 4.6b, and also the vortex formed at the back of the downstream cube (V5) becomes smaller compared with the case at H/D = 1. The uneven pattern in the flow field is due to the nature of the flow around 2D tandem bluff bodies. Experiments predict a variety of flow feature at different gap ratios, however asymmetric nature of the flow in both the cases are due to the steady RANS approach which captures only one instance of the flow behaviour.

Section 4.2

Impacts of Gap Size Between Two Bluff bodies (3D) on The Flow Field Within the Gap

4.2.1 Introduction

The aerodynamic study of the flow field around bluff bodies has been a subject of immense interest across several scientific studies. The wake region of a bluff body is of high priority due to the drag generated from the bluff body itself. Aerodynamic study of bluff bodies has a practical significance and is applied in different engineering disciplines such as Civil Engineering, Automotive Engineering and Aerospace Engineering etc. Studies on these topics have increased in the last few decades due to their simple geometry but practical and realistic significance. This vehicle type is in use for transporting majority of the goods across a country and appreciable drag reduction has been achieved by modifying the design or by adding simple ad-on devices (Holmes, 1976).

An important feature of bluff body flow is the flow separation where the location of separation may strongly affect the aerodynamic characteristic of the body. The most used bluff body shapes are (a) circular cylinder and (b) square cylinder. The arrangement of these bluff bodies can range from tandem to staggered arrangement

The flow around 3D rectangular bluff bodies has been studied due to their practical applications (Havel, et al., 2001) (Charles, et al., 2017) .Flow field around 3D tandem bodies consist of very complex characteristics with the formation of streamwise and spanwise vortices which interact with each other. The vortices formed at the rear of the obstacle tend to change the flow field and the downstream recovery of the flow. Numerous previous studies have been done on flow around two tandem circular cylinders and relatively little attention has been focused on flow over two tandem square cylinders. Several previous studies on square cylinders have demonstrated that the gap spacing between the two tandem cylinders has a great impact on the flow field around the cylinders. Some dramatic changes of flow pattern occur at a critical spacing (Sakamoto, et al., 1988) (Luo & Teng, 1990), leading to the surface pressure, drag coefficient, and vortex-shedding frequency being altered rapidly around the critical spacing. In particular, it has been found that when the gap spacing is bigger than the critical spacing a sudden significant increase in the drag force occurs to

the downstream cylinder. Fluid is exchanged between different separation regions around any three-dimensional bluff bodies. (Werle & Gallon, 1973). This sudden increase is very sharp in the 2D flow case while in the 3D flow case the drag force increases gradually. However, the mechanisms behind the sharp increase in the 2D case and the gradual increase in the 3D case is not fully understood and the main objective of the present study is to advance our current understanding in this area through a detailed numerical studies of 2D and 3D flows around tandem bluff bodies.

4.2.2 Boundary Conditions (3D):

The setup for numerical simulation is based on the experimental study carried out by R.J. Martinuzzi et al (Martinuzzi & Havel, 2004). Two identical cubic blocks (D = 40) mm are arranged in tandem with a gap size of H (the distance between those two cubes) and mounted on the floor of the domain. The dimensions of the computational domain are given in Figure 4.7. A symmetric plane is used on the XY plane at z=0. This approach enables the use of only half the domain resulting in the reduced mesh points and simulation time. A schematic front view of the computational domain is shown in Figure 4.8. The working fluid is air and the inlet velocity is at 8.8m/s, corresponding to a Reynolds number of 22,000 based on the cube height. A pressure outlet boundary condition imposes the working pressure at the outlet. The boundary pressure at the outlet is considered as the static pressure of the working fluid (Star CCM+, 2020). The inlet turbulence intensity from the experiment is 1.5% and the same value has been assigned for the numerical simulations in this research. Simulations have been conducted at several gap sizes to investigate the influence of the gap size on the flow field.
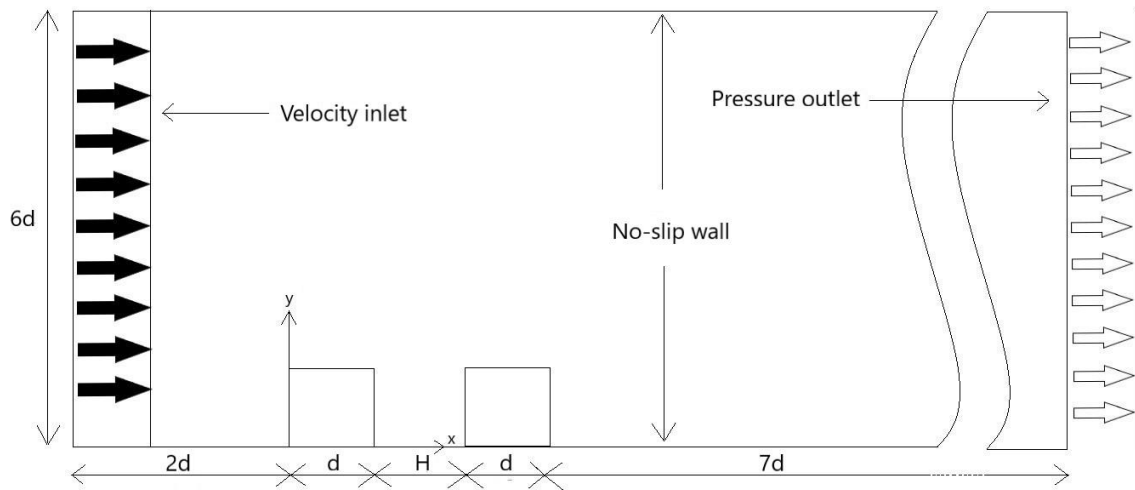
Figure 4.7: Schematic drawing on the symmetry plane of two cubic tandem obstacles.
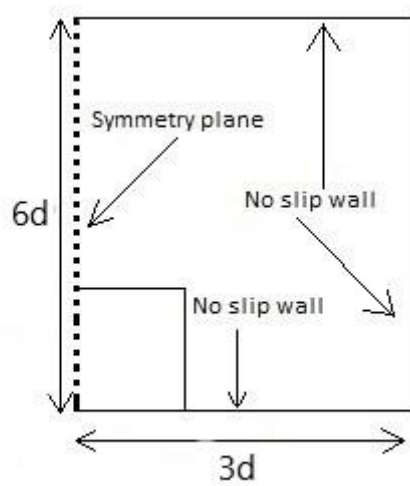
Figure 4.8:Front view of computational domain with symmetry plane.

4.2.3 Validation

The CFD code used in the current study is STAR CCM+ and the realizable $k - \varepsilon$ turbulence model is chosen with an all y+ wall treatment - a hybrid wall treatment combining high y+ wall treatment for coarse meshes, and the low y+ wall treatment for fine meshes. The numerical study was first validated against different set of experimental results (Said, et al., 2008). Two tandem obstacles with rectangular cross section and a dimension of 88mm(h) $\times$ 90mm (l) $\times$ 59mm (L) are simulated. The inlet velocity is 8.0 m/s, corresponding to a Reynolds number of 46,000. In order to Figure 4.9 shows the predicted mean streamwise velocity profile and the experimental data on the symmetrical XY plane at position of 30 mm away from back of the first obstacle. The predicted velocity profile compares well with the experimental data, confirming that the current numerical approach is appropriate for studying this kind of flow.
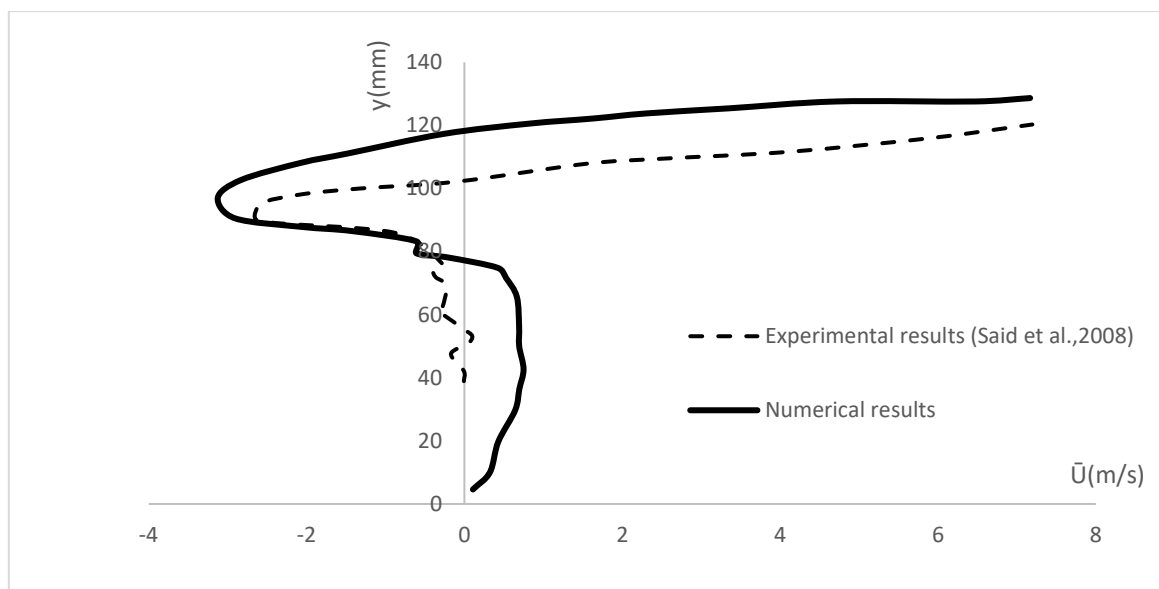
Figure 4.9: Mean velocity profile on the symmetry plane.

Figure 4.10 presents a qualitative comparison between the predicted velocity contours and the experimental results on the XZ plane at half of the cube height (Y/D = 0.5). It can be seen that the general flow features observed in the experiment are well captured by the simulation with the fluid entering the gap from the lateral sides, creating a horseshoe like vortex in the gap region. Another horseshoe vortex formed in the wake of the downstream cube is also clearly observable from both the predictions (Figure 4.10a) and the experimental results (Figure 4.10b). Due to the averaging method used by the turbulent solvers, the flow

features in the wake region have minor discrepancies, especially comparing the wake region of the downstream obstacle. The size of the vortex in the wake region of the downstream cube is slightly longer in the RANS approach compared to experimental results. However, the main flow features are predicted well by the numerical approach employed in this study. The predicted data for the validation of the current CFD study against the experimental results demonstrates that the present employed CFD approach is reasonably accurate and robust for this kind of flow.
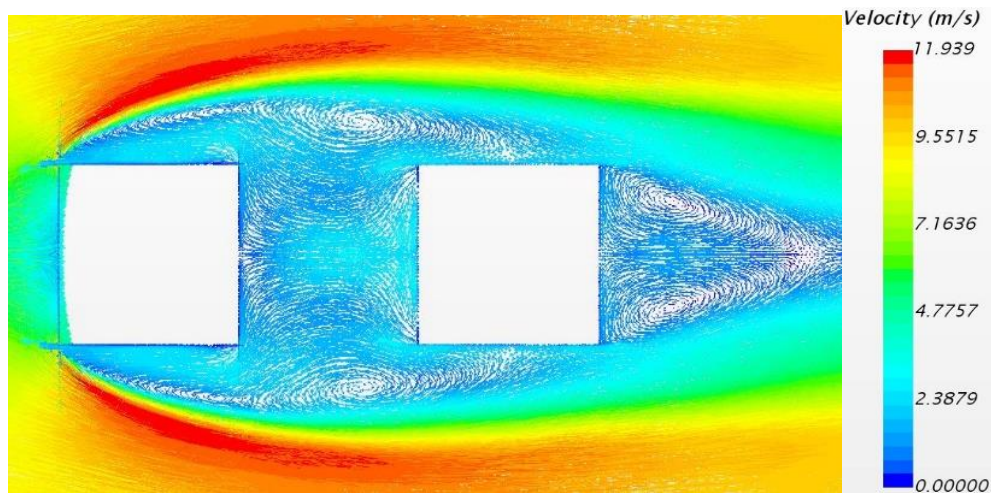
(a)
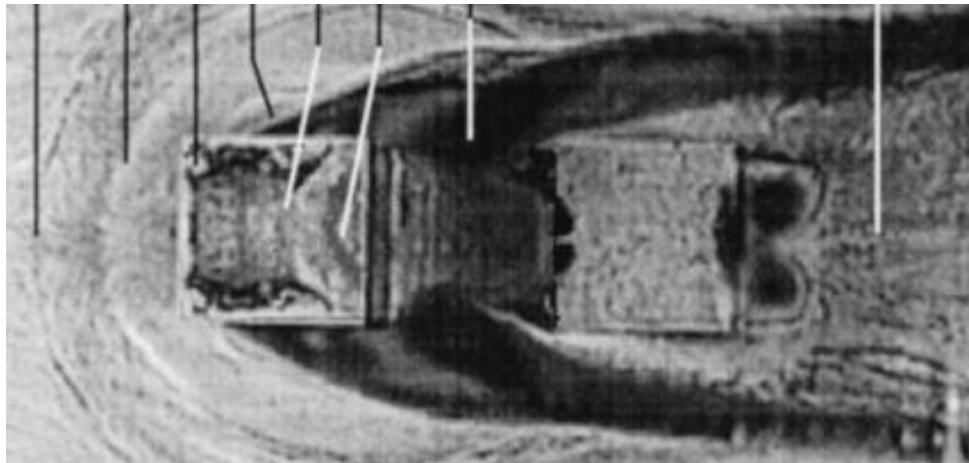
(b)

Figure 4.10: Velocity contour on the XZ plane at half the height of the block at H/D = 1, (a) – predictions; (b) – experimental results (Martinuzzi & Havel, 2000).

4.2.4(a) Effects of the Gap Size on the Drag Coefficient of the Downstream Cube.

Figure 4.11: Drag coefficient predicted around downstream cube at various H/D ratios.

The focus in the current study will be on the drag coefficient of the downstream cube when the gap size varies and Figure 4.11 plots the drag coefficient of the downstream cube against the dimensionless gap size (H/D). Unlike the 2D case in the previous section, the increase of the drag coefficient with the increase of the gap size for the 3D case is not so sharp as it starts to increase gradually at about H/D = 1.47 till about H/D = 1.75, and after this a more steep increase occurs till about H/D = 2. The steady increase in drag coefficient is due to the wake of the upstream cube reduces the interaction with the downstream cube and is formed within the inter cubic spacing resulting in reduced suction effect around the downstream cube. Further flow field analysis on the symmetry XY plane will be presented below to have a better understanding of the drag coefficient variations shown in Figure 4.11.

4.2.4(b) Impact of Gap Size on Flow Field

Figure 4.12 shows the flow field on the symmetry XY plane at H/D = 0.5 and it can be seen that very complex flow structures are generated. The flow separates at the leading edge of the upstream cube and reattaches to the top surface of the downstream cube forming a single semi-elliptical shaped recirculation region on top of the two cubes. This acts like a single vortex at the top face of both cubes and there is not a strong interaction between this vortex and the flow inside the gap region. The flow field in the gap region is dominated by a large vortex occupying almost 80% of the total gap region and some small flow structures are formed in the bottom half of the gap region near the wall. Since there is no strong interaction between the flow inside the gap region and the flow outside it, and especially no flow impingement on the front face of the downstream cube, the total pressure force on the front face is relatively smaller than the total pressure force on the back face, resulting in a negative drag coefficient at this gap size as shown in Figure 4.11. In the wake region behind the second cube, a typical vortex is observed which is commonly reported in flows over a single cube and a backward facing step.
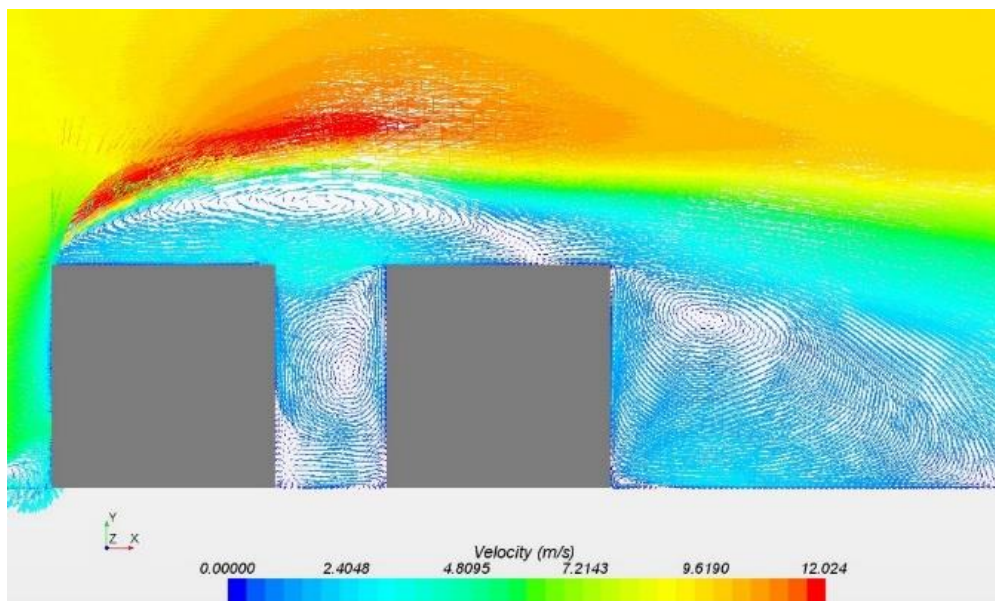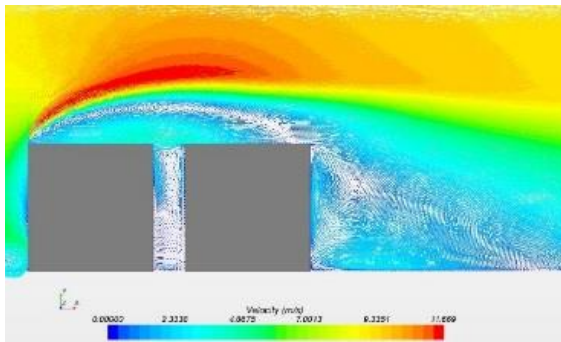

Figure 4.12: Velocity contour on the symmetry XY plane at H/D = 0.5.

Figure 4.13 shows velocity contours on the symmetry XY plane at three gap sizes (H/D = 0.25, 0.75 and 1) and in the case at H/D = 0.25, the primary recirculation zone on top of the two cubes and the flow field in the wake of the second cube resemble that at H/D = 0.5 as shown in Figure 4.12. However, the flow field in the gap region is quite different from the case at H/D = 0.5 as the flow field is not dominated by a single large vortex anymore, with some smaller but quite complex flow structures as shown in Figure 4.13a. Similar to the case at H/D = 0.5 there is no flow impingement on the front face of the second cube and hence the drag coefficient is also negative as discussed above.

For the case at H/D = 0.75, the single semi-elliptical shaped recirculation region on top of the two cubes observed at H/D = 0.25 and 0.5 is still just about observable as shown in Figure 4.13b and is in the brink of breaking into two recirculation zones. It can be also seen that there is more interaction between the flow inside the gap region and the flow outside it. The flow field in the gap region becomes more complex, which is not dominated by a large single vortex. The flow field in the wake region behind the second cube resembles from the previous cases. The drag coefficient remains negative as the total pressure force on the front face of the second cube is still less than the total pressure force on the back face.

When the gap size increases to H/D = 1.0, the single semi-elliptical shaped recirculation region on top of the two cubes observed in the previous two cases breaks into two recirculation regions as shown in Figure 4.13c, leading to a much stronger interaction between the flow above the cubes and the flow inside the gap region with more flow entering the gap region. However, the flow entering the gap region does not impinge on the front face of the second cube and hence the total pressure force on the front face is still smaller than that on the back face, keeping the drag coefficient as a negative value. The gross flow field in the wake region behind the second cube is more or less the same as those in the previous three cases.

When the gap size increases further to H/D = 2.0, the single and two semi-elliptical shaped recirculation regions on top of the two cubes observed in the previous three cases disappear completely as shown in Figure 4.13d. Furthermore, a large proportion of flow past the upstream cube enters the gap region and impinges on the front face of the downstream cube, resulting in a large increase pressure on this surface and hence leading to a significant increase of the drag coefficient as shown in Figure 4.11.

(a) H/D = 0.25.
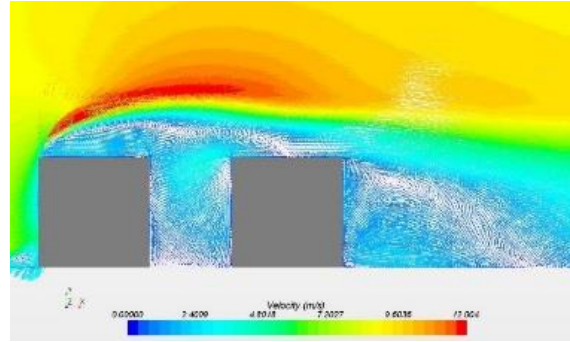
(b) H/D = 0.75
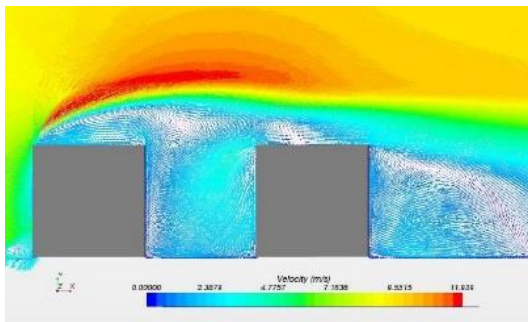
(c) H/D = 1
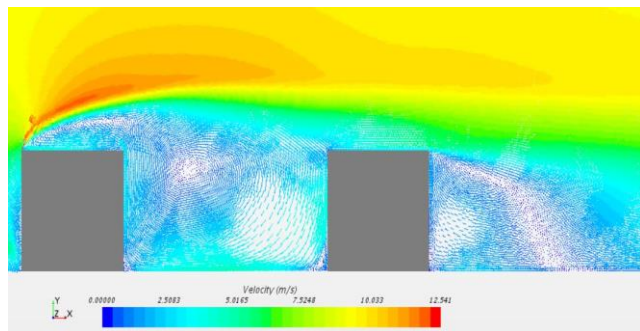
(d) H/D = 2

Figure 4.13: Velocity contour on the symmetry XY plane at different gap sizes (H/D = 0.25, 0.75, 1 and 2).

4.2.5 Summary

Steady RANS simulations with the realizable $k - \varepsilon$ turbulence model have been successfully employed to predict and understand the flow around tandem 2D and 3D bluff bodies. The CFD predictions have been first validated against the experimental data and a reasonably good agreement has been achieved in Figure 4.9. Comparing the quantitative results in Figure 4.10, minor discrepancies are predicted by simulation. This is due to the averaging method employed by RANS simulation approach. However, the major features of the flow field have been predicted to a satisfactory level, demonstrating that the CFD approach used in the present study is reasonably accurate and reliable for the flow around tandem 2D and 3D bluff bodies.

Detailed flow field analysis has been carried out and a good understanding for the sudden increase of the drag coefficient for the downstream cube in the 2D case has been obtained. This is because at a critical gap size a large proportion of flow enters from top of the gap region, leading to flow impingement on the front face of the downstream, resulting in high pressure on this face and hence a sudden in the drag coefficient. Nevertheless, for the 3D case the drag coefficient for the downstream cube does not increase so sharply as in the 2D case because the flow can enter the gap region from two lateral sides, leading to more complex flow in the gap region such as formation of a horseshoe vortex and no sudden flow impingement on the front face of the downstream cube at any gap sizes.

Chapter 5

Validation of Simplified Tractor-Trailer Model

5.1 Introduction

The chapter gives a detailed insight into the validation process by which the obtained numerical results are compared with experimental data to assess the accuracy and robustness of the computational approach used in this study, and to identify the most suitable turbulence model for the current study. Furthermore, an in-depth analysis of flow field and pressure distribution has been carried out for a generic truck like test case.

5.2 Computational Setup

The computational domain dimensions are selected to match those of the wind tunnel used in experiments by Jan Osth et al (Osth & Krajnovic, 2012). Figure 5.1 and Figure 5.2 show the side view and the front view of the computational domain where b = 0.305m.
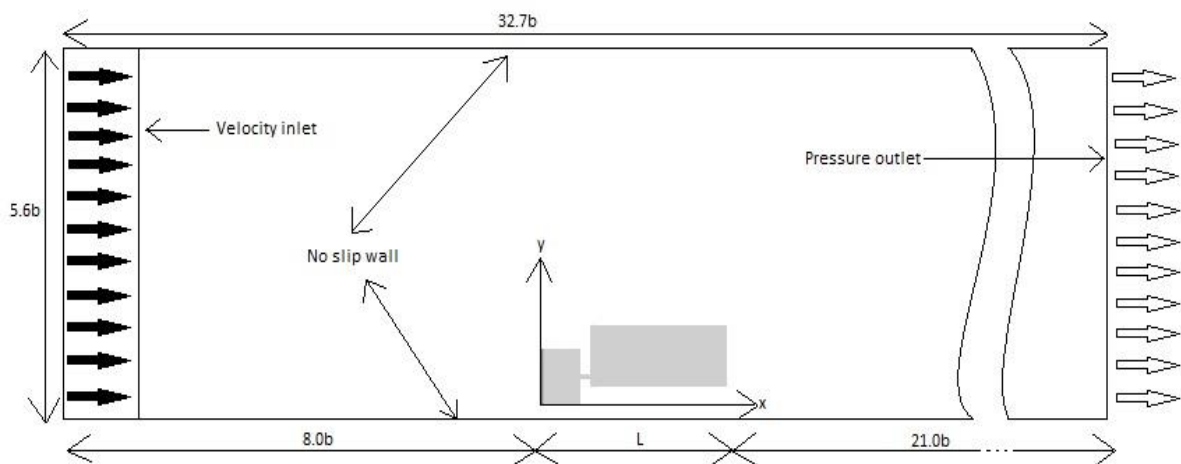
Figure 5.1: Computational domain with a generic truck - Side view.
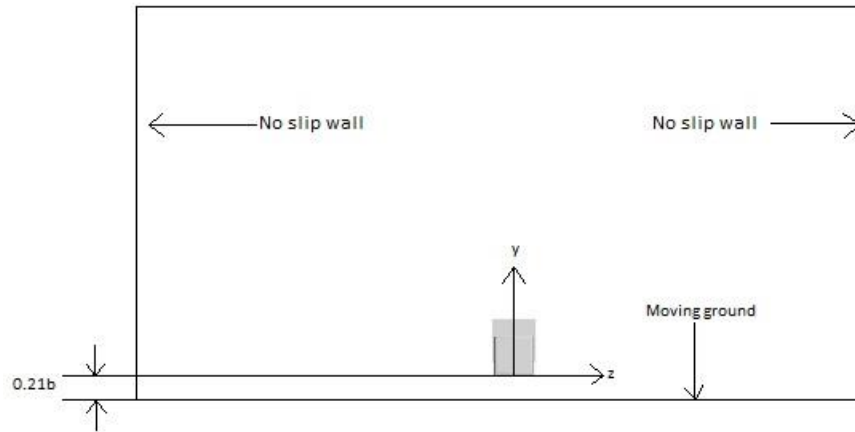
Figure 5.2: Computational domain - Front view.

A constant velocity of 24.4m/s is specified at the inlet, which matches the value used in the experiments and a pressure outlet boundary condition is used at the outflow boundary. A no-slip wall boundary condition is applied to the top and side walls. On the lower wall the velocity component in the streamwise direction is set equal to the inlet velocity, matching the moving ground condition in the experiment. The boundary conditions applied to the computational domain are exactly the same as the ones used in experiments by J.W Allan (Allan, 1981) and in the LES simulations by J. Osth and S. Krajnovic (Osth & Krajnovic, 2012). There is no information available from the experiments for work out the inlet turbulence intensity and hence a representative low turbulence wind tunnel value of 0.1% has been used in the present study.

5.3 Description of the Model

Allan (Allan, 1981) first investigated the model in a wind tunnel of the Southampton University. The Reynold number of the model is 0.51×10^6 based on the inlet velocity and the height of the trailer (b). The model consists of two bluff bodies in a tandem arrangement. The front bluff body represents the tractor and the rear bluff body represents the trailer. Allan experimented two different models. The first model is the tractor with sharp leading edge as seen in Figure 5.3 below and the second model is a tractor with curved leading edge. The experiments were also performed at various tractor trailer gap ratios. In the present study the second model, a tractor with curved leading edge, has been considered. This model has a low drag coefficient for a reasonably smaller tractor trailer gap ratio. The numerical simulations in the present study are carried out at a gap ratio of 0.17b.

The dimensions of the test case are given in Figure 5.3. The dimensions of the tractor considered for the numerical simulation has a height and width of 0.92b with length 0.67b. Since the front edges of the tractor are curved at a radius of 0.08b, the overall length of the tractor extends to 0.79b. The length of the trailer is 2.5b and the height and width are equal to b. The tractor is kept at 0.21b above the ground and the trailer is kept at 0.5b from above the ground (b = 0.305m)
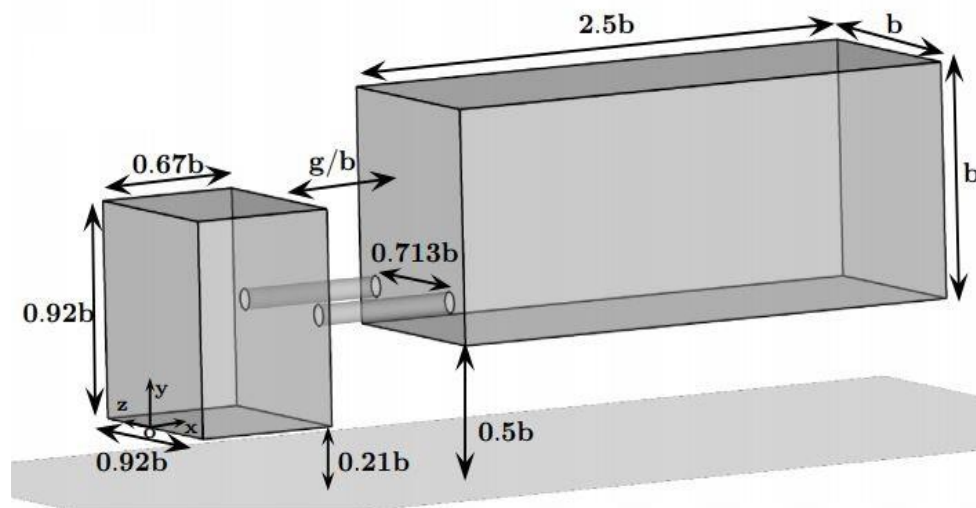
Figure 5.3: Schematic of generic test case (Osth & Krajnovic, 2012).

5.4 Mesh Independency Study

A grid independency study has been carried out first to ensure that the numerical results are independent of the mesh size without wasting computational resources. Two types of computational grids, polyhedral and trimmed meshes have been tested. The grids are generated using commercial CFD code Star CCM+. The coarse grid consists of 4.0 million cells, with medium grid consisting of 5.8 million cells and fine grid consisting of 8.1 million cells. It has been found that significant discrepancies exist when using polyhedral mesh while more consistent results have been obtained when using trimmed mesh. This is logic as trimmed mesh should provide an efficient and robust high-quality grid for simple geometries, which is the case in the present study. Therefore, trimmed mesh has been employed in the present study.

It is necessary to refine the mesh in the wake region to capture accurately very complex turbulent flow fields generated in this region due to flow separation and recirculation. An example of the refined mesh in the wake region is shown in Figure 5.4. This is achieved by using wake refinement and very slow volume growth rate for the entire computational domain.
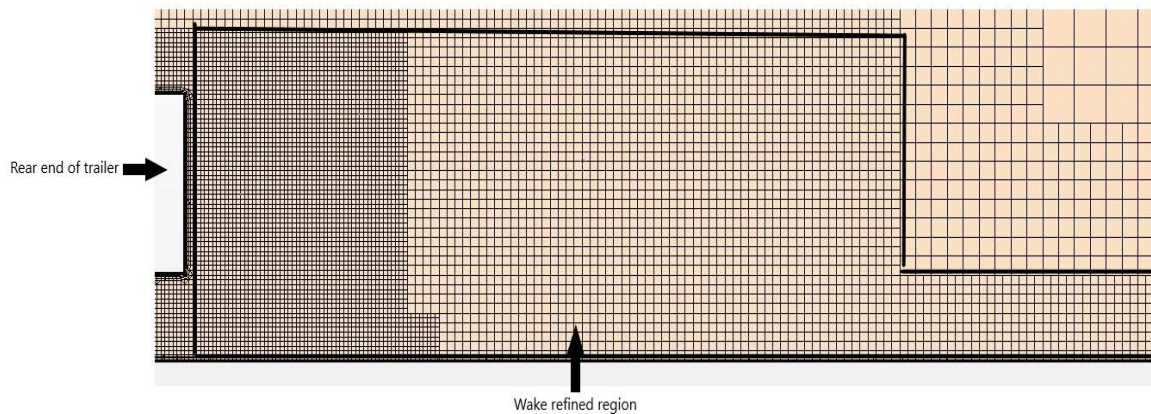
Figure 5.4: Trimmed cell mesh with wake refinement.

Volume growth rate controls the rate at which cell size increases from one cell to another and examples of volume growth rate with medium and slow are shown in Figure 5.5 and Figure 5.6. The cell growth rate defines the transition of the cell size by specifying minimum number of cell layers of each size. A faster growth rate increases the cell size immediately and slower growth rate employs multiple cell layers to provide a gradual transition (Star CCM+, 2020).

Medium Growth Rate (2 Layers per Cell Size)
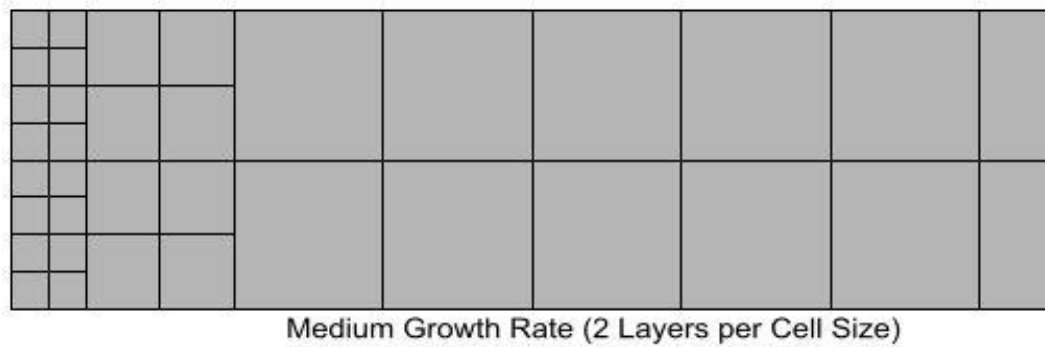
Figure 5.5: Medium growth rate (Star CCM+, 2020).

Slow Growth Rate (4 Layers per Cell Size)
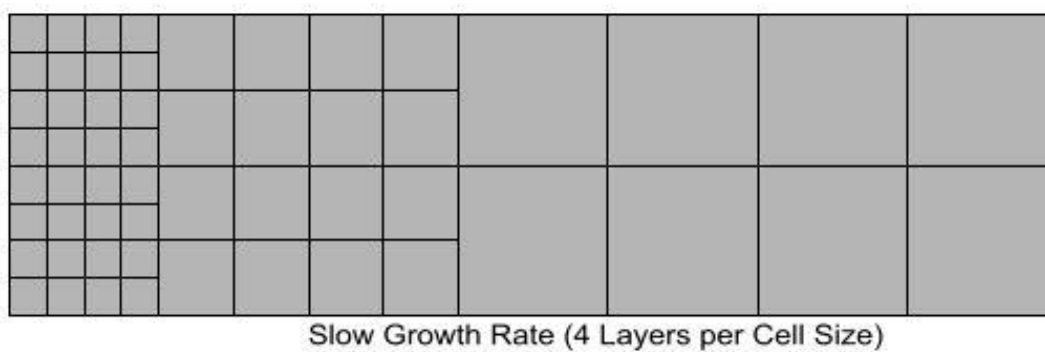
Figure 5.6:Slow growth rate (Star CCM+, 2020).

It is also important to ensure a good near wall mesh resolution and to achieve this, the number of prism layers used in the present study is kept at 10 with a prism layer thickness at 10% of the base size. The maximum prism layer stretching was kept at 1.3. For the coarse grid the nearest wall y+ is from 3< y+ <28.3, for the medium grid it ranges from 1.28< y+ <25.73 and for the fine grid the y+ values ranged from 0.16< y+ <22.6.

A volumetric control can be used to achieve the required mesh resolution at specific zones of the computational domain. As shown in Figure 5.7, volumetric control 1 is used to generate a fine mesh in the gap region to capture accurately the complex flow features in the gap. Volumetric control 2 is applied to a region around the truck wake region and volumetric control 3 is applied to the flow field around the truck, as shown in Figure 5.7.
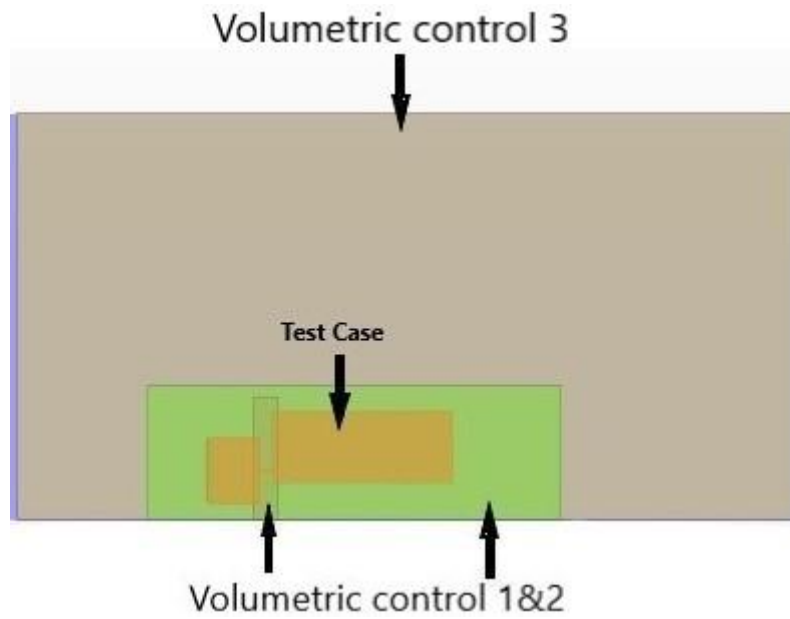
Figure 5.7: Section of computational domain showing three volumetric control around the test case.

5.5 Results
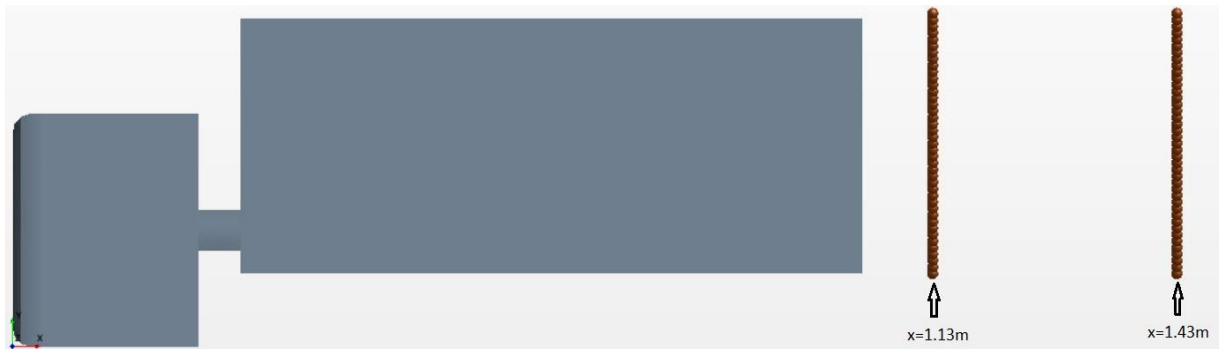
Figure 5.8: Location at which velocity profile is plotted.
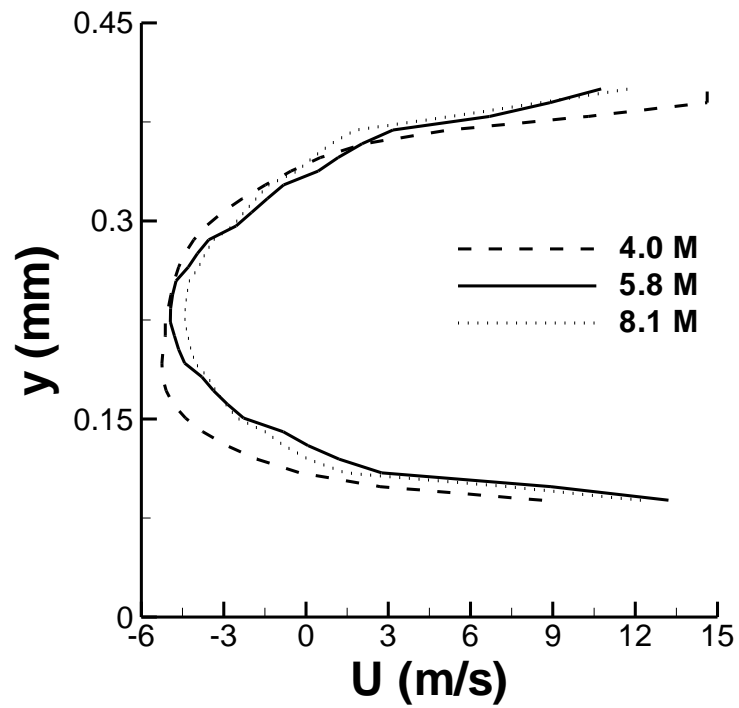
Figure 5.9:Velocity profile obtained using three meshes at x= 1.13m.
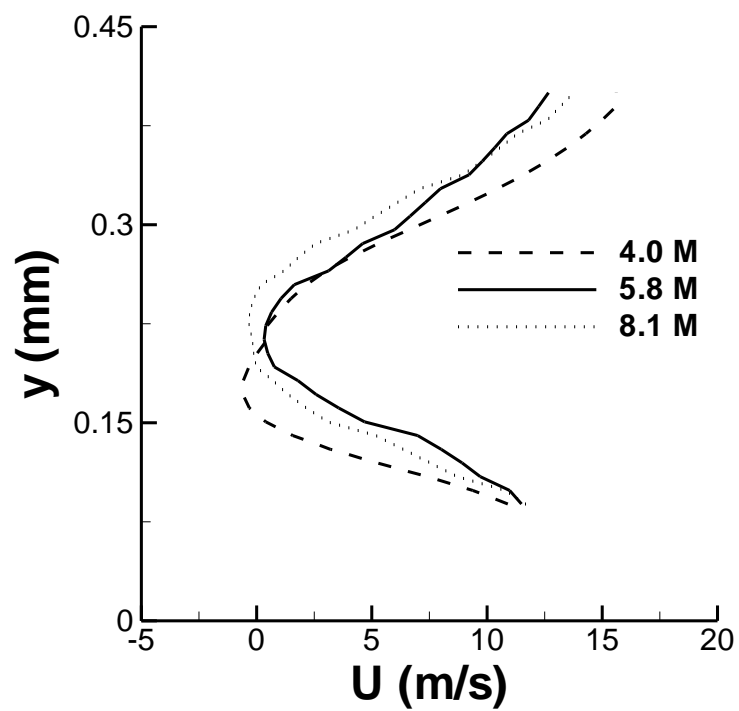
Figure 5.10: Velocity profile obtained using three meshes at x= 1.43m.

Figure 5.8 shows the locations behind the truck at which the velocity profiles are plotted along the vertical direction. The location for plotting the velocity profile are determined based on the flow attachment and vortex formation in the wake region of the trailer. The points are located at x=1.13m and x = 1.43m from the point of origin. The origin is on the front face at the base of the truck marked in 'o' as shown in Figure 5.3. Figure 5.9 and Figure 5.10 show the predicted axial velocity profiles along a vertical line as shown in Figure 5.8 on the centre spanwise plane (z=0) behind the truck. It can be seen from the figures that the results obtained using the coarse mesh are different from those obtained using the medium and fine meshes. However, the results obtained using the medium mesh are close to those obtained using the fine mesh, suggesting that the grid independent results have been achieved. Hence there is no need to refine the mesh further and the medium mesh has been used in the present study, with the nearest wall y+ value being kept close to 1 in order to avoid using wall function.

	C_d	ΔC_d
Experiment (Allan, 1981)	0.77	
Realizable k -e	0.862	11.95%
SST k-w	0.809	5.06%
RSM	0.820	6.49%

Table 5.1: Predicted drag coefficient compared to experimental result.

Choosing an appropriate turbulence model is always difficult as there is not a recognized best turbulence model since their performances vary depending on the flow situations. In the present study three well regarded and widely used turbulence models have been assessed and Table 5.1 shows the drag coefficient obtained from those turbulence model and the experimental data (Allan, 1981). SST k-ω model produces the best results in this flow situation and hence it has been selected in the present study.
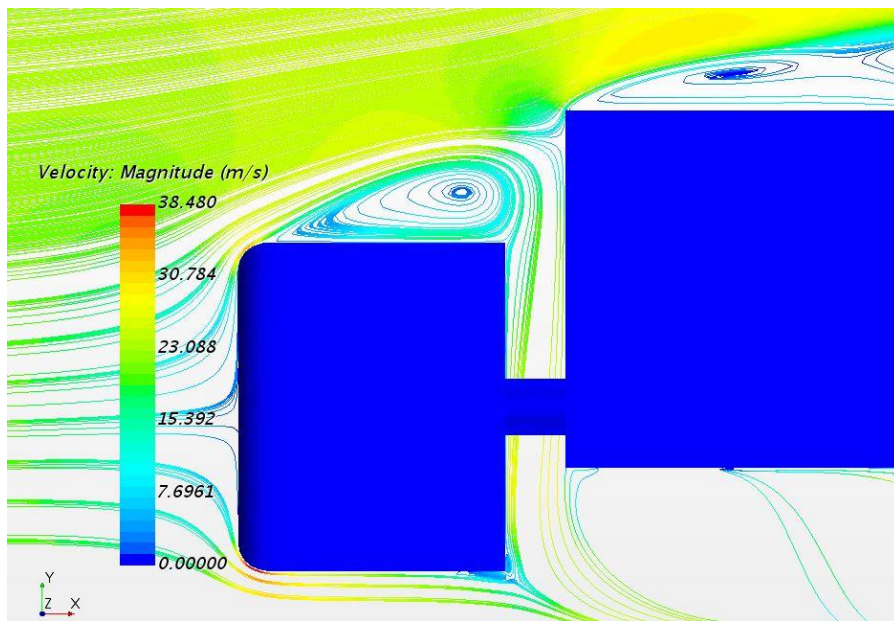
(a)
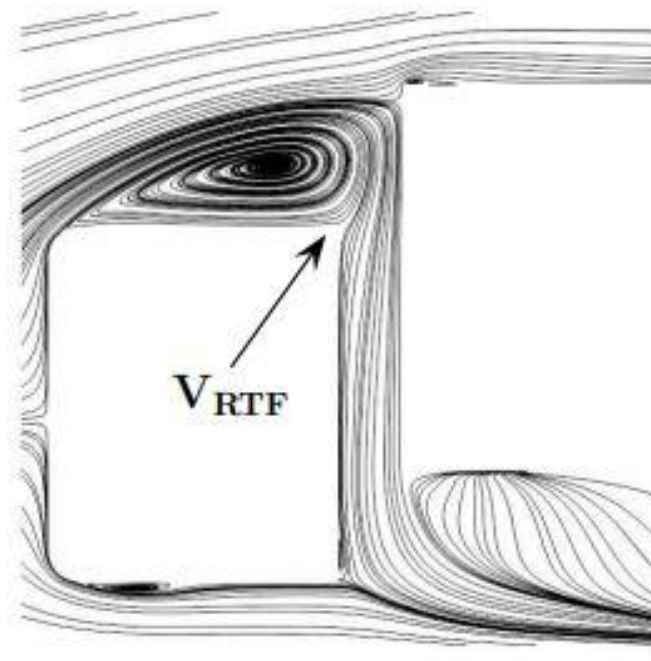
(b)

Figure 5.11: Comparison of streamlines showing one large recirculation region on top surface of the tractor. (a) Steady state numerical simulation, (b) LES simulation (Osth & Krajnovic, 2012)
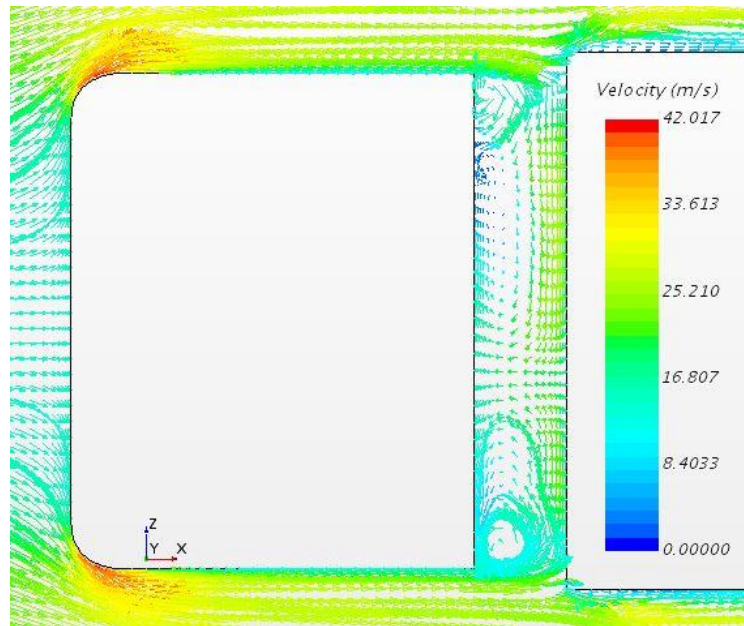
Figure 5.12: Velocity contour in the gap on the XZ plane at y = 0.20 m

Figure 5.11a presents the predicted streamlines on the XY plane located halfway in the spanwise direction and Figure 5.11b show the streamlines obtained from a previous LES simulations. The predicted flow field is reasonably similar to the LES prediction, especially the predicted separation bubble on top of the tractor is very well captured in terms of the shape and size. However, the current prediction shows a reasonably large recirculation region on top of the trailer whereas the previous LES prediction only shows a tiny recirculation region, and also that a small separation bubble is observable at the tractor bottom surface but the current prediction does not capture this small bubble. The separation bubble at the top of the trailer is due to the mesh resolution is lower which is employed for the steady RANS approach in this research in comparison to the LES results which requires a higher grid density. Another possibility could be due to the unsteady nature which cannot be captured by steady RANS approach. Hence only one instance has been predicted.

Figure 5.12 shows velocity contours on a XZ plane and two large vortices form at the two corners of the gap and complex flow field exists inside the gap. In addition, there is no flow separation at the leading edges on the lateral sides of the tractor, which could be due to the curved edges of the tractor front face. The gap experiences a flow field which constantly changes with time, however only one instance could be captured using the Steady RANS approach employed in this research.

5.5.1 Pressure Coefficient
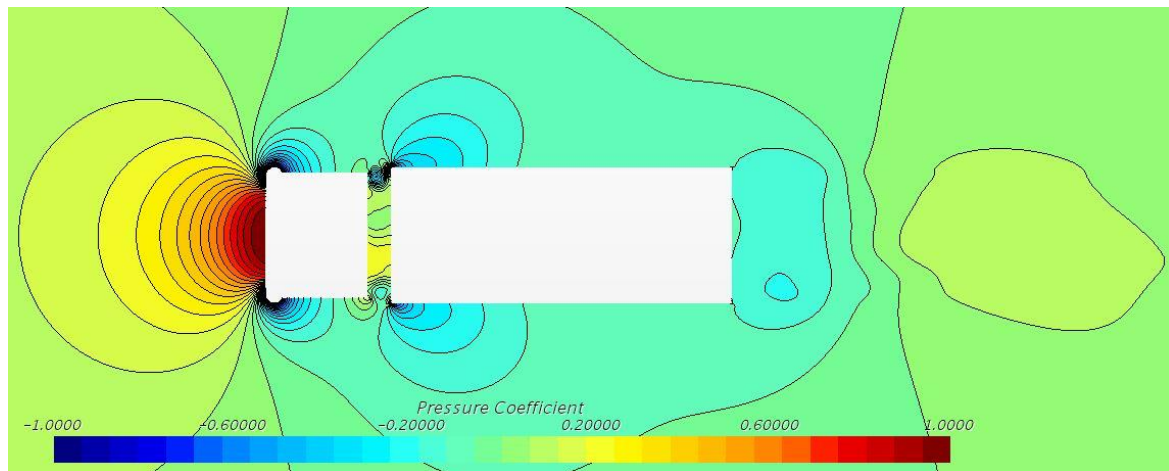
Figure 5.13: Distribution of Pressure coefficient on the horizontal plane at y=0.2m.
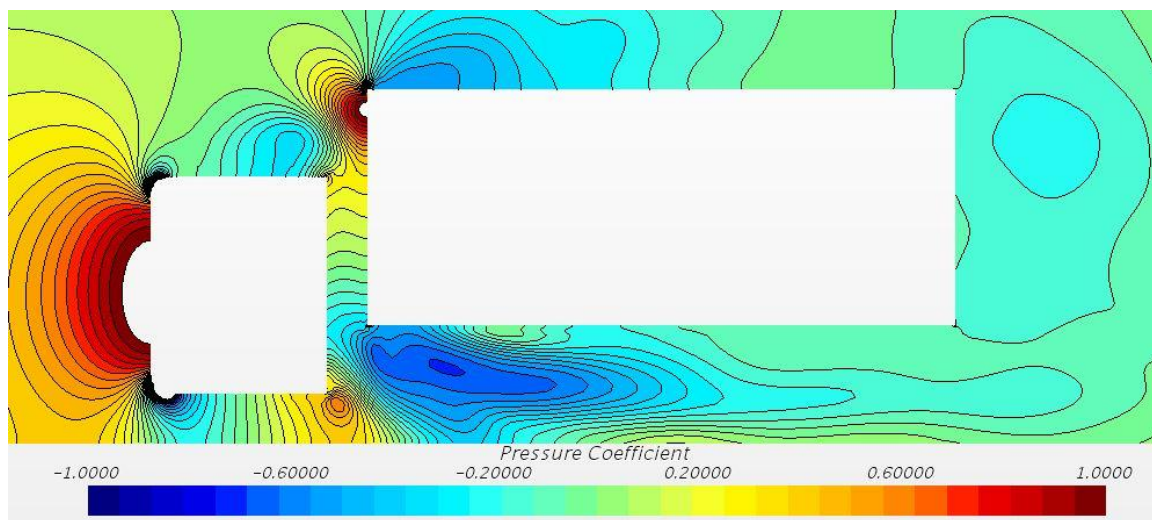
Figure 5.14: Distribution of Pressure coefficient on the XY plane located halfway in the spanwise direction at z=0m.

For a bluff body, the drag is mainly due to pressure distribution around the body, i.e., high pressure on the front surface and low pressure at the back surface, rather than the skin friction force on the body surface. Figure 5.13 presents contours of pressure coefficient on a XZ plane and there is a pressure region in front of the tractor and a low-pressure region behind the trailer (wake region). Overall the level of pressure contours change smoothly and symmetric apart from the front corners of the tractor and in the gap region where pressure change more rapidly due to the rapid change of flow fields in those areas, especially inside the gap with vortices and turbulence generated.

Contour of pressure coefficient on the XY plane located halfway in the spanwise direction is shown in Figure 5.14. It can be seen that there are more pressure variations on the XY

plane than the XZ plane, apart from the usual high pressure region in the front of the tractor and low pressure region behind the trailer, there is a large low pressure region below the trailer and just behind the gap, indicating that the flow is accelerated in this region. Furthermore, there is a small high-pressure region on the top part of the trailer front face due to the flow impingement on it. Pressure changes rapidly in the gap due to the complex turbulent flow field there as discussed above.
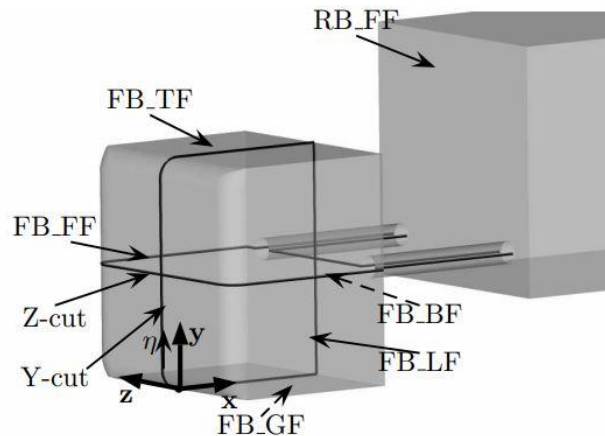
Figure 5.15: Notation of faces and the vertical and horizontal cut of the tractor are denoted by Y-cut and z-cut (Osth & Krajnovic, 2012).
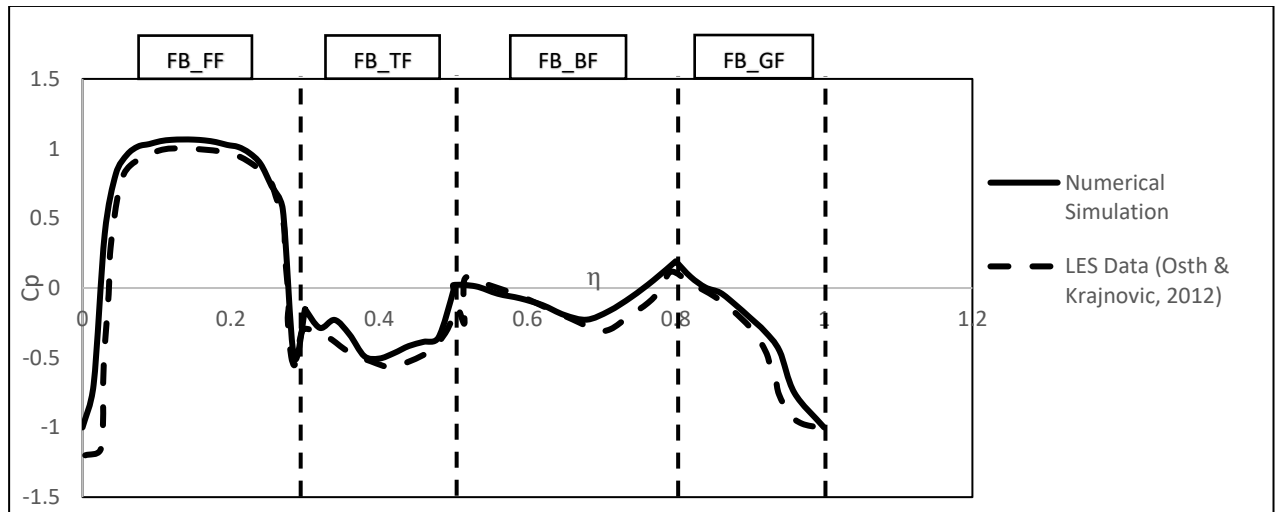
Figure 5.16: Time averaged pressure coefficient plotted from the origin in the clockwise direction along the tractor centre plane as shown in figure 5.15. The vertical dash lines indicate the end of each face and beginning of the next face.

Figure 5.15 shows the notations used to describe various face of the tractor and locations where pressure coefficient is plotted. FB denoted front box and RB denotes rear box. The various faces are denoted as FF -Front face, TF – Top face, BF – Back face and GF – Ground face. Figure 5.16 presents comparison between the predicted pressure coefficient and the

previous LES results (Osth & Krajnovic, 2012). It can be seen that a very good agreement with minor discrepancies between the current predicted results and the previous LES results, which strongly indicate that the current RANS approach employing the SST k-ω model with good mesh resolutions in important flow regions can produce accurate results. The minor discrepancies are due to the steady state time averaged simulations which require only a lower mesh resolution.

Summary

Steady state numerical simulations for flow around a generic truck mode without any drag reduction devices have been carried out using the RANS approach. The numerical results are validated against experimental data and previous LES results. Three widely used turbulence models have been tested and detailed analysis of the flow field has been performed. The main findings are:

- Among the three turbulence models tested, the SST $k - \omega$ model performs best in terms of the drag coefficient prediction and hence has chosen as the turbulence model in the present study.

- Current flow visualization clearly shows several important flow features: a big separation vortex on top of the tractor, another separation vortex on top of the trailer and two distinct lateral vortices on either side of the gap. Those two vortices are formed due to the inward turning flow from the lateral sides of the tractor. A complicated turbulent flow field is generated within the gap due to the strong interaction of those two lateral vortices with the flow entering from the top of the truck.

- Pressure contours plotted on a vertical and a horizontal plane show, as expected, a high pressure region in front of the tractor and a low pressure region behind the trailer, indicating that the drag is mainly due to such a pressure difference in the current case. In addition, it also shows that pressure changes more rapidly in the gap confirming that a complication turbulent flow field pressure changes more rapidly in the gap confirming that a complicated turbulent flow field exists as shown by the flow visualization. One more interesting point worth noting is that there is a reasonably large low-pressure region below the trailer and just behind the gap, indicating that the flow is accelerated in this region.

Chapter 6

Numerical Analysis of Flow in the Gap of a Simplified Tractor-Trailer Model with Several Drag Reducing Devices

6.1 Introduction

The aerodynamics of trucks is an area in which better understanding, and improvements can be made despite major achievements in the past years (Martini, 2016) (Browand & Hammache, 2004). There are several aerodynamic forces acting on a driving vehicle, which directly affect the operation of a vehicle. Aerodynamic loads on the vehicle may act in different ways but primarily result in drag being generated which affect the acceleration and velocity of a vehicle etc., and ultimately leading to fuel consumption efficiency.

Generally speaking, pressure drag makes up most of the total drag force experienced by a truck with the surface friction drag contributing to a miniscule amount of the overall drag. Pressure drag reduction of a truck can be achieved mainly in three areas: the front part of the tractor, rear part of the trailer and the gap between the tractor and trailer. The gap between the tractor and trailer has a significant effect on the total drag force and a better understanding of the flow field in the gap is needed for drag reduction in this region (Allan, 1981).

One simple, yet effective drag reduction device which has been used in the tractor and trailer gap is Cross Vortex Trap Device (CVTD) (Charles, et al., 2019). CVTD are equally spaced vertical slabs that extend perpendicular from the front face of the trailer. The primary aim of these devices is to trap vortices and stabilize the flow in the gap between the tractor and trailer. Kumar and Chaurasia (Kumar & Chaurasia, 2016) analyzed a similar CVTD design along with Coanda device mounted to the leading-edge corners of the trailer in the gap. Analysis carried out without any devices in the gap showed a combination of uneven high and low-pressure contours in the gap between tractor and trailer. When the model was tested with CVTD installed, pressure contours on the front face of the trailer had a better and even pressure distribution which was primarily due to vortices being stabilized by the use of CVTD (Charles, et al., 2019).

Despite that a significant amount of drag is generated in the tractor and trailer gap region the research on the drag reduction in the gap region is scarce in the literature. The present work investigates the effectiveness of a three CVTD configurations using a simplified tractor-trailer model (Osth & Krajnovic, 2012) as shown in Figure 6.1. The model consists of a front box which represents the tractor and a rear box representing trailer and is connected by two cylinders. The model dimensions are the same one used in the experiment (Allan, 1981) and the Reynolds number based on inlet velocity and height of the trailer box is $Re =$

0.51×10^6. The oncoming free stream velocity is at $0°$ yaw angle, which is in no crosswind condition.

The present study focuses on analysing several different drag reduction devices which are mounted to a truck to alter the flow field within the gap region. The results presented in this chapter are part of the numerical simulations carried out on the generic test case with several drag reduction devices. The chapter is split into three sections depending on the aerodynamic devices fitted to the tractor and/or trailer.

Section 6.1

6.1.1 Drag Reduction Devices Mounted on the Tractor

The two most common and widely used aerodynamic devices on the tractor are the cab roof deflector and the cab extenders (Martini, 2016). Numerical simulations have been performed for six configurations, two baseline configurations and four configurations of different aerodynamic devices mounted to the tractor. The six configurations are shown in Table 6.1 and the devices mounted on the tractor are highlighted. Configurations A and D are baseline configurations for their respective tractor heights as shown in Figure 6.1. The simulations have been carried out at a small gap width of $g/b = 0.17$ (b = 0.305m). An in-depth flow field investigation has been carried out to understand the change in drag coefficient due to the change in flow field within the gap. The important aspect of the study is to understand how the flow field change within the gap affects the overall drag of the vehicle. The overall drag coefficient data for each configuration is given in Table 6.2 and it can be seen clearly that a drag reduction has been achieved by all devices as configurations B & C, E & F have a much lower drag coefficient compared with the baseline configurations A & D.
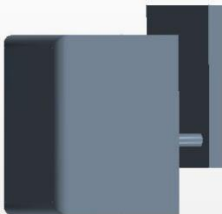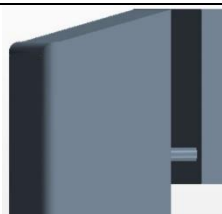
(a) Tractor A

(b) Tractor B

Figure 6.1:Two different tractor baseline configurations considered for this present research (a)Tractor height = 0.92b, (b)Tractor height = 1.105b.

	Configurations	Aero devices
T R A C T O R - A	Configuration A (Baseline)	
	Configuration B	
	Configuration C	 **(Top view)**
T R A C T O R - B	Configuration D (Baseline)	
	Configuration E	
	Configuration F	 **(Top view)**

Table 6.1: Six configurations (two baseline configurations, four configurations with drag reduction devices mounted on the tractor)

6.1.2 Predicted Drag Coefficient

Table 6.2 presents the predicted drag coefficients for the six cases in the present study. It can be seen that configurations A and D without aerodynamic devices mounted onto the tractor have the highest drag coefficients. Once aerodynamic devices are mounted onto the tractor (configurations B & C, D&E) an immense drop in overall drag coefficient of the truck is predicted. The relative difference (ΔC_d) presented in Table 6.2 are compared with the baseline cases i.e. configurations A and D for tractors A and B in Table 6.1. The predicted drag reduction for configurations B & C is 34% and 38.68% compared against the baseline configuration A, and the predicted drag reduction for configurations E & F is 12.84% and 17.87% compared against the baseline configuration D. Browand et al. (Browand & Hammache, 2004) analysed flow over two tandem bluff bodies and concluded that when a high volume of flow enters the gap between the two tandem bluff bodies then the drag coefficient of the downstream body can increase significantly. The present predictions are consistent with the finding by Browand et al. (Browand & Hammache, 2004) as the amount of flow entering the gap is significantly reduced for the baseline configuration A when the cab roof deflector and cab side extenders are deployed, leading to larger drag reduction.

It is evident from the present predictions and previous studies (Browand & Hammache, 2004) (Havel, et al., 2001) that the amount of flow entering the gap has a big impact on the drag coefficient but it is not fully understood how the flow field is changed inside the gap, which leads to the pressure field change inside the gap and hence results in the drag change. Therefore, an in-depth flow field analysis around the tractor and in the gap between tractor and trailer will be carried out in the next section to understand the drag reduction mechanism.

Truck Configuration	Drag Coefficient	ΔC_d
Configuration A (Baseline)	0.809	
Configuration B	0.534	33.99%
Configuration C	0.496	38.68%
Configuration D (Baseline)	0.537	
Configuration E	0.468	12.84%
Configuration F	0.441	17.87%

Table 6.2: Predicted drag reduction achieved by each configuration compared to baseline casses.

6.1.3 Analysis of Flow Field

The time averaged flow field analysis for the flow in the gap are presented in this section for the six configurations. Figure 6.2 presents the velocity contours coloured by the velocity magnitude on the XY plane at Z = 0 for configurations A, B, D & E. The roof deflectors employed in this study are angled at 29° and 15.7^o for tractor models A and B (refer Table 6.1).

For configuration A (Figure 6.2a), numerical simulations have predicted a strong recirculation region on top surface of the tractor. A proportion of the flow above the tractor enters the gap region and the remaining flow passes the gap, moving on to the top surface of the trailer towards the trailing end of the truck. The flow entering the gap from the top moves towards the bottom of the gap and eventually goes out, mixing with the mainstream flow along the bottom of the trailer. Applying the roof deflector to configuration A eliminates the presence of this big recirculation region on the top surface of the tractor and also reduces the amount of flow entering the gap region significantly as shown in Figure 6.2b. As a result of significant reduction of flow entering the gap, which leads to reduced pressure on the front face of the trailer, nearly 34% drag reduction has been obtained for configuration B compared against configuration A.

Figure 6.2c shows velocity contours for configuration D which has an increased tractor height compared with configuration A. The flow field around configuration D is similar to that for configuration A. However, the amount of flow entering the gap is much lower for configuration D than that for configuration A, leading to a lower drag coefficient for configuration D. Figure 6.2d shows the flow field for Configuration E (applying a roof deflector to configuration D) and it can be seen that the recirculation region on the top surface

of the tractor disappears. In addition, the amount of flow entering the gap region is reduced and hence the drag coefficient decreases by 12.84% for configuration E compared against configuration D.
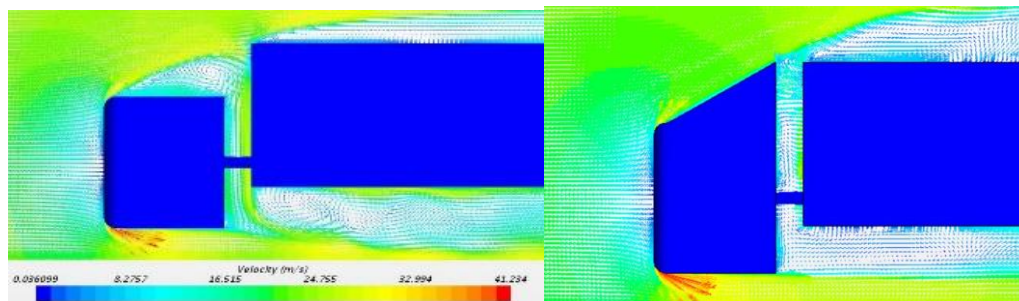
(a)   Configuration A.
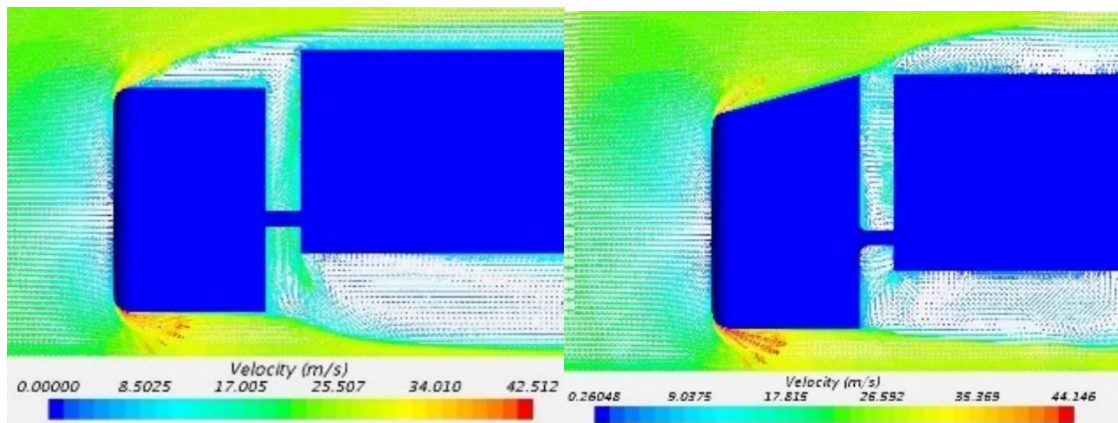
(b) Configuration B.

(c) Configuration D.

(d) Configuration E.

Figure 6.2:Velocity contours on the XY plane at Z=0.

A good understanding of the flow field within the gap is very important because the overall drag of a truck depends partly on pressure distribution within the gap, i.e., pressure distribution on the back of the tractor and front of the trailer. Typically, the flow field within the gap consists of two strong vortices formed due to inward turning flow along the lateral sides of the tractor and interacts with the downwash from the top of the tractor. Hence the flow field within the gap can be highly turbulent as shown in Figure 6.3 which presents velocity contours coloured by the velocity magnitude on the XZ plane at Y = 0.2m.

For the baseline configurations A and D without any drag reduction devices there is a strong interaction between the flow entering from top and the flow entering from lateral sides, resulting in a very turbulent flow field within the gap itself as shown in Figure 6.3a and

Figure 6.3d When the roof deflector is deployed (configurations B & E), the amount of flow entering from the top is significantly reduced, leading to much weaker downwash and the flow field inside the gap is mainly due to the interaction between the inward turning flow along the lateral sides of the tractor as shown in Figure 6.3 b & e. When the side extender is also deployed the interaction between the inward turning flow along the lateral sides of the tractor becomes weaker due to less amount of flow entering from the lateral sides, and hence the flow is less turbulent as shown in Figure 6.3c & f. This can be further confirmed from Figure 6.4 showing velocity contours coloured by the velocity magnitude on the YZ plane in the gap at X=0.026m from the rear face of the tractor and it is obvious that when both the roof deflector and side extender are deployed the flow is much less turbulent as both the velocity magnitude and the vorticity decrease significantly as shown in Figure 6.4b & d. This reductions in turbulence is due to the reduction in flow entering the gap region which can be observed in configurations B and E, the flow field within the gap region is dominated by inward turning flow entering from the lateral sides of the truck. However, when the side extenders are deployed, the flow field in the gap is dominated by inward turning flow from the top and lateral sides of the truck. Configuration F shows the least turbulence in the gap region.

It is evident from the above analysis that the drag reduction is due to two mechanisms: 1. when the drag reduction devices are deployed much less amount of flow entering the gap, resulting reduced pressure on the front of the trailer; 2. flow in the gap becomes much less turbulent, hence less energy being dissipated or lost, when the drag reduction devices are deployed.
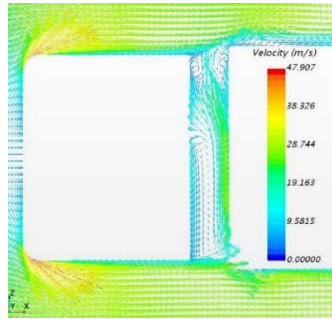
(a) Configuration A   (b) Configuration B   (c) Configuration C

(d) Configuration D   (e) Configuration E   (f) Configuration F.
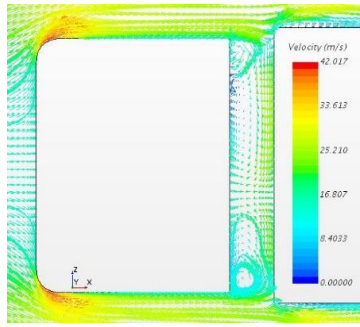
Figure 6.3:Velocity contours on the XZ plane at Y=0.20m.
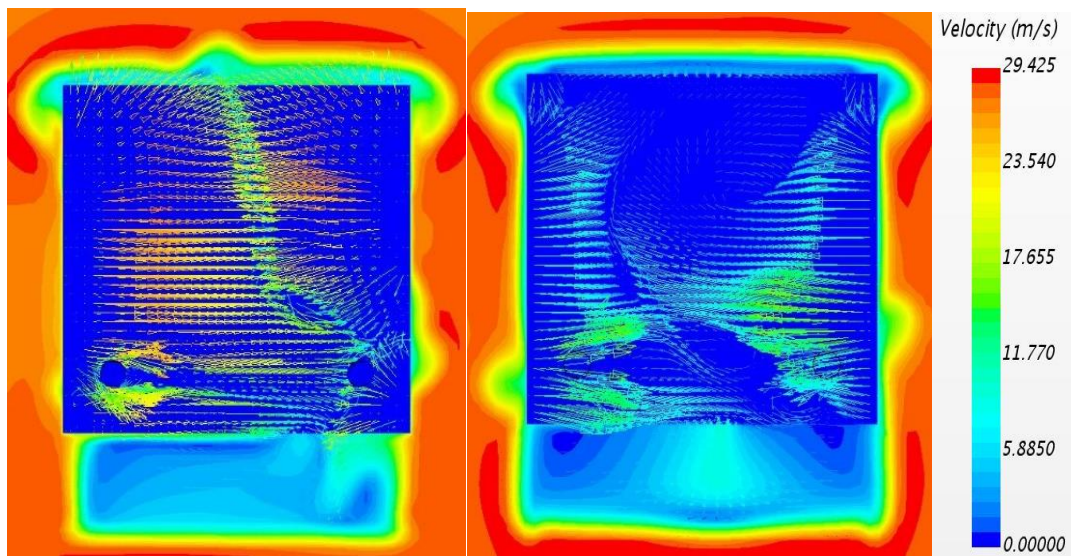
(a) Configuration B.

(b) Configuration C

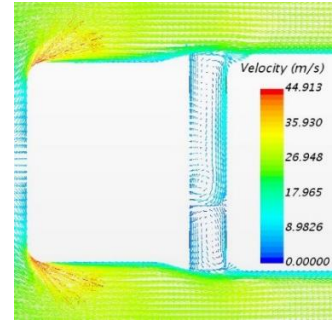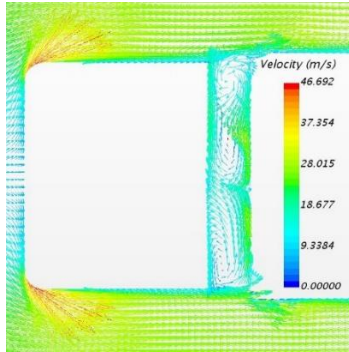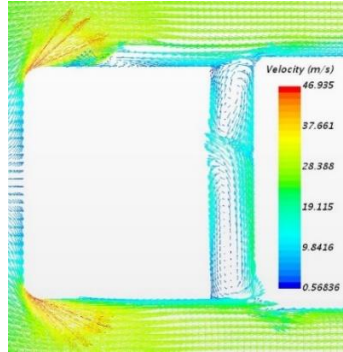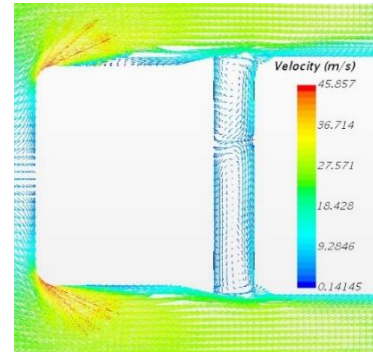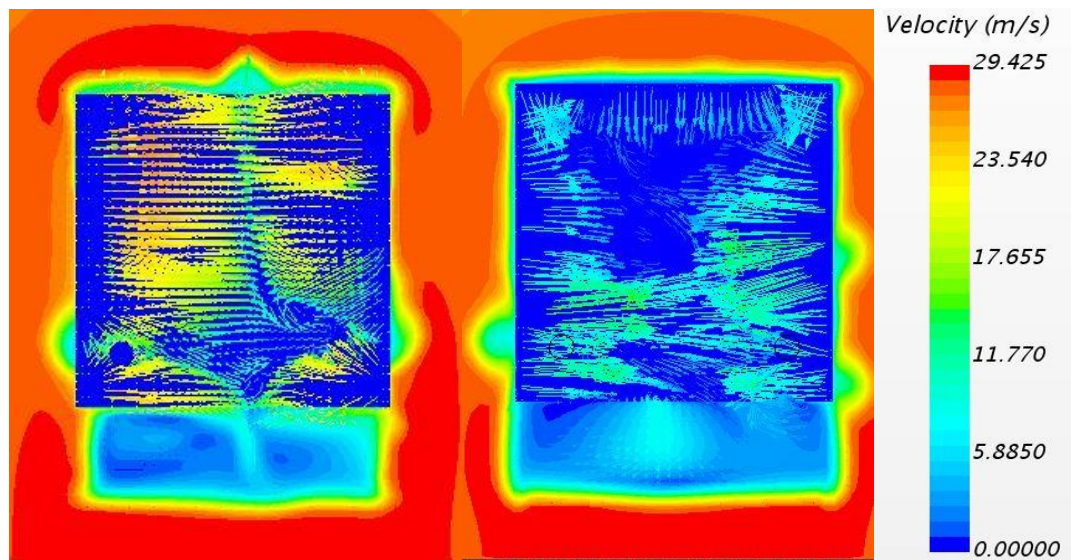

(c) Configuration E.

(d) Configuration F

Figure 6.4:Velocity contour on the YZ plane in the gap at X=0.026m looking from the rear face of the tractor.

6.1.4 Surface Pressure Distribution

Further analysis the mean surface pressure distributions is presented in this section and Figure 6.5 shows contours of pressure coefficient for configuration A. It can be seen that two high pressure regions are clearly observable on the forward-facing faces of the tractor and trailer, which is due to flow impingement directly on those two regions. It is interesting to note that a slightly asymmetric pressure field is observed on the forward-facing of the trailer even at zero-degree yaw angle as shown in Figure 6.5a. This could be due to the bi stable regime predicted in the gap region by (Havel, et al., 2001), which cannot be captured by the steady state numerical simulations used in the present study. At close spacing, the effect of the bi-stable regime on drag is very minimal and this regime cannot be predicted by RANS approach due to time averaging method.

(a) Isometric view   (b) XY Plane view.
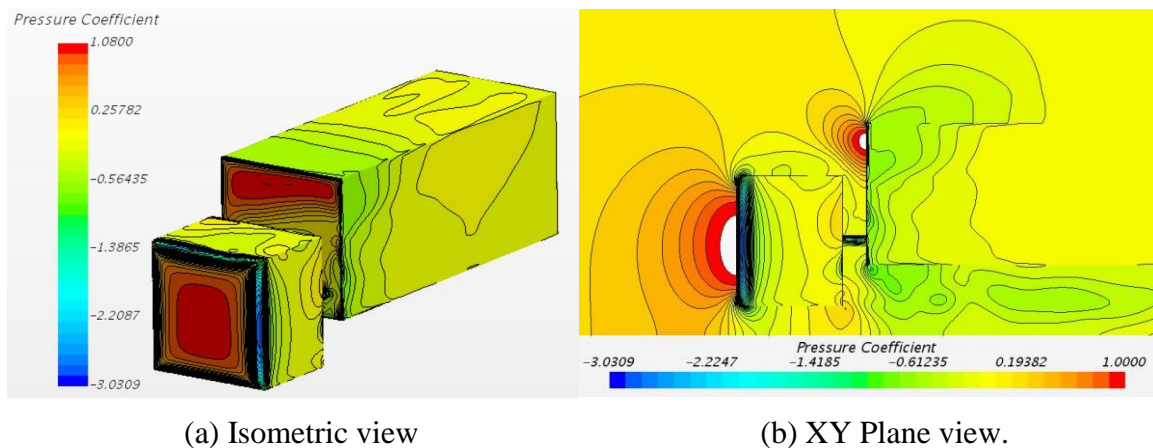
Figure 6.5:Pressure coefficient contours for configuration A.

For configuration B with a roof deflector deployed, the trailer front face experiences a reduction in pressure as the high pressure region on the front face of the trailer in configuration A has disappeared completely as shown in Figure 6.6, leading to a significant pressure drag reduction. This is because the flow impingement directly on the front face is eliminated by the roof deflector. Although the roof deflector causes a bigger recirculation region on top of the trailer as shown in Figure 6.6b the overall pressure drag will not be affected by this recirculation region. Figure 6.7 shows the pressure coefficient contours on the front face of the trailer in more detail and it can be seen that on most of face the pressure coefficient is quite low or negative apart from two very small high pressure regions near the lateral sides. This is because the width of the tractor is less than the width of the trailer which results in flow impingement on those two small regions on the front face of the trailer. due

to the nature of the flow captured at this instance by the steady RANS approach, an assymetric nature of the pressure contours is observed on the front face of the trailer.

| (a)Isometric view. | (b) XY plane. |

Figure 6.6: Pressure coefficient contours for configuration B
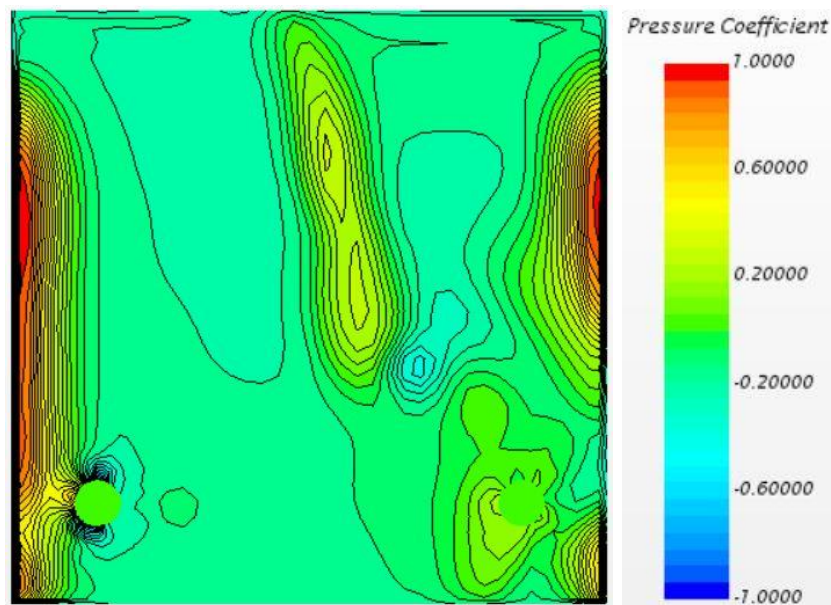
Figure 6.7:Pressure coefficient contours on the front face of the trailer for configuration B.

Figure 6.8 shows contours of pressure coefficients for configuration C which has the least drag compared with configurations A & B due to the use of both the roof deflector and side extenders on the top and lateral surfaces of the tractor. This is because the pressure on the front face of the trailer has been reduced further compared with configuration B due to the reduction in inward turning flow from the lateral sides of the tractor by the side extenders. In particular, the two small high pressure regions observed in Figure 6.7 for configuration B disappears as shown in Figure 6.9 since the flow impingement on those areas has been eliminated due to the use of the side extenders.
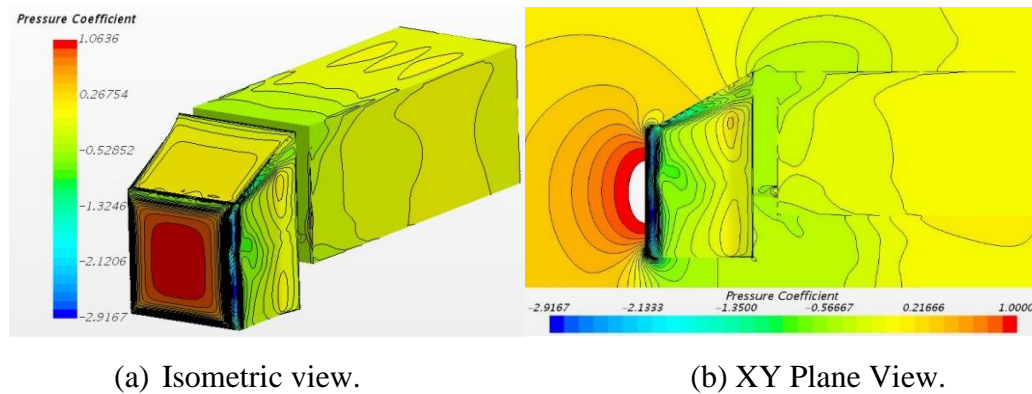
(a) Isometric view.   (b) XY Plane View.

Figure 6.8:Pressure coefficient contours for configuration C.
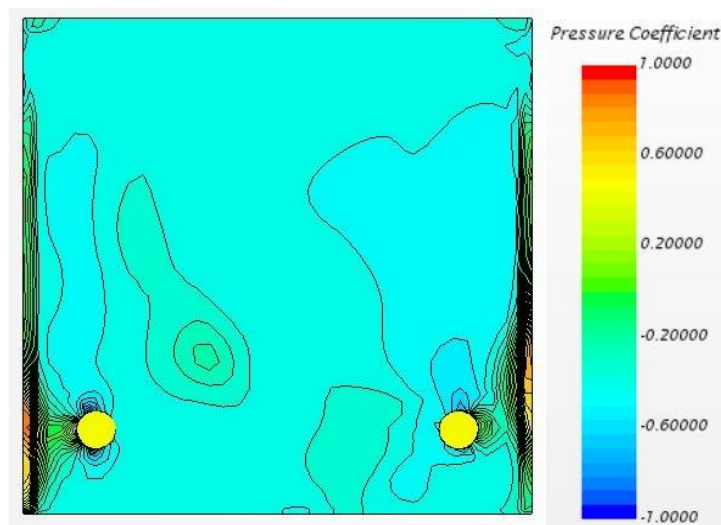
Figure 6.9:Pressure coefficient contours on the front face of trailer for configuration C.

The tractor height of Configuration D is larger than those of the previous configurations which leads to quite different pressure distribution on the front face of the trailer as shown in Figure 6.10. The size of the high pressure region in the upper part of the trailer's front face has drastically reduced as shown in Figure 6.10a. Naturally the high pressure region on the front face of the tractor has increased due to the increased height. However, the drag coefficient for configuration D is still much lower than the drag coefficient for configuration A since the high pressure region on the front face of the trailer is significantly reduced as a result of less flow entering the gap region. Another notable difference compared with Configuration A is that the recirculation region on top of the trailer is much smaller as shown in Figure 6.10b. From Figure 6.11, it can be seen the pressure contours are lot more symmetrical and more even. Two high pressure bubbles on the top of the trailer and a gradual reduction in pressure is predicted towards the centre of the trailers front face.

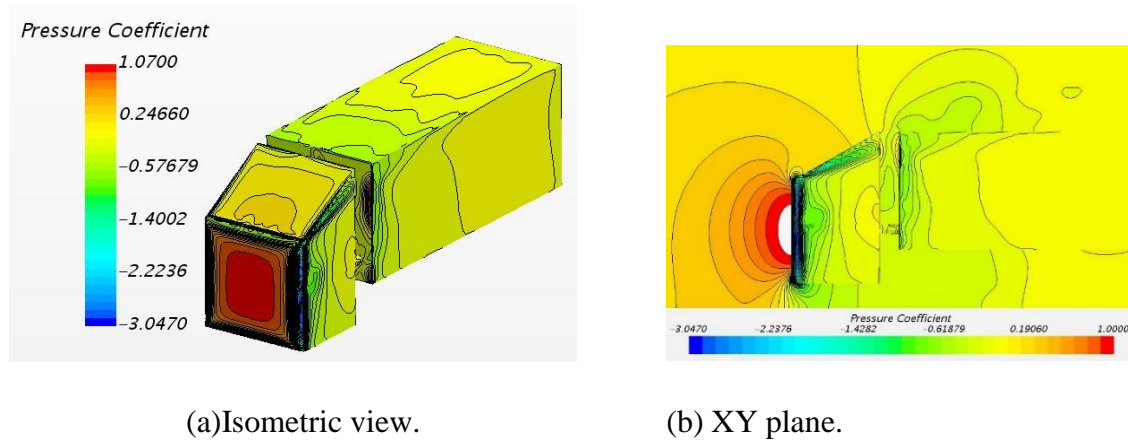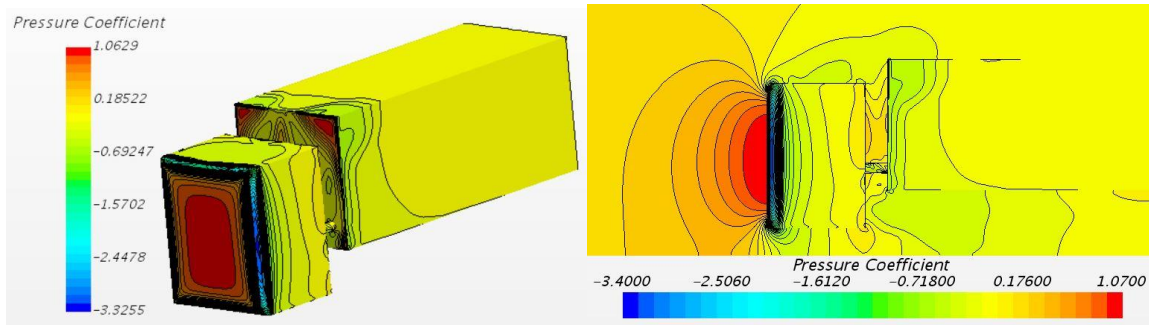(a)Isometric view.   (b) XY Plane View.

Figure 6.10:Pressure coefficient contours for configuration D.
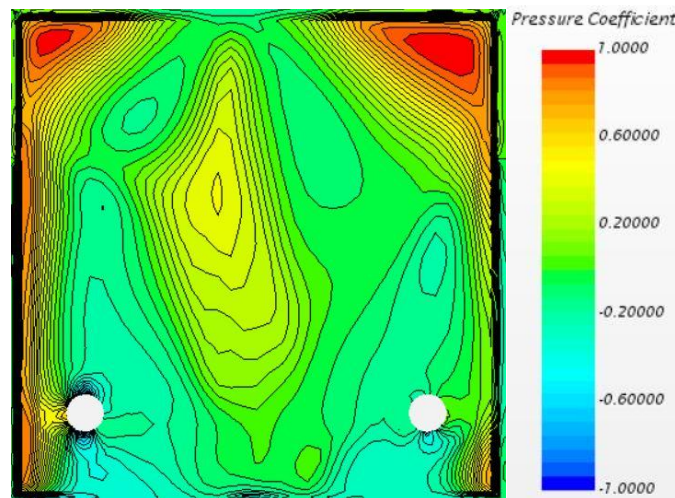
Figure 6.11: Pressure coefficient contours on the front face of trailer for configuration D.

For configuration E when a cab roof deflector is added to configuration D, similar to configuration B, the high pressure region on the front face of the trailer in configuration D is eliminated as shown in Figure 6.12, leading to a drag reduction of about 13%. Two small regions near the side edges of the front face of the trailer, similar to configuration B, can be observed in Figure 6.13 which shows detailed pressure distribution on the front face of the trailer. This is due to the flow impingement onto the front face of the trailer since the width of the tractor is less than the width of the trailer.

147

(a)Isometric View.   (b) XY Plane view.
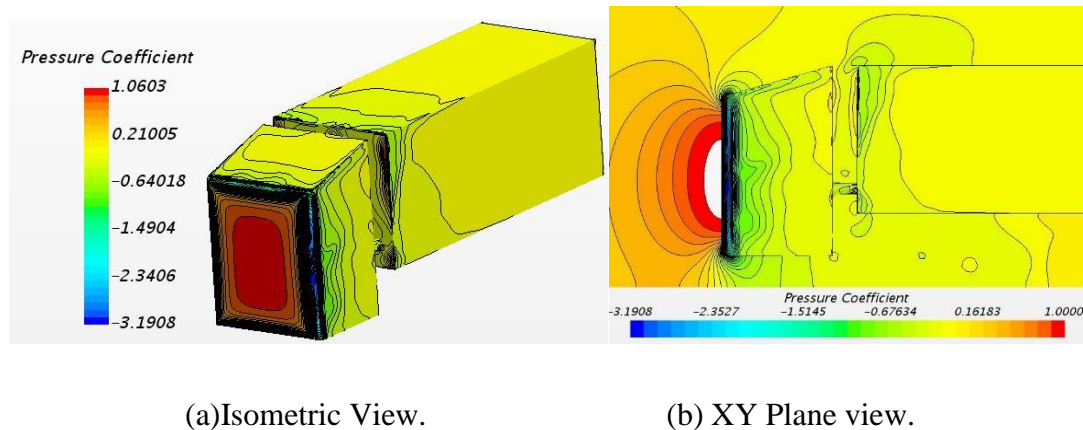
Figure 6.12: Pressure coefficient contours for configuration E.
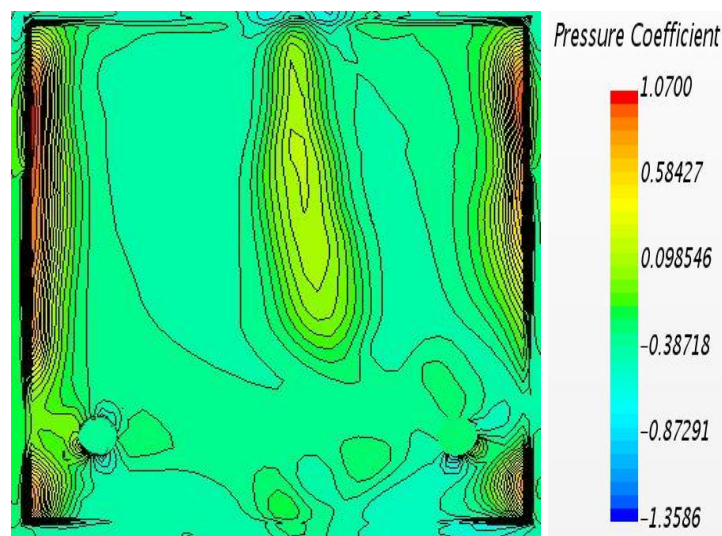
Figure 6.13:Pressure coefficient contours on the front face of trailer for configuration E.

Configuration F has the lowest drag coefficient among all the configurations due to the deployment of both roof deflector and the cab extenders along the lateral sides of the tractor on the baseline configuration D which has already a lower drag coefficient compared with the baseline configuration A. Figure 6.14 shows the pressure coefficient contours for configuration F and the detailed view of pressure coefficient contours on the front face of the trailer is presented in Figure 6.15. It can be seen clearly from Figure 6.15 that not only there is no high pressure region on the front face but also the pressure is lower than those of all other configurations. Furthermore, the pressure field is much smoother or quite uniform,

which confirms that the flow in the gap region is less turbulent as discussed above in analysis of flow field section.

(a)Isometric view   (b) XY Plane view.
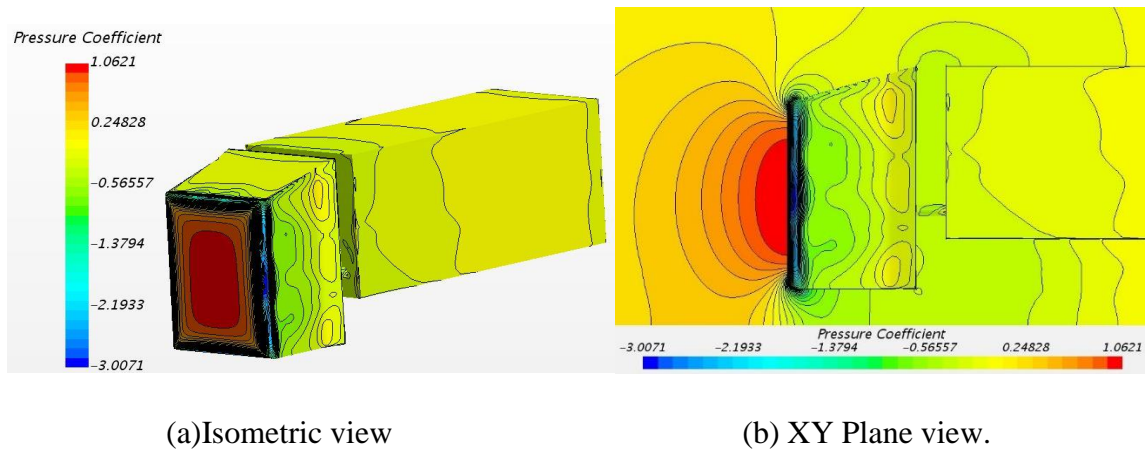
Figure 6.14: Pressure coefficient contours for configuration F.
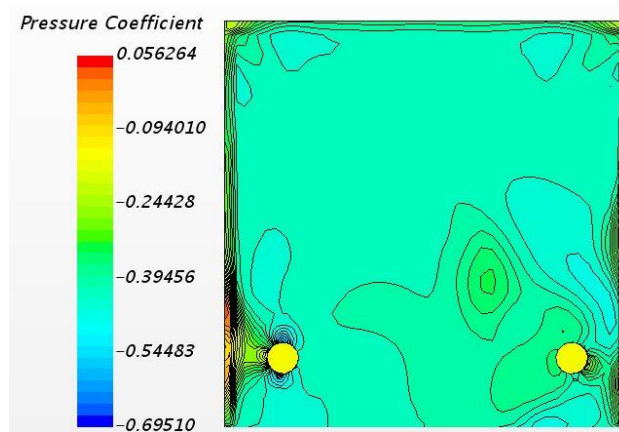
Figure 6.15: Pressure coefficient contours on the front face of trailer for configuration F.

Section 6.2

6.2.1 Drag Reduction Devices Mounted on the Trailer

It is understood that the drag generated in the gap region is due to the pressure on the front face of the trailer and this section will evaluate nine configurations with drag reduction devices mounted on the front face of the trailer (some of the configurations also with devices mounted on the tractor) as shown in Figure 6.16. Following on from the previous six configurations the configurations in this section are labelled from G to O. The first six configurations (G – L) have the same tractor height as the baseline configuration A and the other three configurations (M – O) have the same tractor height as the baseline configuration B.

There are many different kinds of drag reduction devices, the purpose of some devices is to trap the vortices within the gap and even out the pressure field on the front face of the trailer and other devices are used to reduce the level of inflow into the gap region while another kind of devices aim at guiding the flow to improve the flow field. The device investigated in the present study can be classified as "vortex trap device", more specifically it is the so-called Cross Vortex Trap Device (CVTD) apart from configuration O. The CVTD evaluated in the present study consists of one, two and three vertical slabs fitted to the front face of the trailer as shown in Figure 6.16.
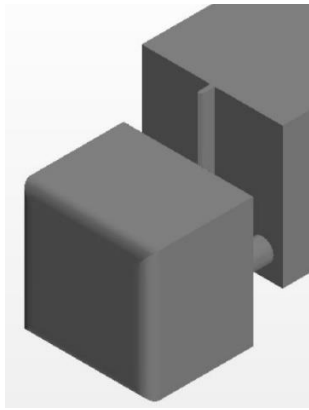
(a) Configuration G.   (b) configuration H.   (c) Configuration I.
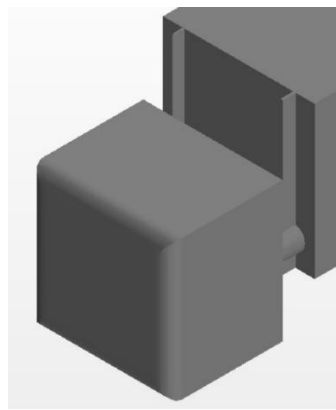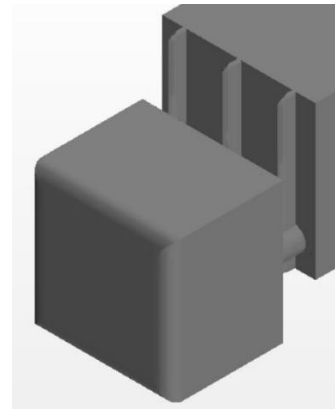
(d)Configuration J.   (e)Configuration K.   (f) Configuration L.

(g) Configuration M.   (h) Configuration N.   (i) Configuration O.

Figure 6.16: Nine configurations with drag reduction device mounted on
the front face of the trailer.

6.2.2 Predicted Drag Coefficient

Table 3 below presents the predicted drag coefficient for those nine configurations and the predicted drag coefficient for the baseline configuration A as a reference value. It can be seen from the table that different levels of drag reduction have been achieved for all configurations compared with the baseline configuration A, from the minimum drag reduction of 10% for configuration H to the maximum drag reduction of 47.58% for configuration N. More detailed analysis of flow field and pressure distribution will be presented in the following sections.

Truck Configurations	Drag Coefficient	ΔC_d
Configuration A (Generic case)	0.809	
Configuration G	0.723	10.60%
Configuration H	0.728	10%
Configuration I	0.690	14.70%
Configuration J	0.663	18.05%
Configuration K	0.487	39.80%
Configuration L	0.524	35.22%
Configuration M	0.521	35.60%
Configuration N	0.424	47.58%
Configuration O	0.439	45.73%

Table 6.3:Predicted drag coefficients

6.2.3 Analysis of Flow Field

Figure 6.17 shows velocity contours on the ZX plane at a height of y=0.20m for all nine configurations. It can be seen that very complicated flow fields are formed within the gap region for all cases, due to the strong interaction of different flow streams entering the gap from the top and inward turning from the sides, leading to turbulent flow with strong vortices which are clearly observable. For configurations G, H and I where no devices are mounted on the tractor and the differences are that one vertical slab is mounted on the front face of the trailer for configuration G, two and three slabs for configurations H and I. Hence the drag reduction can only be due to the change of flow field by the deployment of vertical slabs and it can be seen that the three slabs deployed in configuration I are more effective to reduce the drag since in this case it reduces more flow interactions, leading to the vortices trapped in different regions, and hence resulting in less turbulent flow in the gap region. This is consistent with the previous findings that the main function of CVTD is to trap the vortices within the gap and hence reduce the flow interaction, resulting in less turbulence.

For the six configurations (G – L) with the same tractor height, the maximum drag reduction is achieved for configuration K (39.8%) which has been installed with the triple vortex trap device (three vertical slabs) along with the roof deflector and tractor side extender. As discussed before that the roof deflector and tractor side extender are very effective in reducing the amount of flow entering the gap, eliminating the high pressure regions on the front face of the trailer and hence leading to a significant drag reduction. Addition of the triple vortex trap device on the front face of the trailer stabilises the vortices further and reduces the mixing of the flow within the gap, resulting in less turbulence and hence leading a further drag reduction. For the remaining three configurations (M – O) with a larger tractor height the maximum drag reduction is achieved for configuration N (47.58%) which has been installed with the triple vortex trap device along with the roof deflector and tractor side extender.

It is evident from the above discussion that among the three vortex trap devices (one vertical slab, two vertical slabs and three vertical slabs) the triple vortex trap device (three vertical slabs) mounted on the front face of the trailer proves to be the most efficient arrangement. It is interesting to note that a significant drag reduction is also achieved for configuration O which has not been installed with any CVTD on the front face of the trailer but the back face of the tractor and the front face of the trailer are curved, which means changing the design

153

of the tractor and trailer. This sounds a good idea theoretically but may not be practical and hence deployment of drag reduction devices is a better approach.
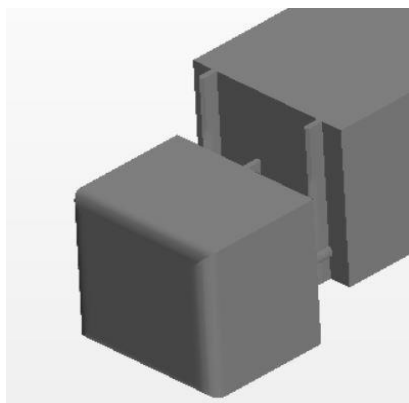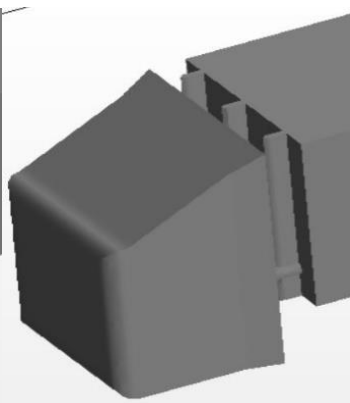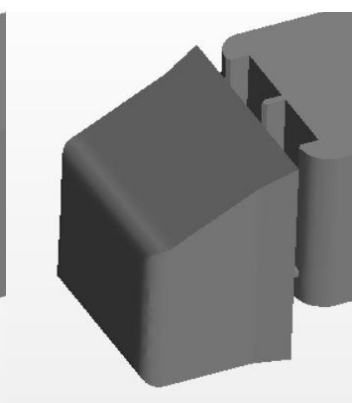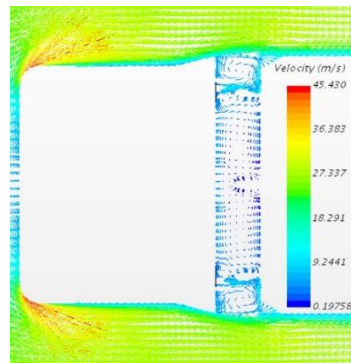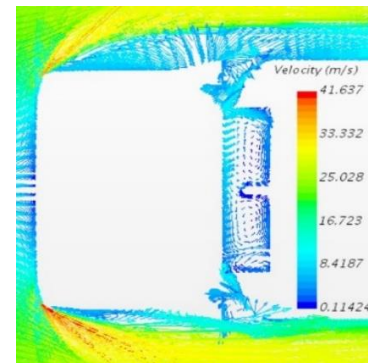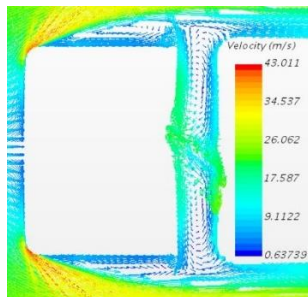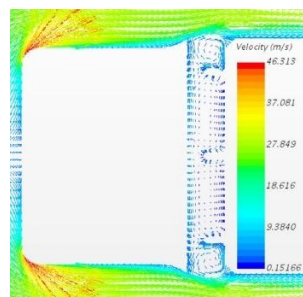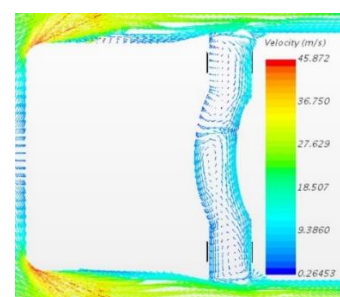

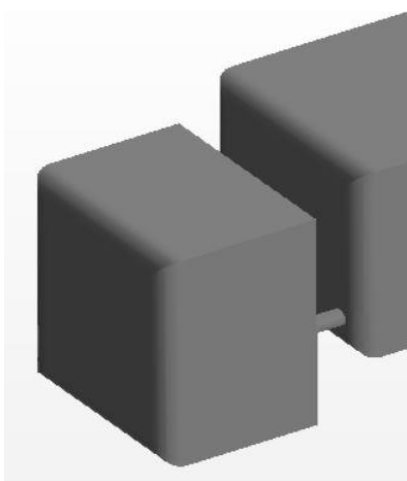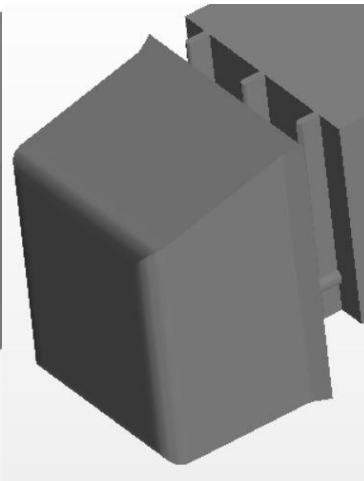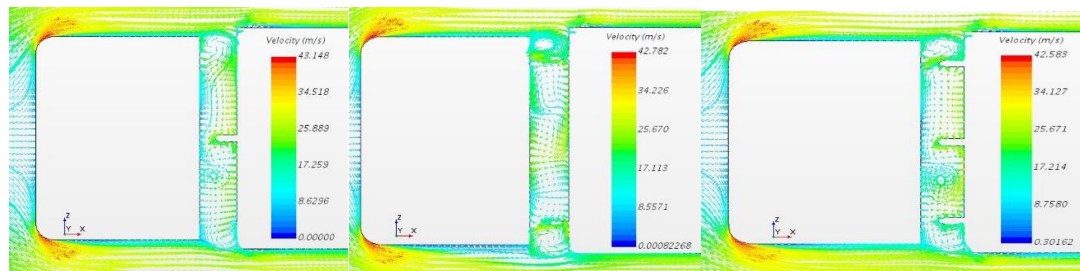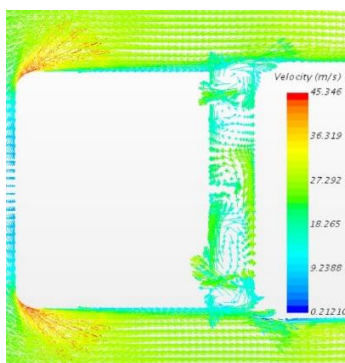| (a) Configuration G. | (b) Configuration H. | (c) Configuration I. |
| (d) Configuration J. | (e) Configuration K. | (f) Configuration L. |
| (g) Configuration M. | (h) Configuration N. | (i) Configuration O. |

Figure 6.17 :Velocity contours on the XZ plane at y=0.20m for all configurations.

Figure 6.18 shows the flow fields in the gap region on the YZ plane at x=0.026m from the rear face of the tractor (located in the middle of the gap) for the nine configurations and it can be seen that the flow fields vary significantly with the use of different devices. Figure 6.18a shows the flow field for configuration G with a single CVTD along the centre line of the truck and a strong inward turning flow is observable which mix in the gap region with the flow entering from the top, leading to high velocity flow exiting from the gap region towards the base of the truck. The flow field for configuration H with double CVTD is similar to that for configuration G although the inward turning flow from the sides are

154

slightly is reduced as shown Figure 6.18b and hence the drag reduction for those two configuration are more or less the same (10%). For configuration I with three CVTD it can be seen that the flow mixing in the gap is clearly reduced (vortices stabilised) as shown in Figure 6.18c, which ultimately results in reduced turbulence within the gap region and hence the drag reduction is larger (14.7%) compared with configurations G & H. The use of a roof deflector and tractor side extenders installed on the tractor for configurations K, L, N has significantly reduced the amount of flow entering the gap region plus the effect of three CVTD on reducing the flow mixing, the flow fields are very smooth (possibly laminar flow) as shown in Figure 6.18 e –h. Therefore, a significant drag reduction has been achieved for those configurations, especially for configuration N (47.58%). It is interesting to note that for configuration O without any CVTD on the front face of the trailer but the back face of the tractor and the front face of the trailer are curved, the velocity magnitude is also reduced with less mixing although the flow field is not as smooth as those for configurations K, L and N.
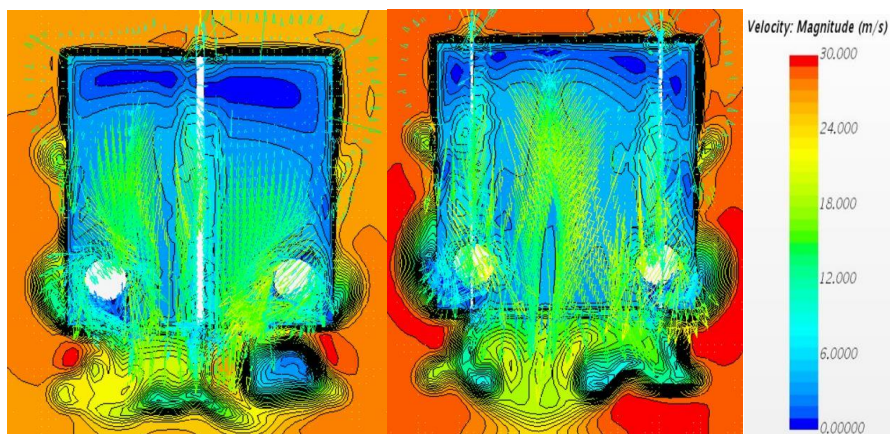
(a) Configuration G.   (b) Configuration H.
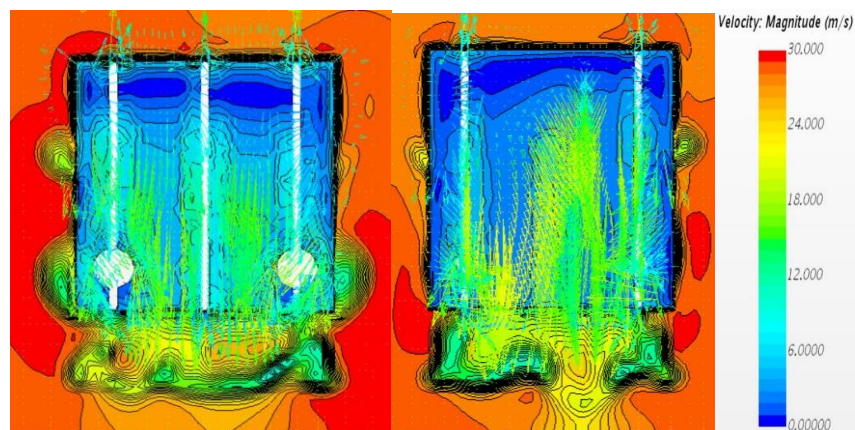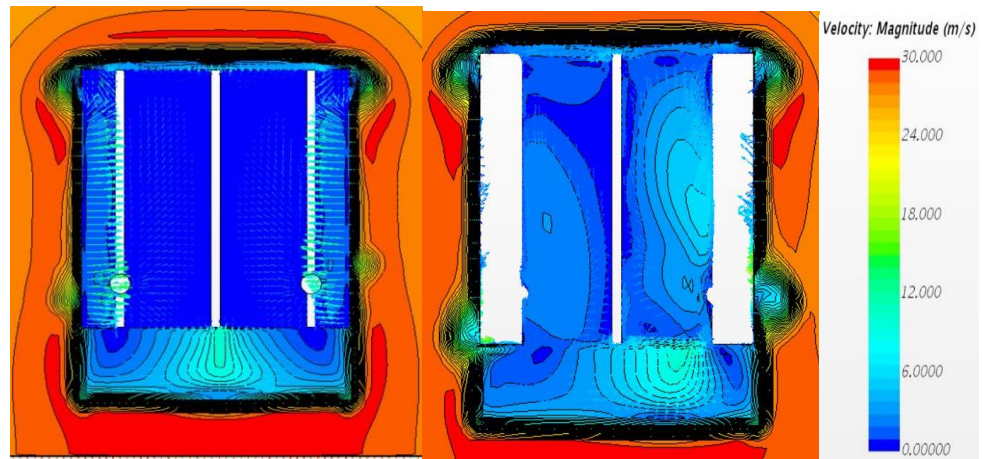
(c) Configuration I.   (d) Configuration J.

(e) Configuration K. (f) Configuration L
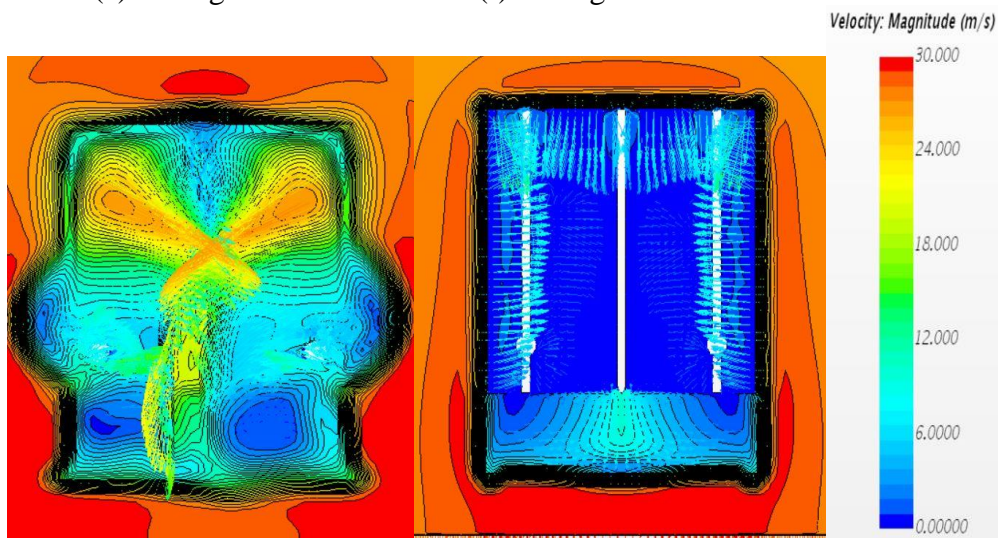
(g) Configuration M. (h) Configuration N
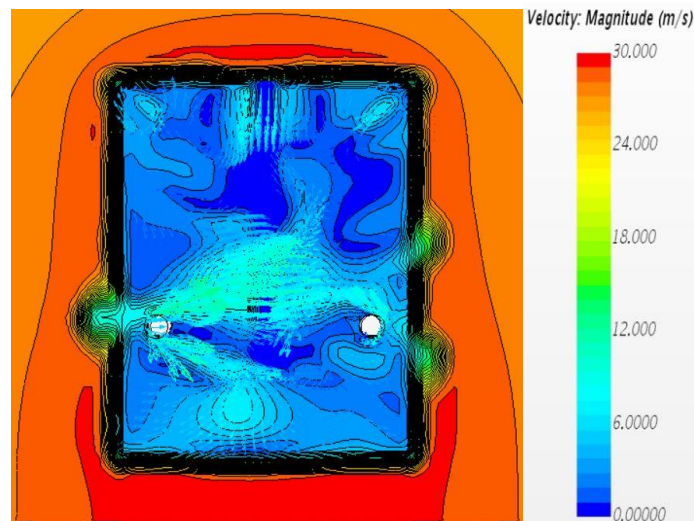
(l) Configuration O

Figure 6.18: Flow field in the gap on the YZ plane at x=0.026m viewed from the front face of the tractor.

6.2.4 Surface Pressure Distribution

The overall pressure drag is mainly due to high pressure regions on the front faces of the tractor and trailer. There is really not much that can be done to reduce high pressure region on the front face of the tractor and hence reducing high pressure regions on the front face of the trailer and decreasing the turbulence level in the gap region by different devices have been the focus of the research for the past several decades. Pressure distributions on the XY symmetry plane, the XZ-horizontal plane at y=0.20m and the front face of the trailer are presented in this section for all the nine configurations have a better understanding how the pressure change when the different drag reduction devices discussed above are deployed.

Figure 6.19 - 6.21 show pressure coefficient contours on the three planes mentioned above for configurations G – H and there are no significant differences between those three configurations. Especially on the front face of the trailer the pressure distributions for those three configurations are reasonably similar too. This is why the drag reduction is more or less the same apart from about 4% more drag reduction for configuration I with three CVTD. This is because the three CVTD configurations is highly effective in controlling the flow within the gap region when compared to single or two CVTD configurations. Therefore, a uniform pressure distribution is observed on the front face of the trailer.

(a)XY Plane**.**   (b) ZX Plane   (c)Front face of trailer
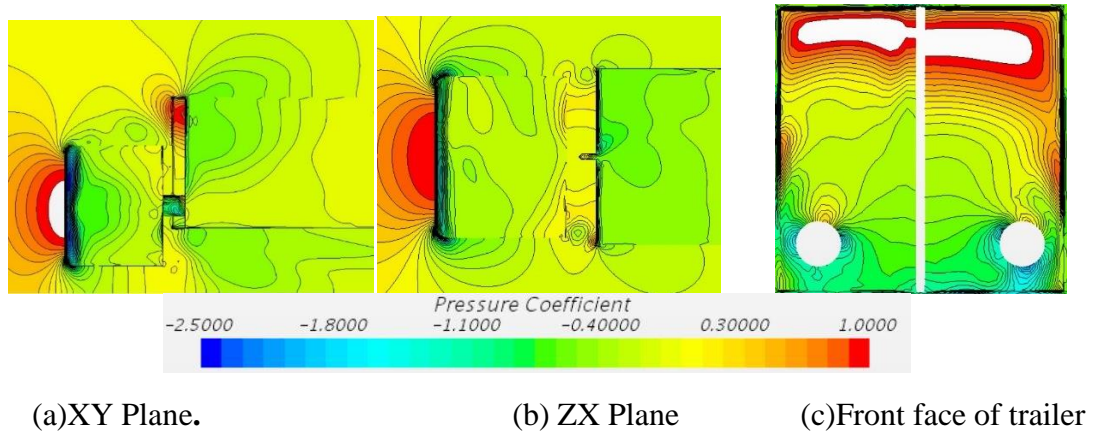
Figure 6.19: Pressure coefficient contours for configuration G.

(a)XY Plane.   (b) ZX Plane.   (c)Front face of trailer.
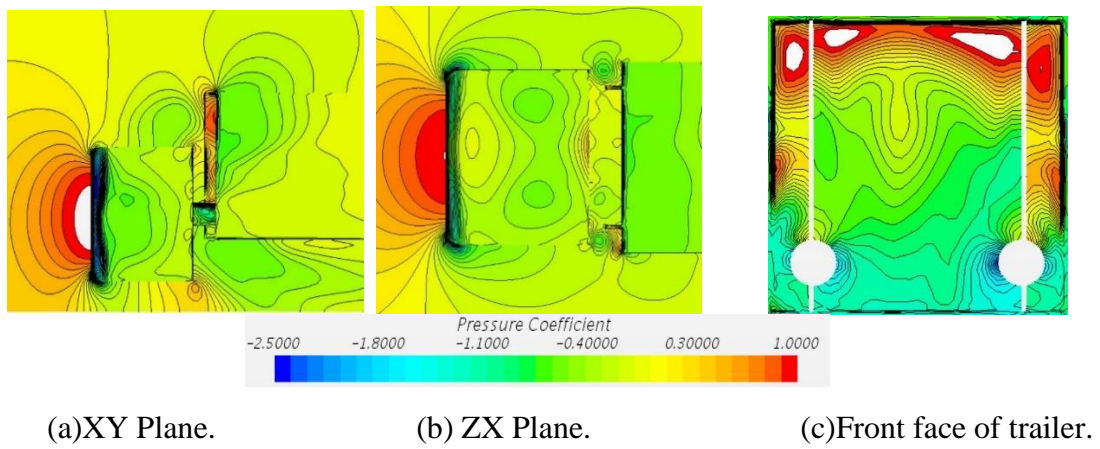
Figure 6.20: Pressure coefficient contours for configuration H.

(a)XY Plane.   (b) XZ Plane   (c) Front face of trailer.
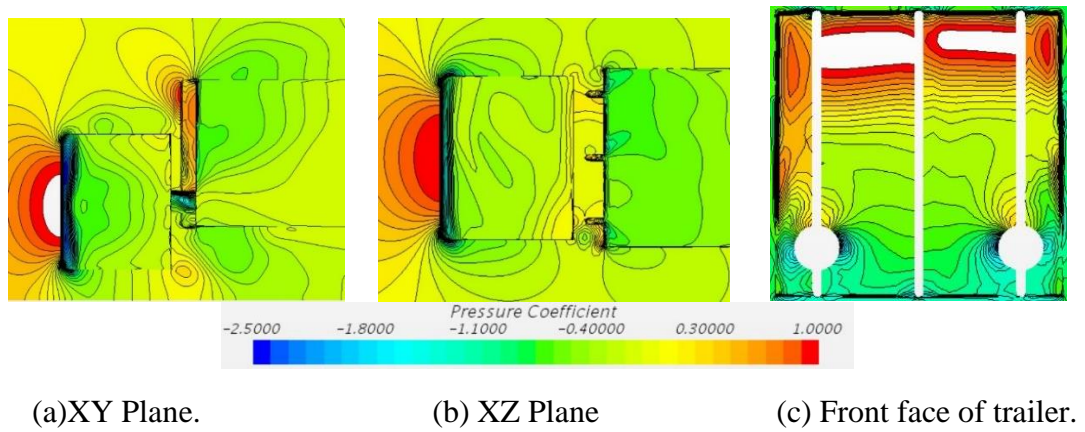
Figure 6.21: Pressure coefficient contours for configuration I.
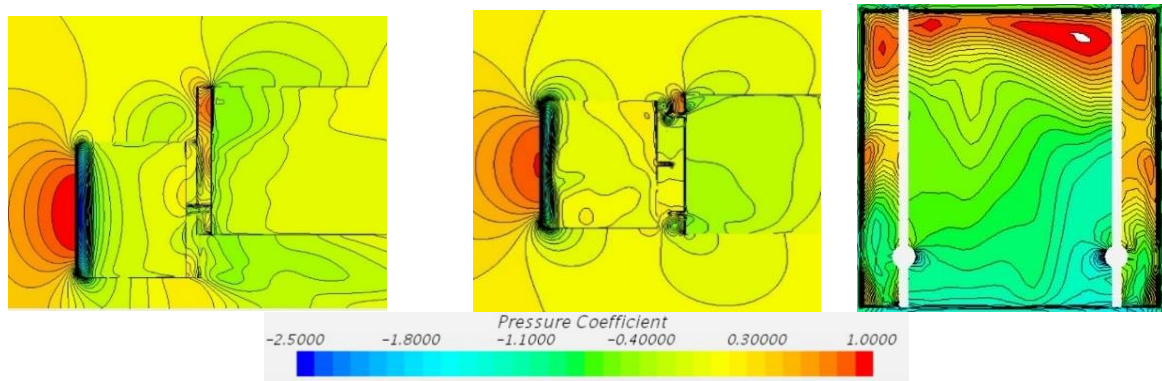
(a)XY Plane.   (b)XZ plane.   (c) Front face of trailer.

Figure 6.22: Pressure coefficient contours for configuration J.
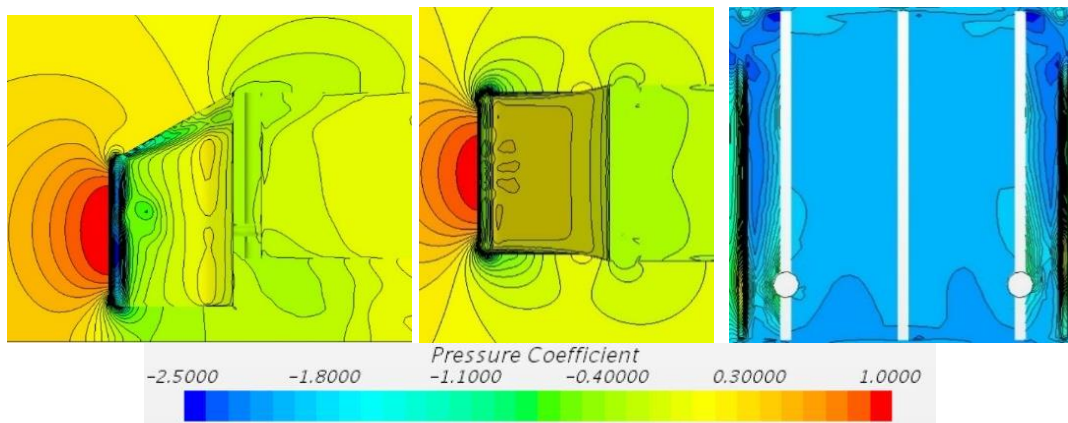
(a)XY plane.   (b)XZ Plane.   (c)Front face of trailer.

Figure 6.23: Pressure coefficient contours for configuration K.

When a roof deflector and side extenders are installed to the tractor for configurations K, L and N the high pressure regions on the front face of the trailer observed for configurations G – J are completed eliminated as shown in Figure 6.23c, Figure 6.23c and Figure 6.26c, due to a significant reduction of the amount of flow entering the gap and no flow impingement on the front face of the trailer. In addition, due to the deployment of three CVTD for those three configurations flow mixing is reduced, leading to less turbulence and a uniform pressure distribution, especially for configuration N the pressure on the front face on the trailer has a relatively very low value and its distribution is also relatively very uniform. Therefore the maximum drag reduction (47.58%) has been achieved for configuration N.
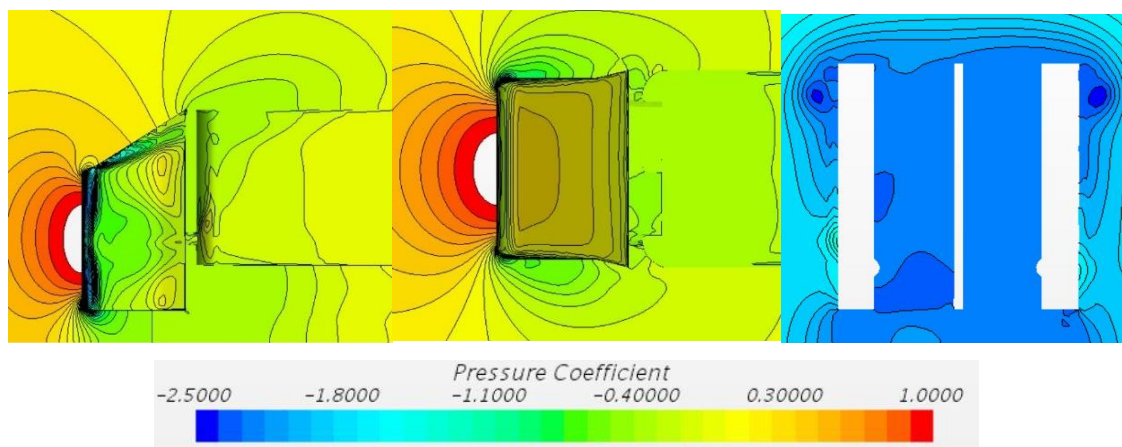
(a) XY Plane.   (b) XZ Plane.   (c) Front face of trailer.

Figure 6.24: Pressure coefficient contours for configuration L.
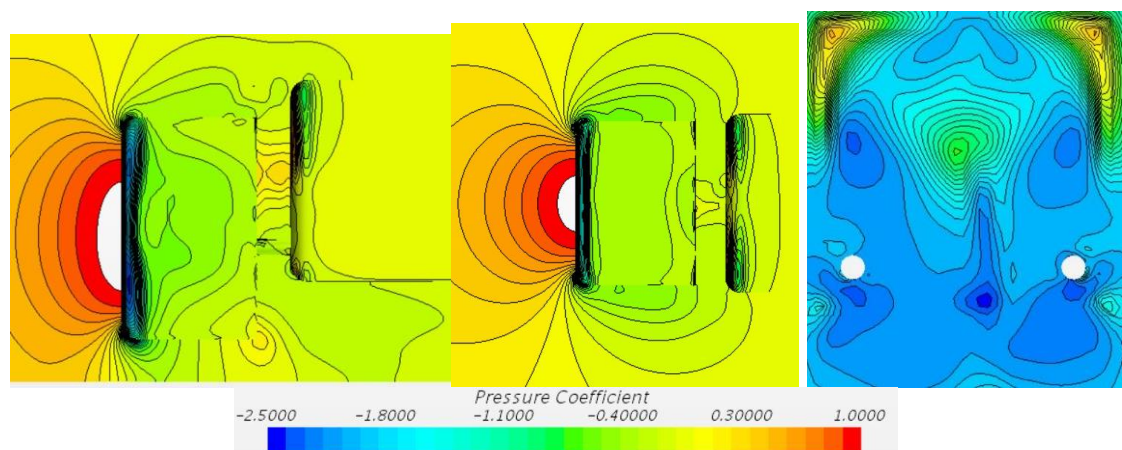
(a) XY Plane.   (b) XZ Plane.   (c) Front face of trailer.

Figure 6.25: Pressure coefficient contours for configuration M.
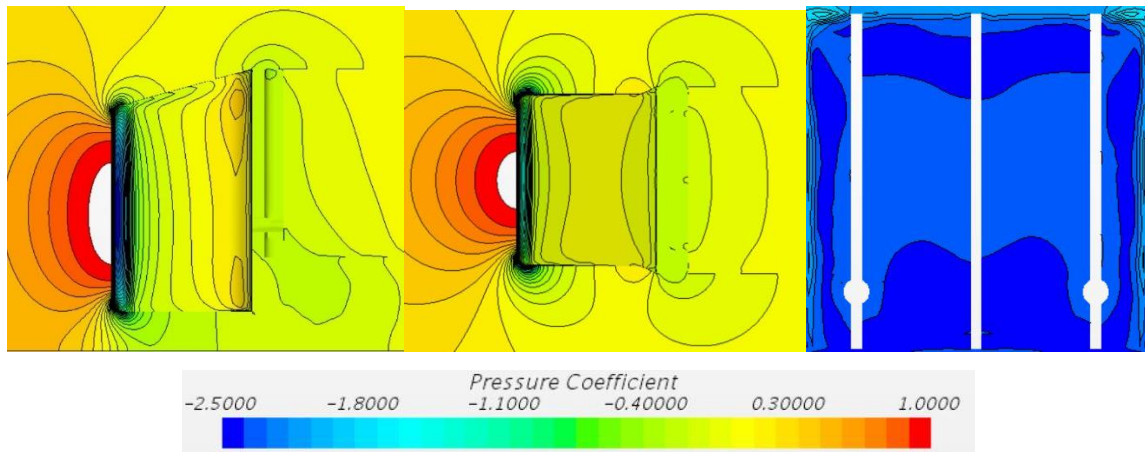
(a) XY Plane.　　　　　(b) XZ Plane.　　　　　(c) Front face of trailer.

Figure 6.26: Pressure coefficient contours for configuration N.
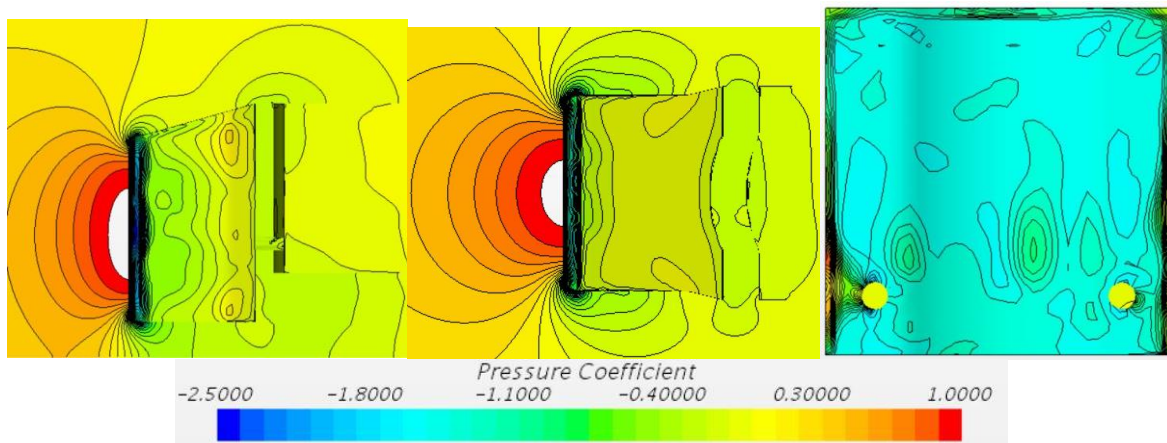
(a) XY Plane.　　　　　(b) XZ Plane.　　　　　(c) Front face of trailer.

Figure 6.27: Pressure coefficient contours for configuration O.

For configuration O with a bumped front face of trailer several vortices are formed on the front face of the trailer as shown in Figure 6.27c in the absence of CVTD devices to reduce flow mixing.

Across all these configurations, the length of the recirculation regions on top surfaces of the tractor and the trailer vary in length and height significantly depending on the type of devices mounted onto the tractor and trailer as shown in Figure 6.19 (a) – 6.27 (a). Nevertheless, this change does not really affect the overall pressure drag on the top surfaces.

Section 6.3

6.3.1 Base Bleeding Technique

Additional aerodynamic drag may arise due to flow separation in the tractor-trailer gap region, the base bleeding technique may be used to reduce or eliminate flow separation. The base bleeding technique is mainly used to streamline the body without major changes to its actual geometry. This technique was first proposed by a team of scientists working on heavy vehicle aerodynamic drag (Mccallen, et al., 2007). One of the motivations employing the bleeding technique is the maintenance issue, i.e., maintaining the aerodynamic add on devices for truck by the owners themselves in the long run. Due to varying aerodynamic loads acting on these devices, the feasibility of these devices becomes a big question mark. The advantage of this technique is that it eliminates the large and easily damageable structural surfaces. Base bleeding technique was mainly aimed at reducing drag of trucks in the base region. However, in this section, the bleeding technique will be used to see whether it can reduce drag generated in the gap region.

6.3.2 Configuration and Boundary Conditions

The bleeding technique is applied to configuration F studied in section one. Previous studies showed that one of the areas on the front face of the tractor with a high density of air flow stagnating is the air dam region located close to the base of the tractor. Hence it is logical to locate the inlet of the duct near the air dam region. The inlet for the bleeding flow is at the front face of the tractor as shown in Figure 6.28a. The outlet is at the back face of the tractor within the tractor side extenders as shown in Figure 6.28b. Ducts extend all the way to the lateral edges of the tractors back face. The duct inlets are located closer to the lateral edges of the tractor due to the presence of the engine bay and drivetrain located along the central region of the tractor. The boundary conditions for the simulations are kept at the same as those for configuration F (inlet velocity at 24.4m/s, with a moving ground, and pressure outlet boundary condition). The lateral walls and the top face of the computational domain are assigned a no-slip wall boundary condition.
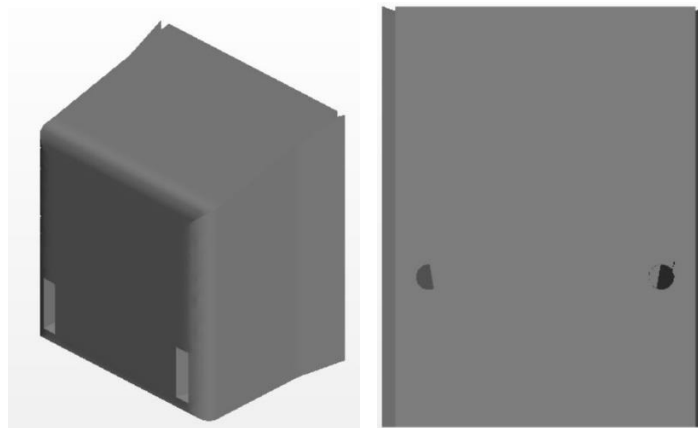
(a) Front face of tractor.   (b) Back face of tractor.

Figure 6.28: Schematic position of ducts for bleeding flow.

6.3.3 Analysis of Flow Field
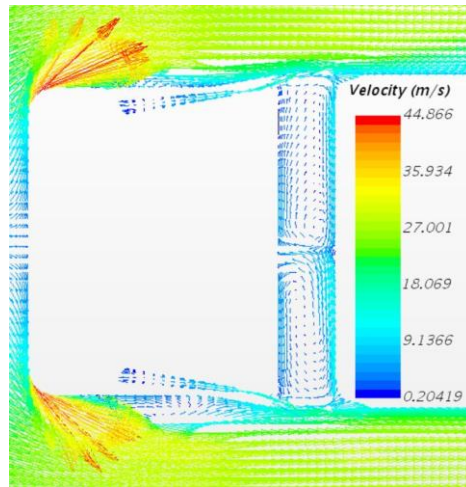
(a)
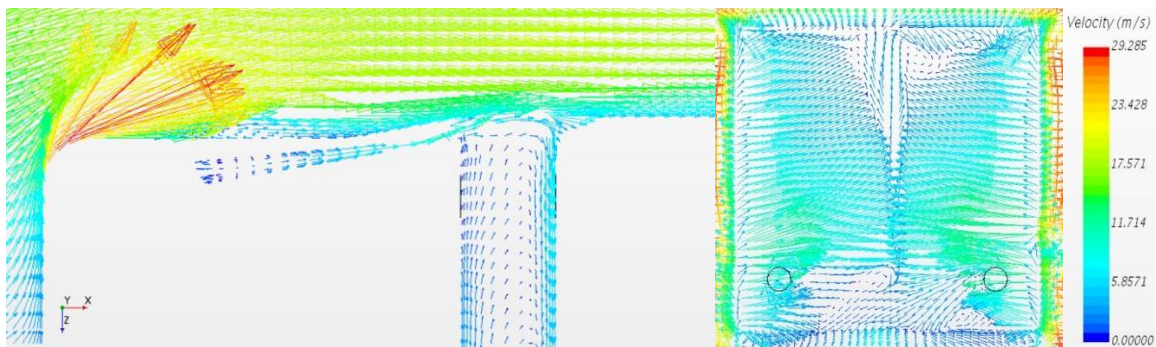
(b).   (c)

Figure 6.29: (a) - Velocity contours on the XZ plane at y=0.20m. (b) – Enlarged view of velocity contours at one corner of the tractor. (c) Velocity contours within the gap region.

Figure 6.29a presents the predicted velocity contours on the XZ plane at y=0.2m and it can be seen that the flow enters the ducts at the inlet which is on the front face of the tractor and exists through two ducts which are on the back face of the tractor within the side extenders, and then mix with the main flow field along the lateral sides of the truck. It can be seen from Figure 6.29b (detailed view of velocity contours at one corner of the tractor) that the flow separation along the lateral walls of the tractor is reduced with a smaller separation bubble compared with configuration F without flow bleeding as shown in Figure 6.3. Furthermore, the flow bleeding has also reduced the asymmetric nature of the flow within the gap itself, indicating that the base bleeding technique helps to even out the flow field around the tractor itself.

6.3.4 Surface Pressure Distribution

Figure 6.30 shows the predicted surface pressure distribution on the XZ plane at y=0.20m and on the front face of the trailer. It can be seen from Figure 6.30a that the pressure filed is quite smooth and uniform in the gap region, which means that there are no vortices formed in this region. In addition, it can be seen from Figure 6.30b that there exists two very small high pressure regions close to the edges of the trailer. This is due to the bleeding flow which exits from the tractor and impinges on the front face of the trailer. The ultimate assessment whether flow bleeding applied to the tractor can reduce the drag or not depending on the drag coefficient is reduced or not when compared with configuration F without flow bleeding. Table 6.4 presents the predicted drag coefficient for the bleeding test case and configuration F, it is clear that flow bleeding can, indeed, reduce the drag by 3.17%.

(a)   (b)
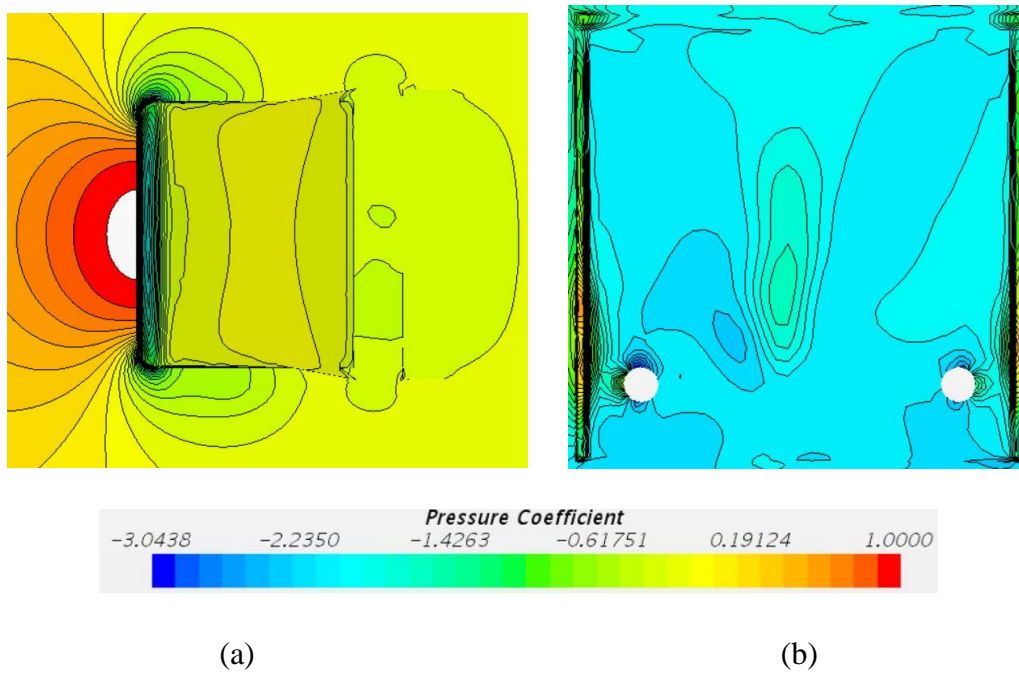
Figure 6.30: (a) – Pressure coefficient contours on the XZ plane at Y=0.20m, (b) - Pressure coefficient contours on the front face of the trailer.

Configuration	Cd	ΔC_d
Configuration F	0.441	
Configuration F with flow bleeding	0.427	-3.17%

Table 6.4: Predicted drag coefficients.

Summary

1. Strong flow interaction exists between the inward turning lateral flow and downwash from the top of the tractor in the gap region.

2. Adding the roof deflector to the tractor results in a reduction in the volume of flow entering the gap from the top of the truck.

3. The side extenders further reduce flow entering the gap region, ultimately leading to a low pressure on the front face of the trailer.

4. The use of both roof deflector and side extender has resulted in an immense drop in drag coefficient for the truck due to the significant reduction or elimination of high-pressure region on the front face of the trailer.

5. The use of CVTD in the gap has reduced the interaction between the flow entering the gap region from different directions and stabilized vortices, leading to less turbulent flow in the gap region. Also, triple CVTD is more effective then single or double CVTD.

6. The use of tractor mounted devices with triple CVTD in configuration K & N proved to be the most efficient solution in terms of drag reduction.

7. The bleeding technique has proved to a viable solution to manage the flow field in the gap and result in a further drag reduction of 3.17%.

8. No matter what drag reduction devices are deployed the drag reduction is mainly due to the reduced pressure on the front face of the trailer.

Further Discussion

It is evident from the present numerical study that several devices and their combinations are very effective in the drag reduction of a simplified generic truck consisting of a tractor and a trailer (as much as 40% drag reduction). Among the tractor mounted drag reduction devices, combining a roof deflecter and side extenders proves to be the most effective tool in reducing aerodynamic drag of a truck by more than 30%. Regarding drag reduction devices deployed inside the gap regions, several different configruations of CVTD have been tested and the triple CVTD configuration is the most effective one in terms of reducing flow mixing and stabilising vortices at 0° yaw angle, which results in less turbulent or even laminar flow.

It is also interesting to note that a high percentage of trucks on road currently are not fitted with those devices despite many studies suggest that those devices are very effective in drag reduction. This is mainly because the weight of those devices are not taken into account in those studies and in the current study, and hence the truck manufactueres or operators would compromise in the total payload of the vehicle to gain an aerodynamic benefit. The other limitations are the degree to which these devices cost for the operator to fit them onto their fleet of trucks. Therefore further studies are needed to clarify the net benefits of fitting those devices so that the truck manufactueres or operators can be convinced the net benefits of fitting on those devices.

Chapter 7

Conclusion and Future Work

Conclusion

In the present study, many drag reduction devices have been numerically tested and assessed regarding their effectiveness in reducing drag generated from the tractor trailer gap region for an articualted truck. A better understanding of the flow field around two identical bluff bodies in a tandem arragement has been achieved, which helps to understand the flow field within the gap region of a realistic heavy truck, elucidating the drag generation mechanisms in the gap region. Several turbulence models have been used to investigate the flow field within the gap region which have not been previously reported in the literature. This work has bridged the gap in the literature between tandem bluff bodies and realistic truck like test casses as this work has paved the way to a generalised method of reducing the drag which can be applied to a generic truck.

The first part of the present study is the investigation on the 3D tandem bluff bodies and the results from the simualtion agree reasonably well with the experimental data. The results from 2D bluff bodies are the stepping stone to understand the sudden jump in drag coefficeint which occurred in the GTS model at a critical gap. Literature on 2D tandem cubes confirmed the presence of a bi-stable regime in the gap region. However, with steady state numerical simulations only one instance could be predicted for a particular gap spacing. Hence the sudden jump in drag coefficient could be captured on two succeding gap ratios. The numerical results of the drag coefficeint corelate to the experimental data well. The numerical predictions show that the flow field around 2D tandem cubes are dominated by strong reciruclation regions around the cubes,within the gap and in the wake region. In comparison 3D cubes are featured by flow field which consist of horseshoe vortices formed due to flow separation from the first and second cube.

The second part of the present study focuses on a realistic truck like test case to assess the effectiveness of several drag reduction devices. A generic test case has been chosen to match a realistic truck bearing in mind the truck geometry in the European region and legislation which govern the dimensions of these trucks. However, it is also worth pointing that the generic test case is still a simplified version of a real truck, e.g., the wheels are not included in the generic test case.

The flow field around the generic test case is dominated by several recirculation regions and vortices, which increase the turbulence in the gap region, and ultimately leads to an increase in drag coefficient. The predictions also clearly show certain high pressure regions on the

front faces of the tractor and trailer which are the main cause of drag. The addition of tractor mounted drag reduction devices, especially a roof deflector, has proved to be a very effective solution to reduce or eliminate the high pressure regions on the front face of the trailer, leading to a significant drag reduction. The tractor mounted drag reduction devices aslo decrease the amount of flow entering the gap region from the top and from the sides of the tractor, which reduces flow interactions in the gap region, leading to less trubulence and hence less drag.

Deploying the CVTD in the gap region reduces flow mixing and stabilise vortices, which would result in reducing the turbulence in the gap region and hence ultimately leads to reduction in drag coefficeint of the truck. Three different configurations of CVTD (single CVTD, two CVTD and triple CVTD) have been evaluated and the triple CVTD proves the most effective one anomg the three configurations. The use of higher CVTD makes the structure more impractical due to the increase in weight, need of regular maintenance, structure more complicated and other practical issues. The combination of tractor mounted drag reduction devices (a roof deflector and side extenders) with the triple CVTD results in the maximum reduction among all different configurations with different drag reduction devices.

Increasing the height of the tractor in the generic test case also results in certain amount of drag reduction because the amount of flow entering the gap region from the top of the truck is reudced, leading to a significant reduction of high pressure regions on the front face of the trailer.

Altering the geometric shape of the back face of tractor and front face of trailer proves to make a significant change in the flow field. The flow pattern within the gap region are much more smoother due to the curved nature of the two faces, leading to drag reduction but this kind of geometric changes to the tractor and trailer may not be practical.

Applying the base bleeding technique to the tractor has changed the flow field within the gap to some degree, leading to a small percentage of drag reduction.

In summary, the drag reduction in the gap region has been achieved mainly due to reducing the amount of flow entering the gap region, resulting in a significant reduction of high pressure regions on the front face of the trailer.

Future Work

There is potentially a significant amount of work which can be undertaken to further investigate drag reduction devices comprehensively based on the findings of the present study. It is worth noting that due to limited available computing power the simulations have been carried out using the RANS approach (steady simulations) in the present study while in real truck case the flow is always unsteady. Therefore, it is highly recommended that one of the most important and imminent work is to simulate the same test case mounted with the same drag reduction devices using the Unsteady RANS and LES approaches to confirm the findings of the present study and also to provide instantaneous inforamtion so as to improve our current knowledge of the flow fields, pressure distributions and so on, leading to a better understanding how those drag reduction devices work and ultimately end up with improved/better design of those drag reduction revices or even new drag reduction devices.

Considering the inflow boundary conditions itself, numerical simulations at several different yaw angles should be carried out to understand how those drag reduction devices perform at different yaw angles because in reality the yaw angle cannot be a constant as wind will change directions or a truck will turn from time to time.

It is worth pointing out that the Reynolds numbers in all the simulations are lower than the Reynolds number (Re = 645,000) of a real truck travelling at 70 miles per hour since the simulations are usually based on a wind tunnel test case. Further studies at a realistic truck Reynolds number are needed to identify the effects of Reynolds number on the results and to make sure that those drag reduction devices would be still effective for flows at a realistic Reynolds number.

Further drag reduction maybe be possible by testing devices with different shapes, sizes, angles etc. using a proper optimisation method. Ideally, in this kind of optimisation studies, LES approach should be used to get a better understanding of the unsteady flow features around a truck and the test case should be more realistic, including wheels, and the flow Reynolds number should be the same as the Reynolds number in a real truck travelling at 70 miles per hour.

References

1. Research Gate,, 2016. *Research Gate.* [Online] Available at: https://www.researchgate.net/post/Y_setting_in_Star_CCM [Accessed 30 May 2019].

2. Ahamed, S. R., Gawthorpe, R. G. & Mackrodt, P. A., 1985. Aerodynamics of Road and Rail vehicles. *Vehicle System Dynamics,* Volume 14, pp. 319-392.

3. Ahamed, S. R., Ramm, G. & Flatin, G., 1984. Some Salient features of the time averaged ground vehicle wake. *SAE,* Volume 840300.

4. Allan, J. W., 1981. AERODYNAMIC DRAG AND PRESSURE MEASUREMENTS ON A SIMPLIFIED TRACTOR--TRAILER MODEL*. *Journal Wind eng and ind aerodynamics,* Volume 9, pp. 125-136.

5. Allen, 2019. *CDL Training Spot.* [Online] Available at: https://cdltrainingspot.com/what-is-considered-a-straight-truck-with-pictures/ [Accessed 04 02 2020].

6. Alti, M. E., Chernoray, V., Jahanmiri, M. & Davidson, L., 2012. Experimental and computational studies of active flow control on a model truck-trailer. *Experimental Fluid Mechanics 2011,* Volume 25, p. 16.

7. Anderson, J. D., 2005. *Introduction to Flight,* Maryland: MCGraw Hill Book Company.

8. Ansys, INC;, 2009. *Spatial Discretization,* s.l.: Ansys.

9. Atkin, E., 2010. *Germany Has Proven the Modern Automobile Must Die.* [Online] Available at: https://www.wired.com/story/germany-proves-cars-must-die/ [Accessed 08 10 2019].

10. Baldwin, B. & Lomax, H., 1978. *Thin-layer approximation and algebraic model for separated turbulentflows.* Alabama, AIAA.

11. Bearman, P. W., 1997. Near wake flow of two and three dimensional bluff bodies.. *Journal of Wind eng and ind aerodynamics,* Volume 69, pp. 33-54.

References

12. Belzile, M., 2012. *Review of Aerodynamic Drag Reduction Devices for Heavy Trucks and Buses,* Ottawa: National Research council Canada.

13. Bracco, R. et al., 2016. Convenient - Complete Vehicle energy saving technologies ofr heavy trucks. *Transportation rEsearch Procedia,* 14(2016), pp. 1041-1050.

14. Bradley, R., 2000. *Technology roadmap for the 21st century truck program,* Washington DC: US department of energy.

15. Brahmaliuc, R., 2019. *Truck Designs: 3 CFD simulations for improving truck aerodynamics,* s.l.: Simscale.

16. Browand, F. & Hammache, M., 2004. *The limits of drag behaviour for two bluff bodies in tandem.* Detroit, s.n.

17. Buil, R. M. & Herrer, L. C., 2009. Aerodynamic analysis of a vehicle tanker. *Journal fluid eng,* 131(4), p. 14.

18. Cab specifications for Volvo FH, n.d. *Cab Dimensions.* [Online] Available at: https://www.volvotrucks.se/sv-se/trucks/volvo-fh/specifications/cab.html# [Accessed 04 02 2020].

19. Castelucci, P. J. & Salari, K., 2005. Computational Simulation of Tractor-Trailer Gap Flow with Drag-Reducing Aerodynamic Devices. *SAE,* 1(724).

20. Celik, I., 1999. *Introductory turbulence modeling.* Morgantown: West Virginia University.

21. Charles, T., Lu, Y. & Yang, Z., 2017. *Impact of gap size between two bluff bodies on the flow field.* Portoroz, s.n.

22. Charles, T., Yang, Z. & Lu, Y., 2019. Numerical NAalysis of Flow in the gap bertween a Simplified Tractor Trailer Model with Cross Vortex Trap Device.. *International Journal of Mechanical and Mechatronics Engineering,* 13(11), pp. 707-711.

23. Chilbule, C., Upadhyay, A. & Mukkamala, Y., 2014. *Analyzing the profile modification of truck-trailer to prune the aerodynamic drag and its repercussion on fuel consumption.* Vellore, s.n.

References

24. Choi, H., Lee, J. & Park, H., 2013. Aerodynamics of Heavy Vehicles. *Annual Review Fluid Mechanics,* Volume 46, pp. 441-468.

25. Coon, J. D. & Visser, K. D., 2004. rag Reduction of a Tractor-Trailer Using Planar Boat tail plates. *Springer Link,* Volume 1, pp. 249-265.

26. Cooper, K., 2002. *Commercial vehicle aerodynamics drag reduction: historical perspective as a guide,* Monterey: National Research Council.

27. Cooper, K. & Leuschen, J., 2005. Model and Full-Scale Wind Tunnel Tests of Second-Generation Aerodynamic Fuel Saving Devices for TRactor-trailer. *SAE,* p. 13.

28. Cooper, K. R., 1985. The effect of front edge rounding and rear edge shaping on the aerodynamic drag of bluff veicles in ground proximity. *SAE,* p. 36.

29. Cooper, K. R., 2002. Truck Aerodynamic Reborn - Lesson from the past. *SAE,* p. 13.

30. Croll, S., Gutierrez, R. & Hassan, W., 1996. Experimental investigation of the ground transportation systems (GTS) project for heavy vehicle drag reduction. *SAE,* pp. 235-259.

31. Cuotto, N., 2016. *Buddies on the Road,* Gothenburg: Chalmers UNiversity of Technology.

32. Darekar, R. M. & Sherwin, S. J., 2001. Flow past a square-section cylinder with a wavy stagnation face. *Journal of Fluid Mechanics,* Volume 426, pp. 263-295.

33. Delgado, O. & Rodriguez, F., 2018. *Co2 emission and fuel consumption standards for heavy duty vehicle in the european union.,* s.l.: The int council of clean transport.

34. Don Bur, 2016. *Don Bur - Tear drop trailers.* [Online] Available at: https://donbur.co.uk/gb-en/products/aerodynamic-teardrop-trailer.php [Accessed 18 02 2020].

35. Easton, H. A. & Cromer, G. C., 2019. *Encylopaedia Britannica.* [Online] Available at: https://www.britannica.com/technology/truck-vehicle [Accessed 04 02 2020].

36. Englar, R., Smith, M., Niebur, C. & Gregory, S., 1996. Aerodynamic concepts for control of lift, drag and moments plus lateral.directional stability of automotive vehicles.. *SAE technical paper series,* Volume 960673.

37. EPA, 2015. *Inventory of US greenhouse gas emissions and sink,* s.l.: EPA.

38. EPA, 2019. *EPA.* [Online]
Available at: https://www.epa.gov/ghgemissions/sources-greenhouse-gas-emissions
[Accessed 28 01 2020].

39. European Commision, 2017. *European Commission Website, Transport.* [Online]
Available at: https://ec.europa.eu/clima/policies/strategies_en
[Accessed 29 08 2020].

40. European Commission, 2016. *Mobility and Transport.* [Online]
Available at: https://ec.europa.eu/transport/modes/road/weights-and-dimensions_en
[Accessed 04 02 2020].

41. European Strategy of Low emission, 2016. *European Commission.* [Online]
Available at: https://ec.europa.eu/transparency/regdoc/rep/1/2016/EN/1-2016-501-EN-F1-1.PDF
[Accessed 03 02 2020].

42. Freight best practise, 2007. *Aerodynamics for efficient road freight operations,* London: Department of transport.

43. Fu, L., 2011. *Automobile Design and Aerodynamics,* Beijing: China Machine Press.

44. Good, G. L. & Garry, K., 2004. On the use of Reference models in automotive model in automotive aerodynamics. *SAE technical paper.*

45. Grandemange, M., 2013. *Analysis and control fo three dimensional turbulent wake: from axisymmetric bodies to road vehicles,* Paris: ENSTA Paris tech, Ecole Polytechnique.

46. Hak, G. E. M., 2005. *Flow Control,* s.l.: CRC Press.

47. Hakkansson, C. & Lenngren, M., 2010. *CFD Analysis of aerodynamic trailer devices for drag reduction of heavy duty trucks,* Goteborg: Chalmers University of Tech.

48. Hammache, M. & Browand, F., 2004. On the aerodynamics of tractor-trailer. *Dept of Aerospace and mechanical engineering, University of Southern California,* pp. 187-205.

49. Hanfeng, W., Yu, Z. & Xuhui, H., 2016. Aerodynamic drag reduction fo an ahmed body based on deflectors. *J of wind eng and ind aerodynamics,* Volume 148, pp. 34-44.

50. Hangan, H. & Vikery, B. J., 1999. Buffeting of two-dimensional bluff bodies. *Journal of Wind Engineering and Industrial Aerodynamics,* 82(1-3), pp. 173-187.

51. Hariram, A., Koch, T., Mardberg, B. & Kyncl, J., 2019. A Study in Options to Improve Aerodynamic Profile of Heavy-Duty Vehicles in Europe. *MDPI,* Volume 11, p. 23.

52. Havel, B., Hangan, H. & Martinuzzi, R., 2001. Buffeting of 2D and 3D sharp edged bluff bodies. *J of Wind eng,* Volume 89, pp. 1369-1381.

53. Heisler, H., 2002. *Vehicle body aerodynamics,* London: 584-634.

54. High Capacity Transport, 2019. *ACEA.* [Online] Available at: https://www.acea.be/publications/article/paper-high-capacity-transport [Accessed 04 02 2020].

55. Hjelm, L. & Bergqvist, B., 2009. European Truck Aerodynamics–A Comparison Between Conventional and CoE Truck Aerodynamics and a look into future trends and possibilities.. *Springer link,* Volume 41, pp. 469-477.

56. Holmes, H. R., 1976. *Practical Economics aspects of tractor/trailer aerodynamics.* s.l., s.n.

57. Houghton, E. L. & Valentine, D. L., 2015. Basic Concenpts and Definitions. In: *Aerodynamics for Engineering students.* s.l.:Batterworth-Heinmann, p. 688.

58. Howell, J. & Good, G. L., 2008. The effect of backlight aspect ratio on vortex and base drag for a simple car like shape. *SAE,* p. 9.

59. Howell, J., Passmore, M. & Tuplin, S., 2013. Aerodynamics Drag reduction on a simple car like shape with rear upper body taper. *SAE int J Passenger cars,* Volume 6, pp. 52-60.

60. Hucho, W. H., 1998. *Aerodynamics of Road Vehicles.* Warrendale: SAE Int.

61. Hucho, W. H. & Sovran, G., 1993. Aerodynamics of Road Vehicles. *Ann rev of Fluid mechanics,* Volume 25, pp. 485-537.

62. Hummel, D., 1987. Chapter 2 - Some fundamentals of fluid mechanics.. In: *Aerodynamics of Road Vehicles.* s.l.:Butterworth Heinmann, pp. 47-82.

63. Hyams, D. G. et al., 2011. Computational simulation of model and full scale Class 8 trucks with drag reduction devices. *Computer and Fluids,* 41(2011), pp. 27-40.

64. Imam, A. S., Chinta, B. & Thorpe, S., 2011. optimum constraints strategy for liftgates. *SAE,* p. 7.

65. Iveco, 2008. *Innovation for the future, the future is here-transport concept,* Torino: Iveco SPA.

66. Jiyuan, T., Yeoh, G. & Liu, C., 2018. CFD mesh generation: a practical guideline. In: *Computational Fluid Dynamics.* s.l.:s.n., pp. 125-152.

67. Jones, W. & Launder, B., 1972. The Effects of Maternal Diets, Varying in Fat Content, on Proximal Hepatic and Skeletal Muscle Insulin Signalling in Neonatal Wistar Rat Offspring. *International Journal of Heat and Mass Transfer,* Volume 15, pp. 301-314.

68. Seigel, K., n.d. *Transportation and Global warming,* California: Center of Bilogical Diversity.

69. Khaligi, B., Zhang, S. & Koromilas, C., 2001. Experimental and Computational Study of Unsteady Wake Flow Behind a Bluff Body with a Drag Reduction Device. *SAE,* 110(6), p. 16.

70. Kim, M., Kim, D., Yoon, S. & Lee, D., 2008. Measurements of the flow fields around two square cylinders in a tandem arrangement. *J of mechanical sciences and technology,* 22(2008), pp. 397-407.

71. Kumar, P. & Chaurasia, N., 2016. Enhancement of Aerodynamic Efficiency of Truck-Trailer. *Int J of Innovative Research in Science, engineering and technology. ,* 5(6), pp. 9563-9573.

72. Kuo, E. Y. & Mehta, P. R., 2005. The effects of Body joint designs on liftgate chucking performance. *SAE,* p. 10.

73. Larson, C. D., 2011. *Comparison of Three Degree of Freedom and Six Degree of Freedom Motion Bases Utilizing Classical Washout Algorithms,* Iowa: Iowa State University.

References

74. Launder, B. E., 1972. the Effects of Maternal Diets, Varying in Fat Content, on Proximal Hepatic and Skeletal Muscle Insulin Signalling in Neonatal Wistar Rat Offspring. *International Journal of Heat and Mass Transfer,* Volume 15, pp. 301-314.

75. Luo, S. C. & Teng, T. C., 1990. Aerodynamic Forces on a Square Section Cylinder That is Downstream to an Identical Cylinder.. *The Aeronautical Journal,* Volume 94, pp. 203-212.

76. Malviya, V., Mishra, R. & Fieldhouse, J., 2009. CFD Investigation of a novel fuel saving device for articulated tractor traile combination.. *Engineering Applications of Computational Fluid Mechanics,* 3(4), pp. 587-607.

77. Martini, H., 2016. *Perspectives of Aerodynamic Drag and Cooling Airflow for Heavy-Duty Trucks - Reconsidering European Total-Length Legislation,* Gothenburg: Chalmers University of Technology.

78. Martinuzzi, R. & Havel, B., 2004. Vortex Shedding of two surface mounted cubes in tandem. *Int j of Heat fluid flow,* 25(3), pp. 364-372.

79. Martinuzzi, R. J. & Havel, B., 2000. Turbulent flow around two surface mounted cubic obstacles in tandem arrangement. *J or Fluid eng,* 122(1), pp. 24-31.

80. Mason, W. T. & Beebe, P. S., 1978. The drag related flow field characteristics of trucks and buses. In: *Aerodynamic Drag Mechanisms of Bluff Bodies and Road Vehicles.* Boston: Springer Link, pp. 45-93.

81. Mccallen, R., Salari, K. & Ortega, J., 2004. *DOE's Effort to Reduce Truck Aerodynamic Drag through Joint Experiments and Computations Lead to Smart Design.* s.l., s.n.

82. Mccallen, R., Salari, K., Pointer, W. D. & Ross, J., 2007. *DOE Project Heavy vehicle aerodynamic drag,* s.l.: Lawrence Livermore National Laboratory.

83. Menter, F. R., 1994. Two-equation eddy-viscosity turbulence models for engineering applications. *AIAA,* 32(8), pp. 1598-1605.

84. Mercedes Benz, 2020. *Mercedes Benz.* [Online] Available at: https://tools.mercedes-benz.co.uk/current/trucks/brochures/products/truck-range.pdf [Accessed 14 02 2020].

References

85. Minelli, G., 2017. *Active flow control for reducing drag on trucks: from concept to full scale testing,* Goteborg: Chalmers University of Technology.

86. Motorway standard speed limits in Europe, 2015. *Studentnews,eu.* [Online] Available at: https://trip.studentnews.eu/s/4086/77072-Motorways-standard-speed-limits-in-Europe.htm
[Accessed 04 02 2020].

87. Ni, Q. X. & Qi, L. Y., 2011. Experimental and numerical studies of aerodynamic performance of trucks. *Journal of Hydrodynamics,* 23(6), pp. 752-758.

88. Obidi, Y. T., 2004. Trucks, Trailer and buses. In: *Theory and application of aerodynamics of ground vehicles.* Pennsylvania: SAE, pp. 155-171.

89. Okajima, A., 1979. Flow around two tandem ciruclar cylinders at very high reynolds number. *JSME,* 17(11), pp. 504-511.

90. Osth, J. & Krajnovic, S., 2012. The flow around a simplified tractor-trailer model studies by LES. *J of Wind eng and ind aerodynamics,* Volume 102, pp. 36-47.

91. Oversize or overmass vehicles, 2020. *NT.GOVE.AU.* [Online] Available at: https://nt.gov.au/driving/heavy/oversize-or-overmass-vehicles/dimension-limits
[Accessed 04 02 2020].

92. Pankajakshan, R., Sirnivas, K., Mitchell, B. & Whitfield, D., 2007. CFD Simulations of Class 8 Trucks. *SAE Int,* p. 7.

93. Park, J. H., 1995. A laser-Doppler velocimetry study of ensemble-averaged characteristics of the turbulent near wake of a square cylinder. *Journal of Fluid Mechanics,* Volume 304, pp. 285-319.

94. Paul, J. R., 2017. The issue of transport and the environment. In: *The Geography of transport systems.* New York: s.n., p. 440.

95. Peng, J. et al., 2018. Research on the aerodynamic characteristics of tractor-trailers with a parametric cab design. *Applied Sciences,* 8(5).

96. Perry, A. K., 2016. *An investigation into the base pressure of simplified automotive squareback geometries,* Loughborough: Louighborough University.

References

97. Perry, A. K., Passmore, M. & Finney, F., 2015. Influence of short rear end tapers on the base pressure of a simplified vehicles. *SAE,* Volume 8, pp. 317-327.

98. Quang, L., 2019. *UNESCAP.* [Online] Available at: https://www.unescap.org/sites/default/files/China_20.pdf [Accessed 04 02 2020].

99. Rao, A. N. & Minelli, G., 2018. Investigation of the near-wake flow topology of a simplified heavy vehicle using PANS simulations. *J of Wind end and ind aero,* Volume 183, pp. 243-272.

100. Renault Trucks Optifuel Lab 3 aims to reduce heavy-duty diesel truck fuel consumption by 13%, 2018. *Green Car Congress.* [Online] Available at: https://www.greencarcongress.com/2018/09/20180923-optfuel3.html [Accessed 04 02 2020].

101. Ricciardelli, F., 1994. *Aerodynamics of a pair of square cylinders,* Ontario: The University of Western.

102. Ross, J. & Mahta, R., 2006. *Heavy Vehicle Drag reduction experimental evaluation and design.* [Online] Available at: https://www1.eere.energy.gov/vehiclesandfuels/pdfs/hvso_2006/05_ross.pdf [Accessed 26 02 2020].

103. SAE China, 2001. *Good practice guide 308, truck aerodynamics styling.* Berlin, s.n.

104. Said, N., Mhiri, H., Palec, G. & Bournot, P., 2008. Wind Tunnel Investigation and Numerical Simulation of the Near Wake Dynamics for Rectangular Obstacles. *Eng eng science,* 25(7), pp. 1037-1060.

105. Sakamoto, H., Haniu, H. & Obata, Y., 1987. Fluctuating forces acting on two square prisms in a tandem arrangement. *J of wind eng and ind aerodynamics,* Volume 26, pp. 85-103.

106. Sakamoto, H., Haniu, H. & Obata, Y., 1988. The effect of free stream turbulence on the characteristics of fluctuating forces acting on two square prisms in tandem arrangement. *Journal of fluids eng,* 110(2), pp. 140-146.

References

107. Saltzman, E. J. & Meyer, R. R., 1999. A Reassessment of Heavy-Duty Truck Aerodynamic Design Features and Priorities. *NASA,* p. 38.

108. Seyyedvalilu, H., 2018. *Difference between standard and realizable k-epsilon model, Researchgate.* [Online] Available at: https://www.researchgate.net/post/Difference_between_standard_and_realizable_k-epsilon_model#:~:text=The%20realizable%20k%2D%C9%9B%20model,%C9%9B%20model%20in%20two%20ways.&text=As%20a%20guess%20I%20would,a%20problem%20in%20both%20cases. [Accessed 21 05 2020].

109. Sharma, R. K. & Kumar, S., 2012. Impact of transportation system on environment in developing contries "A Review". *Internation jouirnal of Research review in Engineering science and technology,* 1(2), pp. 61-66.

110. Shih, T. H. et al., 1995. A new k-ε{lunate} eddy viscosity model for high reynolds number turbulent flows. *Computers and Fluids,* 24(3), pp. 227-238.

111. Simscale, 2016. *Pinterest.* [Online] Available at: https://www.pinterest.com/pin/9288742961712864/ [Accessed 06 09 2020].

112. Sitlani, M. P. & Aung, K., 2006. *Numerical Simulation on Aerodynamic drag of ground transport system.* Illinois, s.n.

113. Skrucany, T., Sarkan, B. & Gnap, J., 2016. Influence of Aerodynamic Trailer devices on drag reduction measure in a wind tunnel. *Eksploatacja i Niezawodnosc – Maintenance and Reliability,* 18(1), pp. 151-154.

114. Spalart, P. R. & Allmaras, S. R., 1992. *A One-Equatlon Turbulence Model for Aerodynamic Flows A ONE-EQUATION TURBULENCE MODEL FOR AERODYNAMIC FLOWS.* RENO, AIAA.

115. Spentzos, A., 2005. *CFD Analysis of 3D Dynamic stall,* Glasgow: University of Glasgow.

References

116. Srinivas, K., Pankajakshan, R. & Taylor, L., 2006. *Aerodynamic Simulation of Heavy Trucks with Rotating Wheels.* Nevada, 44th AIAA Aerospace Sciences Meeting and Exhibit.

117. Star CCM+, 2020. *Star CCM+ user guide.* [Online] Available at: file:///C:/Program%20Files/Siemens/15.02.009/STAR-CCM+15.02.009/doc/en/online/index.html#page/STARCCMP%2FGUID-B52EEA73-AA46-4E60-9F85-4779E3C7397D.html [Accessed 09 09 2020].

118. Star CCM+, 2020. *Volume growth rate/Template growth rate.* s.l.:Siemens.

119. Star CCM+, 2020. *Wall Treatment.* [Online] Available at: file:///C:/Program%20Files/Siemens/15.02.009/STAR-CCM+15.02.009/doc/en/online/STARCCMP/GUID-2E8C2999-B5FC-4C95-B934-734059C9B045.html#wwconnect_header [Accessed 08 09 2020].

120. Steinmetz, K., 2017. *Driving the green revolution in transportation Technology advancements further electrify cars, enable new efficiencies.* Stuttgart, EVS 2017 - 30th International Electric Vehicle Symposium and Exhibition (2017).

121. Stoesser, T., Mathey, F., Frohlich, J. & Rodi, W., 2003. LES of Flow over Multiple Cubes. *ERCOFTAC Bulletin,* 56(March), pp. 1-5.

122. Storms, B. L., Cross, J. C. & Heineck, J. T., 2001. An Experimental System Study of the Ground Transportation System (GTS) in the NASA Ames. *Nasa,* p. 22.

123. Thiria, B. & Diana, R. G., 2018. On the diverse roles of fluid dynamic drag in animal swimming and flying. *Journal of Royal Society Interface,* Volume 15, p. 13.

124. Truck Manufactueres Association, 2007. *Test, Evaluation, and Demonstration of Practical Devices/Systems to Reduce Aerodynamic Drag of Tractor/Semitrailer Combination Unit Trucks ,* Washington DC: National Energy Technology Laboratory.

125. US department of transportation, 2001. *Weights and Dimensions of Vehicles Regulations.* [Online] Available at: https://novascotia.ca/just/regulations/regs/mvwd.htm [Accessed 30 04 2020].

126. Varney, M., 2018. *Base drag reduction for squareback road vehicle,* Loughborough: Loughborough university.

127. Varney, M., Passmore, M. & Gaylard, A., 2017. The effect of passive base ventillation on the aerodynamic drag of a generic SUV vehicle. *SAE Int J of Passenger cars,* Volume 10, pp. 345-357.

128. Verzicco, R., Fatica, M. & Iaccarino, G., 2002. Large Eddy Simulation of a Road Vehicle with Drag-Reduction Devices. *2012,* 40(12), pp. 2447-2455.

129. Vino, G., Watkins, S., Mousley, P. & Watmuff, J., 2005. Flow stucture in the near wake of the Ahmed Model. *J of fluids and structures,* 20(5), pp. 673-695.

130. Werle, H. & Gallon, M., 1973. Sillages De Cheminees, Faisceaux Tubulaires, Grilles Et Turbomachines. Quelques Exemples De Visualisations Bases Sur L'Analogie Hydraulique. *Houille Blanche,* 28(4), pp. 339-341.

131. Wikipedia, 2019. *Semi trailer truck.* [Online] Available at: https://en.wikipedia.org/wiki/Semi-trailer_truck#Australasia [Accessed 04 02 2020].

132. Wilcox, D. C., 1988. Reassessment of the scale-determining equation for advanced turbulence models. *AIAA,* 26(11), pp. 1299-1310.

133. Wolenski, M., 2017. *Tempus Transport.* [Online] Available at: http://tempustransport.com/trucking-blog/2017/06/09/top-3-reasons-to-go-over-the-road-in-a-straight-truck/ [Accessed 04 02 2020].

134. Wood, R. M., 2006. A Discussion of a heavy truck advanced aerodynamic trailer system. *The Aerodynamics of Heavy Vehicles 2: Trucks, Buses and Trains.,* p. 14.

135. Wood, R. M. & Bauer, S., 2003. Simple and Low-Cost Aerodynamic Drag Reduction Devices for Tractor-Trailer Trucks. *SOLUS,* 1(724).

136. Wu, J. D. & Liu, J. C., 2011. Development of a predictive system for a car fuel consumtion using an artifical neural network. *Expert system with applications,* 38(5), pp. 4967-4971.

137. Yang, Y. et al., 2017. *Analysis on the Influence of Gap Flow Around a Tractor-Trailer.* Portoroz, slovenia, ASTFE.

138. Yang, Z., 2020. *Fundamental Computational Fluid Dynamics - Lecture notes.* Derby: University of Derby.

139. Zdravkovich, M., 1977. Review of flow interfernce between two circular cylinders in various arrangement. *ASME,* pp. 618-633.

140. Zhang, H. & Melbourne, W. H., 1992. Interference between two circular cylinders in tandem in turbulent flow. *Journal of wind end and ind aerodynamics,* Volume 41, pp. 589-600.

141. Zhiying, Z. et al., 2010. Study on the effect of the distance between the front and the comapartment of van its aerodynamic caractertistics. *Energy Conservation Technology,* 28(16).

142. Castellucci, P. J. & Salari, K. (2010) 'Computational Simulation of Tractor-Trailer Gap Flow with Drag-Reducing Aerodynamic Devices', *SAE Technical Paper Series*, 1(724). doi: 10.4271/2005-01-3625.

143. CCM+, S. (2019) 'Realizable k-ep model'.

144. Jones, W. P & Launder, B. E. (1972) 'K-E Model of Turbulence.Pdf', *International Journal of Heat and Mass Transfer*, 15(December), pp. 301–314. doi: 10.1016/0017-9310(72)90076-2.

145. Allen, J.J & Smits, A. J. (2001) 'Energy Harvesting Eel', *Journal of Fluids and Structures*, 15(1), pp. 1–13. doi: 10.1006/j.

146. Star CCM+ (2019) 'SST K-Omega solver', p. 1.